

UNIVERSITÀ
DI PAVIA

Dipartimento di Biologia e Biotecnologie "L. Spallanzani"

Laurea Magistralis in Neurobiologia

Resolving directionality in structural cerebellar connectivity with literature-derived anatomical evidence and diffusion tractography

La direzionalità della connettività cerebellare svelata mediante evidenze anatomiche su traccianti derivate dalla letteratura e trattografia

Supervisor:
Prof. Fulvia Palesi

Co-supervisors:
Dr. Marta Garivaghi
Dr. Eleonora Lupi

Experimental thesis
by
Alexa Escobar Pastor

Academic Year 2025/2026

INDEX

Abstract ii
Abstract (Italian Version) iv
Abbreviations vi
1.Introduction 1
1.1 Anatomy of the Cerebellum 1
1.2 Diffusion MRI and Tractography 6
1.2.1 MRI and Diffusion MRI 6
1.2.2 Structural Connectivity and Fiber Modeling 7
1.2.3 Tractography 8
1.2.4 Anatomically Constrained Tractography 9
1.2.5 Interpretation and Limitations of Tractography 10
1.3 Graph Theory 10
1.4 Methodological Overview of Structural Connectivity Evidence 11
1.5 Aim and Objectives 12
2. Material and Methods 13
2.1 Study Design 13
2.1.1 Regions of Interest (ROI) 14
2.2 Cerebellar Structural Connectivity Pathways 19
2.2.1 Compilation of the Anatomical Reference 19
2.2.2 Intracerebellar Structural Connections 19
2.2.3 Structural Connectivity Between the Cerebellum and Brainstem Nuclei 21
2.2.4 Cerebellar Thalamic and Subcortical Structural Connections 30
2.3 Analysis on Connections 32
2.3.1 Graph-Theoretical Analysis 32
2.3.2 MRI Dataset and Participant 35
2.3.3 Anatomical Parcellation and Regions of Interest 35
2.3.5 Comparison with Literature-Based Connectivity 40
2.4 Software 42
3. Results 44
3.1 Literature-Derived Binary Structural Connectivity Matrix 44
3.2 Graph Theory 50
3.3 Tractography Reconstruction 54
4. Discussion 65
5. **Bibliography** 71

Abstract

The cerebellum is directly connected with the brainstem and subcortical structures (e.g., thalamus) through pathways with a defined direction and laterality. Its communication with the cerebral cortex is indirect: cortical information reaches the cerebellum through the pontine nuclei, while the cerebellar output returns to the cortex through the thalamus. Diffusion MRI tractography is increasingly used to reconstruct these pathways in human brain *in vivo*, but its anatomical accuracy in the cerebellum is difficult to assess, and it cannot determine the directionality of reconstructed connections. Tract-tracing methods, which identifies directly where axons originate and terminate, are generally not feasible in the human brain *in vivo*, but have been widely used in animal models, including rodents, cats and non-human primates. Although reviews of cerebellar connectivity based on tract-tracing evidence are available, this evidence has not been systematically organized into a directed and lateralized connectivity matrix that can be compared with tractography results.

The main aim of this thesis was to construct a binary connectivity matrix based on an extensive review of anatomical studies in animal models, encoding directionality and laterality (ipsilateral, contralateral, or bilateral) of cerebellar connections. Tract-tracing studies were the primary source of evidence and were integrated with findings from lesion-degeneration and electrophysiological studies. The connectivity matrix derived from anatomical studies included intracerebellar connections, and connections between the cerebellum and brainstem, and between cerebellum and subcortical regions such as the thalamus and hypothalamus. It was then integrated with the brainstem-brainstem, brainstem-subcortical, and cortical-brainstem connections. The resulting matrix comprised 139 regions and 1876 directed connections, of which 699 involved the cerebellum. The second aim was to characterize how the cerebellar regions were connected using graph theory analysis. The third aim was to use the matrix as an anatomical reference for evaluating seven diffusion MRI tractography configurations in one healthy participant from the Human Connectome Project in Aging. These configurations differed in their anatomical constraints, seeding strategies, tracking algorithms, fiber orientation distribution (FOD) thresholds, and image resolutions. The agreement with the reference matrix was quantified with the Youden's J index, which combines sensitivity and specificity, being higher for better agreement. Tractography performance was also assessed separately for ipsilateral and contralateral connections.

Graph-theoretical analysis reflected the known organization of the cerebellum. The cerebellar cortex mainly received connections, while the deep cerebellar nuclei acted as central relay

regions that received and sent many connections. The best agreement with the literature-derived matrix was achieved by three tractography configurations that used a modified anatomical segmentation, in which the deep cerebellar and brainstem nuclei, hypothalamus, septal nuclei, subthalamic nucleus and claustrum were classified as gray matter rather than white matter. Two of these seeded streamlines at the gray matter-white matter interface, with the default and a slightly higher FOD cutoff, and the third used dynamic seeding.

For cerebellar connections, the best configuration (Youden's J = 0.29) used the modified anatomical segmentation with a slightly stricter fiber orientation distribution cutoff (0.06 instead of the default 0.05). The modified segmentation with the default cutoff recovered the largest number of anatomical connections but also produced more false positive connections. For the whole matrix, the best configuration used the same modified anatomical segmentation with dynamic seeding during tracking (Youden's J = 0.32). For both cerebellar and whole brain connections, the standard anatomical segmentation configuration performed worst (Youden's J = 0.09), mainly due to a higher number of false positive connections. Even so, all configurations reconstructed more false-positive than true connections. Ipsilateral cerebellar connections were recovered more than twice as often as contralateral connections, while the crossed projection from the deep cerebellar nuclei to the thalamus was not reconstructed by the best-performing configurations.

To conclude, encoding directionality in the matrix showed that the cerebellar cortex mainly receives connections, while the deep cerebellar nuclei are the main output of the cerebellum. Encoding laterality revealed systematic errors of tractography in crossed pathways that a reference without laterality would not detect. Modifying the anatomical segmentation was the methodological choice that most improved the agreement between tractography and the literature-derived matrix. Overall, the literature-derived matrix provides an anatomically grounded reference for evaluating diffusion MRI tractography of cerebellar connections, allowing the assessment of both connection directionality and laterality.

Abstract (Italian Version)

Il cervelletto è direttamente connesso con il tronco encefalico e con strutture sottocorticali, come il talamo, attraverso connessioni di materia bianca caratterizzate da direzionalità e lateralità. La comunicazione con la corteccia cerebrale è invece indiretta: le informazioni corticali raggiungono il cervelletto attraverso i nuclei pontini, mentre le efferenze cerebellari raggiungono la corteccia attraverso il talamo. La trattografia basata sulla risonanza magnetica di diffusione è sempre più utilizzata per ricostruire queste connessioni nel cervello umano *in vivo*, ma la sua accuratezza anatomica nel cervelletto è difficile da valutare e non consente di determinarne la direzionalità. I metodi di tracciamento assonale, che identificano l'origine e la terminazione degli assoni, non sono generalmente applicabili al cervello umano *in vivo*, ma sono stati ampiamente utilizzati in modelli animali, tra cui roditori, gatti e primati non umani. Sebbene siano disponibili revisioni della connettività cerebellare basate su queste evidenze, manca una matrice sistematica che ne codifichi direzionalità e lateralità e che possa essere confrontata con i risultati della trattografia.

L'obiettivo principale di questa tesi è stato costruire, attraverso un'ampia revisione della letteratura anatomica su modelli animali, una matrice binaria di connettività che codificasse la direzionalità e la lateralità delle connessioni cerebellari (ipsilaterali, controlaterali o bilaterali). Gli studi di tracciamento assonale hanno costituito la principale fonte di evidenze, integrate con studi di degenerazione conseguente a lesioni ed elettrofisiologici. La matrice comprendeva le connessioni intracerebellari, quelle tra cervelletto e tronco encefalico e quelle tra cervelletto e regioni sottocorticali, come talamo e ipotalamo. È stata poi integrata con le connessioni interne al tronco encefalico, quelle tra tronco encefalico e strutture sottocorticali e quelle tra corteccia e tronco encefalico. La matrice risultante comprendeva 139 regioni e 1876 connessioni direzionate, di cui 699 coinvolgevano il cervelletto. Il secondo obiettivo era caratterizzare la connettività cerebellare mediante la teoria dei grafi; il terzo era utilizzare la matrice come riferimento anatomico per valutare sette configurazioni di trattografia in un partecipante sano dello Human Connectome Project in Aging. Le configurazioni differivano per vincoli anatomici, strategie di inizializzazione delle streamline (seeding), algoritmi di tracciamento, soglie FOD e risoluzioni delle immagini. La concordanza con la matrice è stata quantificata mediante l'indice J di Youden, che combina sensibilità e specificità. Le prestazioni sono state valutate anche separatamente per le connessioni ipsilaterali e controlaterali.

L'analisi basata sulla teoria dei grafi ha evidenziato un'organizzazione coerente con quella nota del cervelletto: la corteccia cerebellare presentava prevalentemente connessioni afferenti,

mentre i nuclei cerebellari profondi svolgevano un ruolo centrale, con numerose connessioni afferenti ed efferenti. La maggiore concordanza con la matrice è stata ottenuta da tre configurazioni che utilizzavano una segmentazione anatomica modificata, nella quale i nuclei cerebellari profondi e del tronco encefalico, l'ipotalamo, i nuclei settali, il nucleo subtalamico e il claustro erano classificati come sostanza grigia anziché bianca. Due configurazioni inizializzavano le streamline all'interfaccia tra materia grigia e bianca, con la soglia FOD predefinita o una soglia leggermente più elevata; la terza utilizzava il seeding dinamico.

Per le connessioni cerebellari, la configurazione migliore (J di Youden = 0.29) combinava la segmentazione modificata con una soglia FOD di 0.06 anziché 0.05. La stessa segmentazione con soglia predefinita ricostruiva il maggior numero di connessioni anatomiche, ma produceva anche più falsi positivi. Per l'intera matrice, la configurazione migliore utilizzava la segmentazione modificata con seeding dinamico (J di Youden = 0.32). Sia per le connessioni cerebellari sia per l'intero cervello, la segmentazione standard mostrava le prestazioni peggiori (J di Youden = 0.09), principalmente a causa dei falsi positivi. Tutte le configurazioni ricostruivano comunque più connessioni false positive che vere. Le connessioni cerebellari ipsilaterali venivano ricostruite con una frequenza più che doppia rispetto a quelle controlaterali, mentre le connessioni controlaterali tra nuclei cerebellari profondi e talamo non veniva ricostruita dalle configurazioni migliori.

In conclusione, la codifica della direzionalità nella matrice ha mostrato che la corteccia cerebellare presenta prevalentemente connessioni afferenti, mentre i nuclei cerebellari profondi costituiscono la principale sede di origine delle efferenze cerebellari. La codifica della lateralità ha evidenziato errori sistematici della trattografia nella ricostruzione delle proiezioni controlaterali, che non sarebbero stati rilevati utilizzando un riferimento privo di informazioni sulla lateralità. La modifica della segmentazione anatomica è stata la scelta metodologica che ha migliorato maggiormente la concordanza tra la trattografia e la matrice binaria derivata dalla letteratura. Nel complesso, questa matrice fornisce un riferimento fondato su evidenze anatomiche per valutare le ricostruzioni delle connessioni cerebellari ottenute da trattografia, tenendo conto sia della direzionalità sia della lateralità delle connessioni.

Abbreviations

Abbreviation	Term	Abbreviation	Term
5TT	Five-tissue-type image	mRT	Mesencephalic reticular formation
ABD	Abducens nucleus	MSGn	Limitans–suprageniculate and medial geniculate nuclei
Accu	Nucleus accumbens	MSMT-CSD	Multi-shell multi-tissue constrained spherical deconvolution
ACT	Anatomically Constrained Tractography	NDA	NIMH Data Archive
Amyg	Amygdala	NIMH	National Institute of Mental Health
ANTs	Advanced Normalization Tools	NRTP	Nucleus reticularis tegmenti pontis
AV	Anteroventral thalamic nucleus	PAG	Periaqueductal gray
BET	Brain Extraction Tool	Pall	Pallidum
BPN	Basilar pontine nuclei	Pb	Parabrachial nucleus
Caud	Caudate nucleus	Pc	Paracentral thalamic nucleus
Cbm	Cerebellum (prefix of cerebellar cortical regions)	Pf	Parafascicular thalamic nucleus
CeM	Central medial thalamic nucleus	PFC	Prefrontal cortex
CL	Central lateral thalamic nucleus	PHA-L	Phaseolus vulgaris leucoagglutinin
Cla	Claustrum	PMSMA	Premotor cortex and supplementary motor area
CM	Centromedian thalamic nucleus	PnC	Caudal pontine reticular nucleus
CN	Cochlear nuclei	PnO	Oral pontine reticular nucleus
CNN	Convolutional neural network	PPN	Pedunculopontine nucleus
COMMIT	Convex Optimization Modeling for Microstructure Informed Tractography	PPRF	Paramedian pontine reticular formation
CSD	Constrained spherical deconvolution	PulA	Pulvinar, anterior nucleus
CSR	Central superior raphe nucleus	PulI	Pulvinar, inferior nucleus
DCN	Deep cerebellar nuclei	PulL	Pulvinar, lateral nucleus

dMRI	Diffusion-weighted magnetic resonance imaging	PulM	Pulvinar, medial nucleus
DN	Dentate nucleus	Puta	Putamen
DTI	Diffusion tensor imaging	Re	Nucleus reuniens
F0	Trophic incoherence parameter	RN	Red nucleus
FA	Fractional anisotropy	RNPON	Raphe nucleus pontis
FAST	FMRIB's Automated Segmentation Tool	ROI	Region of interest
FIRST	FMRIB's Integrated Registration and Segmentation Tool	SC	Superior colliculus
FM	Facial motor nucleus	SD_STREAM	Streamline tractography based on spherical deconvolution (deterministic)
FN	Fastigial nucleus	Septal	Septal nuclei
FNe	False negative	SIFT2	Spherical-deconvolution Informed Filtering of Tractograms 2
FOD	Fiber orientation distribution	SNc	Substantia nigra pars compacta
FP	False positive	SNr	Substantia nigra pars reticulata
FSL	FMRIB Software Library	SOC	Superior olivary complex
GM-WM	Gray matter–white matter (interface)	SSN	Superior salivatory nucleus
HCP-A	Human Connectome Project in Aging	Subthal	Subthalamic nucleus
Hippo	Hippocampus	SUIT	Spatially Unbiased Infratentorial Template
HRP	Horseradish peroxidase	SyN	Symmetric normalization
Hypo	Hypothalamus	T1	Longitudinal relaxation time
IC	Inferior colliculus	T2	Transverse relaxation time
iFOD2	Second-order integration over fiber orientation distributions	TE	Echo time
IN	Interposed nuclei	Thal	Thalamus (prefix of thalamic regions)

IntC	Intralaminar thalamic nuclei, caudal (CM, Pf)	TM	Trigeminal motor nucleus
IntR	Intralaminar thalamic nuclei, rostral (CeM, CL, Pc)	TN	True negative
ION	Inferior olivary nucleus	TP	True positive
LC	Locus coeruleus	TPS	Principal sensory trigeminal nucleus
LD	Laterodorsal thalamic nucleus	TR	Repetition time
LDP	Laterodorsal and lateral posterior thalamic nuclei	VA	Ventral anterior thalamic nucleus
LDT	Laterodorsal tegmental nucleus	Ve	Vestibular nuclei
LGn	Lateral geniculate nucleus	VL	Ventral lateral thalamic nucleus
M1	Primary motor cortex	VLa	Ventral lateral thalamic nucleus, anterior part
MD	Mediodorsal thalamic nucleus	VLp	Ventral lateral thalamic nucleus, posterior part
MDl	Mediodorsal thalamic nucleus, lateral (parvocellular) part	VM	Ventral medial thalamic nucleus
MDm	Mediodorsal thalamic nucleus, medial (magnocellular) part	VPL	Ventral posterolateral thalamic nucleus
MNI	Montreal Neurological Institute	VTA	Ventral tegmental area
MPRAGE	Magnetization-prepared rapid gradient echo	WGA-HRP	Wheat germ agglutinin–horseradish peroxidase
MR	Magnetic resonance	ZI	Zona incerta
MRI	Magnetic resonance imaging		

In tables and figures, L and R after an abbreviation indicate the left and right hemisphere. Thalamic and cerebellar cortical regions of the parcellation are labeled with the prefixes Thal_ and Cbm_ (Table 1).

1.Introduction

1.1 Anatomy of the Cerebellum

The cerebellum is the largest component of the hindbrain, and it is located within the posterior cranial fossa. It is inferior to the occipital lobes of the cerebral hemispheres separated by the tentorium cerebelli, and it lies posteriorly to the pons and medulla. Its anterior surface contributes to the roof of the fourth ventricle. Although the cerebellum makes up only a small fraction of total brain volume (10%), it contains more than half of the brain's neurons and an extensively folded cortex, allowing a large cortical surface area to fit within the confined space of the posterior cranial fossa (Lara-Aparicio et al., 2022; Voogd & Glickstein, 1998).

The cerebellum consists of two lateral hemispheres connected across the midline by the vermis (Figure 1). The cerebellar surface is organized into numerous folds called folia, which are separated by shallow sulci and deeper fissures. The folia are much smaller and more tightly packed than the gyri of the cerebral cortex. Major fissures divide the cerebellum into distinct lobes, while additional fissures delineate its lobules (Figures 1 and 2). The boundaries between the vermis and cerebellar hemispheres are relatively indistinct on the superior surface. On the inferior surface, a deep median groove called the vallecula separates the two hemispheres, with the inferior vermis lying within it (Lehman et al., 2020; Voogd & Marani, 2016).

The primary and posterolateral fissures divide the cerebellum into three anatomical lobes: the anterior, posterior, and flocculonodular lobes. These lobes are conventionally described using the Larsell numerical system, which divides the cerebellar vermis into ten lobules, designated I to X, with corresponding hemispheric regions traditionally identified by the prefix "H" (Larsell, 1952; Larsell & Jansen, 1972). The primary fissure separates the anterior lobe from the posterior lobe and is a prominent landmark on midsagittal images. And the posterolateral fissure separates the posterior from the flocculonodular lobe. The anterior lobe lies predominantly on the superior surface and comprises lobules I to V. The posterior lobe is the largest division, extending from lobule VI to lobule IX. The flocculonodular lobe corresponds to lobule X and consists of the midline nodulus and the paired lateral flocculi. The horizontal fissure is a further prominent landmark, separating the superior and inferior semilunar lobules of the cerebellar hemispheres. More specifically, it lies between Crus I superiorly and Crus II inferiorly, though it does not define the boundaries of the anterior, posterior, or flocculonodular lobes (Lehman et al., 2020; Voogd & Marani, 2016). Further subdivisions are used to describe the posterior cerebellum in anatomical and neuroimaging studies. In the hemisphere, lobule

VII is commonly divided into Crus I, Crus II, and lobule VIIB, while lobule VIII is divided into lobules VIIIA and VIIIB. These subdivisions can be identified on high-resolution MRI, although the morphology and boundaries of individual lobules vary considerably among individuals (Diedrichsen et al., 2009; Makris et al., 2003; Schmahmann et al., 1999).

Internally, the cerebellum comprises a highly folded cortex surrounding a central core of white matter. In sagittal sections, the branching appearance of the cerebellar white matter is known as the *arbor vitae*. Embedded within this white matter are the fastigial (FN), globose, emboliform, and dentate nuclei (DN). The globose and emboliform nuclei are commonly grouped as the interposed nuclei (IN), producing an approximate mediolateral arrangement of the FN, IN, and DN. These deep cerebellar nuclei (DCN) receive inhibitory projections from Purkinje cells and excitatory collaterals from cerebellar afferent fibers. They provide the principal source of cerebellar output to the brainstem and thalamus, although Purkinje cells in parts of the vestibulocerebellum project directly to the vestibular nuclei (Ve) (Middleton & Strick, 2001; Voogd & Glickstein, 1998; Voogd & Marani, 2016).

The cerebellar cortex is conventionally divided into three layers: the granular layer, Purkinje-cell layer, and molecular layer. Mossy fibers provide excitatory input to granule cells in the granular layer. Granule-cell axons ascend into the molecular layer and bifurcate to form parallel fibers, which synapse with the dendrites of Purkinje cells. Purkinje cells also receive powerful excitatory input from climbing fibers originating in the contralateral inferior olivary complex. Golgi cells and molecular-layer interneurons regulate cerebellar cortical activity through inhibitory signaling. Purkinje cells provide the sole output of the cerebellar cortex, and their GABAergic axons project primarily to the DCN or, in parts of the vestibulocerebellum, directly to the Ve (Hull & Regehr, 2022; Lara-Aparicio et al., 2022). Although this cellular arrangement is repeated throughout the cerebellar cortex, regional differences in neuronal identity, synaptic connectivity, and plasticity indicate that cerebellar regions are more specialized than suggested by the traditional view of identical repeated modules (Hull & Regehr, 2022).

The cerebellum communicates with the brainstem, spinal cord, vestibular system, and cerebral cortex through three paired white-matter bundles called the cerebellar peduncles. The inferior cerebellar peduncle carries afferent and efferent fibers connecting the cerebellum with the spinal cord, medulla, inferior olivary complex, and vestibular system. The middle cerebellar peduncle is composed predominantly of afferent pontocerebellar fibers, which convey information indirectly from the contralateral cerebral cortex through the pontine nuclei. The superior cerebellar peduncle carries most cerebellar output from the DCN toward the red

nucleus and thalamus, although it also contains afferent fibers. These peduncles constitute the principal macroscopic pathways through which the cerebellum participates in distributed cortical and subcortical networks and therefore provide an important anatomical basis for examining cerebellar structural connectivity using diffusion MRI (Lara-Aparicio et al., 2022; Palesi et al., 2017).

Cerebellar cortical regions and DCN do not operate as isolated anatomical compartments. Evidence from nonhuman-primate tract-tracing studies supports an organization consisting of parallel, partially segregated circuits connecting specific cerebellar regions with motor and association areas of the cerebral cortex through pontine and thalamic relays (Kelly & Strick, 2003; Strick et al., 2009). For example, separate closed-loop circuits have been identified between lobules IV–VI and the primary motor cortex and between Crus II and the prefrontal cortex (Kelly & Strick, 2003; Strick et al., 2009). This circuit organization provides an anatomical basis for the cerebellum's involvement in both motor and non-motor functions.

Although cerebellar size, relative expansion, and folding complexity differ substantially among species, fundamental features of cerebellar organization are conserved across mammals. Rodents, nonhuman primates, and humans share a layered and foliated cerebellar cortex, a central white-matter core, DCN, and an arrangement in which longitudinal cortical zones project to particular nuclear regions (Apps & Garwicz, 2005; Voogd & Glickstein, 1998). This conservation supports the use of animal models to investigate cerebellar microcircuits and pathway organization. However, conserved anatomical principles do not imply that the relative size, strength, or distribution of individual connections is identical across species. The human cerebellar cortex is considerably expanded and more densely folded relative to the neocortex than that of nonhuman primates, suggesting evolutionary elaboration of cerebellar circuitry associated with human motor and non-motor functions (Sereno et al., 2020).

Comparative tracing studies directly support the conservation of cerebellar circuits across species. Luo and colleagues combined axonal tracing and molecular expression analysis across humans, macaques, marmosets, rats, and mice to identify homologous cerebellar regions, and found that the region corresponding to human Crus I/II (the “ansiform area”, which corresponds to Crus I in rodents) exhibits conserved connectivity and molecular expression patterns across primates and rodents, despite being disproportionately expanded in the human cerebellum (about 34% of cerebellar volume in humans compared with about 10% in rodents) (Luo et al., 2017). These findings indicate that fundamental circuit organization can be

conserved across species even where relative volume and regional expansion differ substantially.

Despite this evolutionary conservation of major cerebellar circuits, it remains unclear whether the presence, laterality, and directionality of human cerebellar pathways correspond fully to patterns identified through invasive tracing in animal models. This uncertainty is partly methodological because conventional diffusion MRI tractography estimates the orientation and spatial course of white-matter pathways but cannot, by itself, determine the direction of axonal signaling or reliably distinguish afferent from efferent projections. The present thesis therefore builds a directed and lateralized structural connectivity matrix of the human cerebellum from the anatomical tract-tracing literature and uses it as a reference to evaluate how accurately diffusion MRI tractography reconstructs cerebellar pathways. This reference may provide a foundation for future research investigating whether the direction and laterality of human cerebellar connections correspond to or differ from the organizational patterns observed in animal models.

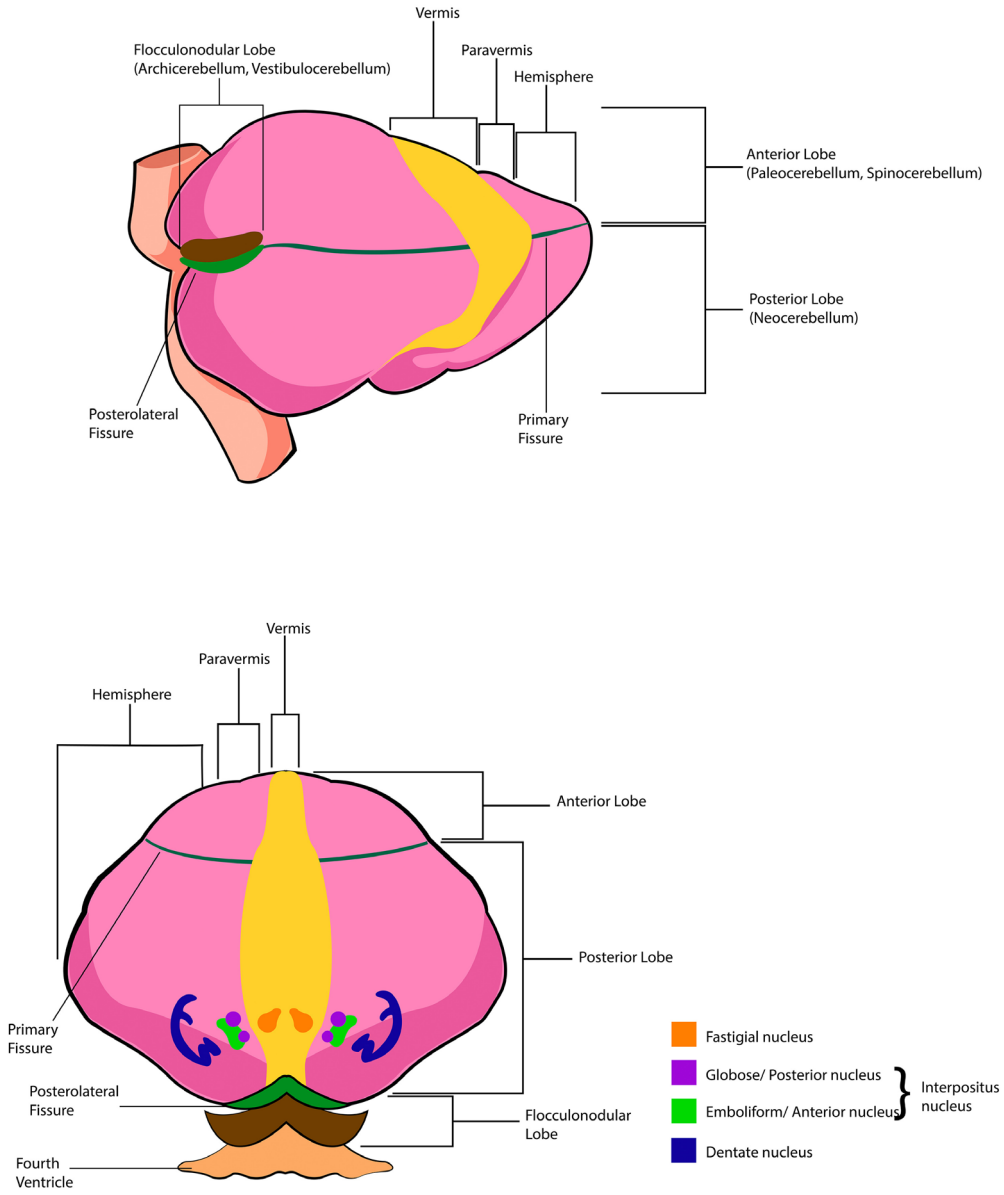


Figure 1. Sagittal and dorsal views of the adult human cerebellum showing its anatomical divisions according to the midline organization, major fissures, and phylogenetic classification. The figure identifies the vermis, paravermis, cerebellar hemispheres, anterior, posterior, and flocculonodular lobes, and the deep cerebellar nuclei. *Note.* Reprinted from "Latest Research on the Anatomy and Physiology of the Cerebellum," by S. Y. Lara-Aparicio et al., 2022, *Neurology Perspectives, 2*(1), p. 37 (https://doi.org/10.1016/j.neurop.2021.12.002). Copyright 2021 Sociedad Española de Neurología. Licensed under CC BY-NC-ND 4.0.

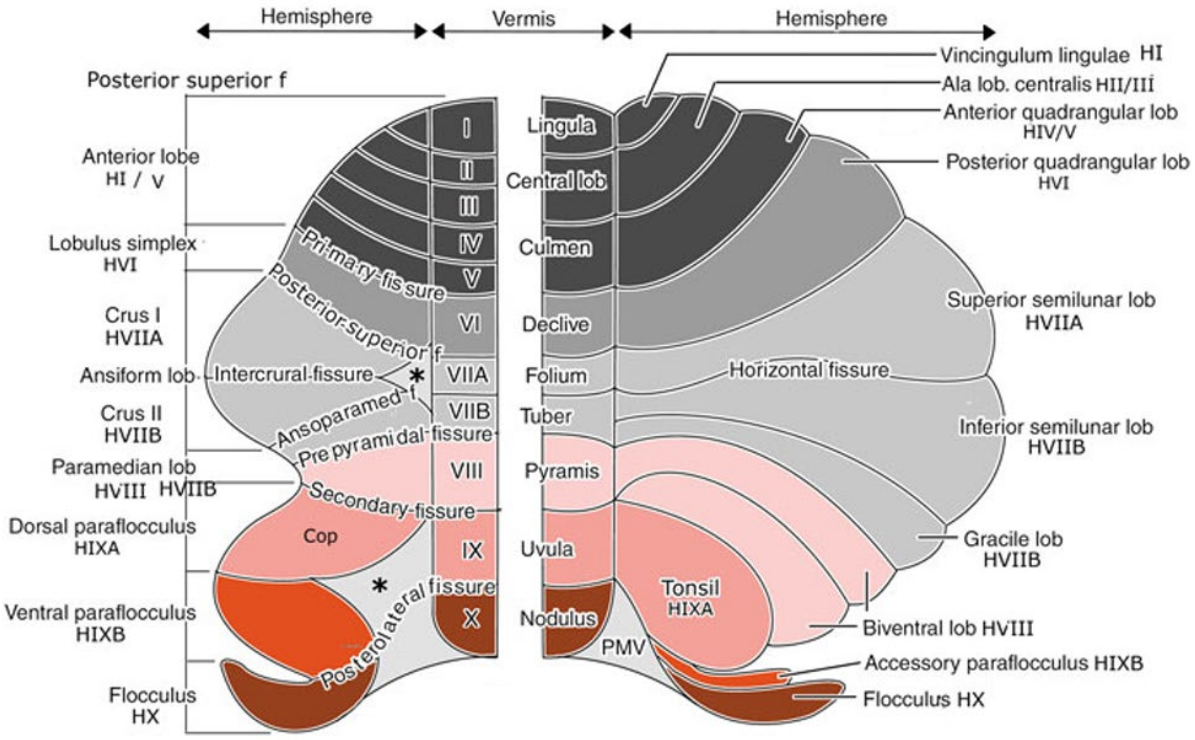


Figure 2. Anatomical subdivisions and nomenclature of the human cerebellum. The diagram illustrates the vermal lobules and their corresponding hemispheric regions according to classical anatomical terminology and Larsell's numerical classification. Reproduced from Voogd and Marani (2016), Figure 4.1.

1.2 Diffusion MRI and Tractography

1.2.1 MRI and Diffusion MRI

Magnetic resonance imaging (MRI) is a non-invasive technique that provides high-resolution images of brain anatomy. The MR signal arises mainly from hydrogen nuclei in water. When placed in a strong static magnetic field (B_0), these nuclei produce a net magnetization. A radiofrequency pulse disturbs this magnetization, and the signal emitted as it returns to equilibrium is spatially encoded with magnetic field gradients to form an image. Differences in relaxation properties between tissues produce the contrast of T1- and T2-weighted images (Grover et al., 2015).

The hydrogen nuclei rotate around B_0 at the Larmor frequency, which is proportional to the field strength ($\omega_0 = \gamma B_0$, where γ is the gyromagnetic ratio). After excitation by a radiofrequency pulse, the magnetization recovers along B_0 with the longitudinal relaxation time (T1) and loses its transverse component with the transverse relaxation time (T2). Because T1 and T2 differ

between tissues, the repetition time (TR) and echo time (TE) can be chosen to weight the image toward T1 or T2 contrast. A short TR and short TE produce T1-weighted images, in which white matter appears brighter than gray matter. A long TR and long TE produce T2-weighted images, in which cerebrospinal fluid appears bright. T1-weighted images are therefore commonly used for anatomical segmentation (Grover et al., 2015).

Diffusion-weighted MRI (dMRI) makes the MR signal sensitive to the random movement of water molecules. In white matter, cell membranes, axons and myelin restrict this movement, so water diffuses more easily along the axons than across them. By applying diffusion-encoding gradients along many directions, dMRI measures how diffusion varies with orientation. The strength of diffusion weighting is described by the b-value, and images without diffusion weighting ($b = 0$) serve as a reference. dMRI does not image axons directly, but the organization of the underlying fibers is inferred from water diffusion measured at a much larger scale than single axons (Jeurissen et al., 2019; Jones et al., 2013).

1.2.2 Structural Connectivity and Fiber Modeling

Structural connectivity refers to the anatomical connections between brain regions, formed by bundles of axons that travel through the white matter (Yeh et al., 2021). In the living human brain, these connections cannot be traced directly, but they can be estimated non-invasively by combining dMRI with tractography. The brain can then be represented as a network, in which brain regions are the nodes, and the estimated connections between them are the edges (Bullmore & Sporns, 2009; Hagmann et al., 2007).

The first widely used model, diffusion tensor imaging (DTI), describes diffusion in each voxel with a tensor whose main direction approximates the dominant fiber orientation (Basser et al., 1994). Fractional anisotropy (FA), derived from the tensor, describes how strongly diffusion depends on direction. However, the tensor can represent only one fiber orientation per voxel, while crossing, bending or fanning fibers are present in up to 90% of white-matter voxels (Jeurissen et al., 2013). Constrained spherical deconvolution (CSD) addresses this limitation by estimating a fiber orientation distribution (FOD) in each voxel, which can represent several fiber populations at once (Dell'Acqua & Tournier, 2019; Tournier et al., 2007). Multi-shell, multi-tissue CSD (MSMT-CSD) extends this approach to data acquired with several b-values. Because white matter, gray matter and cerebrospinal fluid respond differently to diffusion weighting, the additional shells allow the signal to be separated into tissue-specific components, which yields a cleaner white-matter FOD in voxels that contain more than one tissue type (Jeurissen et al., 2014).

1.2.3 Tractography

Tractography uses these local orientation estimates to reconstruct white-matter pathways. Starting from seed points, an algorithm advances step by step along the local fiber orientation, producing virtual trajectories called streamlines. The full set of streamlines is called a tractogram (Jeurissen et al., 2019). Streamlines are computational reconstructions compatible with the diffusion signal, not individual axons. In deterministic tractography, the direction at each step is fixed by the local orientation, so the same seed always produces the same streamline (Basser et al., 2000; Mori et al., 1999). In probabilistic tractography, the direction is sampled from the local orientation estimate, so many plausible trajectories can be explored from the same seed (Behrens et al., 2003). This can increase sensitivity in regions with complex fiber configurations, but it can also generate more anatomically implausible streamlines. The iFOD2 algorithm in MRtrix3 is a probabilistic method that samples short curved paths and favors those well supported by the FOD amplitudes along their length (Tournier et al., 2019).

Seeding defines where streamlines start. A seed point is not the biological origin of an axon, but it only starts the tracking process. Seeds can be placed throughout white matter or at the interface between gray and white matter, so that streamlines begin where axons are expected to enter or leave gray matter (Smith et al., 2012). In dynamic seeding, new seeds are placed preferentially where the reconstructed streamline density is lower than expected from the FODs (Smith et al., 2015). The seeding strategy affects which connections are reconstructed and how often.

When tracking relies only on diffusion information, streamlines can stop in the middle of white matter or enter cerebrospinal fluid, which is inconsistent with anatomy. Anatomically Constrained Tractography (ACT) uses a tissue segmentation derived from a T1-weighted image to accept or reject streamlines according to where they terminate (Smith et al., 2012). ACT removes some classes of implausible streamlines, but it does not prove that the remaining streamlines correspond to real connections. The tissue segmentation used by ACT is described in Section 1.2.4.

Once a tractogram has been generated, streamlines can be assigned to predefined regions to build the structural connectivity matrix. Because each step of this pipeline (diffusion model, tracking algorithm, anatomical constraints and seeding) can change the resulting connections, these choices must be considered when interpreting tractography-based connectivity (Yeh et al., 2021). The cerebellum is particularly challenging in this respect, because its main input and output pathways pass through the brainstem, where fiber bundles cross and lie close together.

1.2.4 Anatomically Constrained Tractography

Anatomical information can be incorporated into tractography through a five-tissue-type (5TT) segmented image. In MRtrix3, the 5TT image is specifically designed for use with Anatomically Constrained Tractography (ACT) and represents five tissue compartments:

- Cortical gray matter
- Subcortical gray matter
- White matter
- Cerebrospinal fluid
- Pathological or unclassified tissue

Each compartment is represented by partial volume fractions rather than exclusively by binary labels, allowing tissue boundaries to be represented more accurately (R. E. Smith et al., 2012).

The 5TT image can be generated from a structural T1-weighted image using the *5ttgen* command. Different segmentation algorithms are available, including approaches based on FSL and FreeSurfer. In FSL, *5ttgen* uses BET (Brain Extraction Tool) for brain extraction, FAST (FMRIB's Automated Segmentation Tool) for tissue segmentation, and FIRST (FMRIB's Integrated Registration and Segmentation Tool) for the segmentation of subcortical structures (Patenaude et al., 2011; R. E. Smith et al., 2012; S. M. Smith, 2002; Tournier et al., 2019; Zhang et al., 2001).

The 5TT image assigns different anatomical roles to the tissue compartments. White matter defines the main domain through which streamlines propagate, because axons should not terminate within normal white matter or enter fluid-filled regions (R.E. Smith et al., 2012). A streamline that enters cortical gray matter is considered to have reached an appropriate termination point, whereas a streamline that enters cerebrospinal fluid is rejected. A streamline that leaves the field of view is accepted, which allows tracking towards the spinal cord. A streamline that stops within white matter, for example because of a low FOD amplitude or high curvature, is rejected, but if it stops within subcortical gray matter it is accepted. Once a streamline has entered a subcortical structure, it is not allowed to exit it, yet if it tries to, it is truncated within that structure. The fifth compartment of the MRtrix3 5TT image allows pathological tissue to be represented separately when required, preventing lesions or other abnormal tissue from being forced into one of the four other categories (R. E. Smith et al., 2012).

1.2.5 Interpretation and Limitations of Tractography

Despite its widespread use, tractography output must be interpreted with caution, as reconstructed connectomes are known to contain a substantial proportion of both false-positive and false-negative connections (Maier-Hein et al., 2017). As well, tractography cannot determine the direction of a connection, because the diffusion signal reflects the local movement of water molecules rather than the direction in which axons carry signals (Jbabdi & Johansen-Berg, 2011). Studies comparing tractography with tracer injections in non-human primates have also shown that even when tractography correctly detects a connection, its estimate of connection strength agrees only moderately with the true axonal density. Part of this agreement is explained by distance, because both tractography and tracer-based connection strengths decrease as the distance between regions increases; once distance is taken into account, the agreement becomes weaker (Donahue et al., 2016). At the network level, false-positive connections affect the estimated network organization at least twice as much as false negatives, because they can create artificial links between groups of regions that are not directly connected (Zalesky et al., 2016). Taken together, this indicates that tractography-derived connectomes should be treated as approximations of the underlying anatomy rather than as ground-truth structural maps.

1.3 Graph Theory

Once a structural connectivity matrix has been built, its organization can be described with graph theory (Bullmore & Sporns, 2009; Rubinov & Sporns, 2010). In graph theory, brain regions are represented as nodes and the connections between them as edges. In a binary directed network, each edge is either present or absent and goes from a source region to a target region. The density of the network is the proportion of all possible edges that are present. The in-degree of a node is the number of edges it receives, and its out-degree is the number of edges it sends. Betweenness centrality measures how often a node lies on the shortest paths between other pairs of nodes, and therefore how important it is for communication across the network (Freeman, 1977; Rubinov & Sporns, 2010). The clustering coefficient measures how often the neighbors of a node are also connected to each other (Fagiolo, 2007; Watts & Strogatz, 1998). Reciprocity is the proportion of edges whose reverse edge is also present, that is, the proportion of connections that run in both directions (Garlaschelli & Loffredo, 2004). Local reciprocity applies the same idea to a single node, as the proportion of its connections that run in both directions. Finally, trophic analysis assigns each node a trophic level according to its position in the flow of directed connections. Nodes that mainly send connections have low levels, and

nodes that mainly receive connections from lower-level nodes have higher levels. The trophic incoherence parameter (F0) summarizes how hierarchical the whole network is, from 0 (a perfectly hierarchical network, in which every edge points up by one level) to 1 (no hierarchical organization) (MacKay et al., 2020).

1.4 Methodological Overview of Structural Connectivity Evidence

This section outlines the main methodologies behind the collected studies to clarify the basis on which connections were included.

The main source of evidence was conventional tract tracing in animals, including non-human primates, cats, rabbits, rats, and mice. By injecting anterograde or retrograde tracers, such as horseradish peroxidase (HRP), radiolabeled amino acids detected by autoradiography, and Phaseolus vulgaris leucoagglutinin (PHA-L), into defined cerebellar cortical territories or deep nuclei, these studies map both the presence and the direction of projections (Apps & Garwicz, 2005; Boonstra, 2025; Voogd & Glickstein, 1998). This approach provides high-confidence anatomical evidence for corticonuclear, cerebellothalamic, and reciprocal cerebellum–brainstem connections (Apps & Garwicz, 2005; Ruigrok, 2011). Because some cerebellar output reaches the forebrain through multisynaptic routes that conventional tracers cannot follow, transsynaptic viral tracing has been used to identify multi-relay circuits (Kelly & Strick, 2003; Pisano et al., 2021; Rogers & Beier, 2021; Xu et al., 2020). These multisynaptic findings were used to interpret circuits but were not encoded in the matrix, which was restricted to monosynaptic projections. Lesion studies and histological microanatomy support a local organization of the cerebellar cortex into longitudinal zones and microzones (Apps & Garwicz, 2005; Ruigrok, 2011; Wu et al., 2023). Some of the animal studies used to build the matrix relied on electrophysiological recording and stimulation to define connections (Andersson & Oscarsson, 1978; Ekerot et al., 1991). Diffusion tractography, in contrast, does not trace axons directly and cannot resolve synapses or the direction of a connection. Its results should therefore be interpreted with caution and alongside anatomical evidence (Jones et al., 2013; Thomas et al., 2014). For this reason, human imaging studies, including tractography, were not used to code connections in the matrix.

1.5 Aim and Objectives

Diffusion MRI tractography is widely used to reconstruct human brain connectivity, but it has important limitations, as described in Section 1.2.5. Tractography limitations are especially relevant for the cerebellum, whose afferent and efferent pathways are strongly directional and frequently cross the midline, and whose lobules and nuclei lie only millimeters apart.

This thesis aimed to evaluate how accurately diffusion MRI tractography reconstructs human cerebellar connectivity, using a lateralized, directed binary structural connectivity matrix derived from anatomical literature as a reference. The specific objectives were:

1. to construct, from a review of anatomical tract-tracing studies, a binary directed connectivity matrix of the afferent, efferent and intracerebellar projections of the cerebellum, in which left and right regions were coded separately so that each projection could be encoded as ipsilateral, contralateral or bilateral;
2. to characterize the organization of this matrix using graph-theoretical measures and
3. to compare seven tractography configurations in a single participant with the undirected version of the matrix, to identify the configuration that best reproduces known cerebellar connectivity and to assess whether ipsilateral and contralateral connections are reconstructed correctly.

2. Material and Methods

2.1 Study Design

This study used a review of the anatomical literature to build a binary reference matrix of human cerebellar structural connectivity and compared diffusion MRI tractography against this reference to evaluate how accurately different tractography configurations reconstruct cerebellar connections. As well, graph theoretical measures were applied to the binary directed matrix to characterize the organization of cerebellar connectivity, including the role of the deep cerebellar nuclei and the hierarchical positions of cerebellar regions within the network. Structural connectivity in the present work was represented using a binary matrix to encode the direction and laterality of each connection. The matrix was also directed and coded separately for each hemisphere, because anatomical tract-tracing evidence is typically reported as directional and hemisphere-specific, for example, a projection arising predominantly from the contralateral versus ipsilateral nucleus, or a pathway that is present in one direction but absent in the other direction. A binary directed matrix can preserve these afferent/efferent and left/right distinctions directly as separate coded edges.

The study was carried out in four steps. First, connections of the cerebellum, both among cerebellar regions between the cerebellum and the brainstem, and cortical and subcortical structures were identified from the anatomical literature and encoded into a binary directed connectivity matrix, including the laterality of each projection. The literature was collected from tract-tracing studies in different animal models, including non-human primates, cats, and rodents.

Second, the organization of the matrix was characterized using graph-theoretical measures computed on the binary directed network of 139 regions. In-degree and out-degree described the number of afferent and efferent connections of each region. Betweenness centrality described how often a region lies on the shortest paths between other regions. The clustering coefficient described how interconnected the neighbors of a region are, and local reciprocity described the proportion of a region connections present in both directions. Trophic level and trophic incoherence were used to describe the hierarchical position of each region and the overall hierarchical organization of the network.

Third, diffusion MRI data from one healthy participant of the HCP-A dataset were used to reconstruct the connections among the same regions, with the pontine nuclei merged into a single pons region, using seven tractography configurations that differed in anatomical

constraints, seeding strategy, tracking algorithm, fiber orientation distribution amplitude cutoff, and image resolution.

Finally, the connections reconstructed by each configuration were compared with the reference matrix and classified as true positives, false positives, false negatives, or true negatives, and the configuration that best reproduced the matrix was identified. Because tractography cannot determine the direction of a projection, the comparison was performed on undirected connections. When reconstructed connections were interpreted, their direction was taken from the reference matrix.

2.1.1 Regions of Interest (ROI)

The connectivity matrixes were defined on a common set of brain regions covering the cerebellum, the brainstem, and the supratentorial structures connected with them. For tractography, the participant's brain was parcellated into 112 regions (Table 1). The thalamus was divided into 16 regions per hemisphere by combining neighboring nuclei (Table 2). For the graph-theoretical analysis, the pons was further divided into 14 nuclei per hemisphere (Table 3), giving 139 regions in total. The parcellation was built in the laboratory by combining several atlases and segmentation tools (Table 4).

Group	Region	Abbreviation	Left	Right
Cerebral cortex	Prefrontal cortex	PFC	1	4
	Primary motor cortex	M1	2	5
	Premotor and supplementary motor area	PMSMA	3	6
Hypothalamus	Hypothalamus	Hypo	7	33
Thalamus	Anteroventral	Thal_AV	8	34
	Laterodorsal + lateral posterior	Thal_LDP	9	35
	Ventral anterior	Thal_VA	10	36
	Ventral lateral anterior	Thal_VLA	11	37
	Ventral lateral posterior	Thal_VLP	12	38
	Ventral posterolateral + ventromedial	Thal_VPL	13	39
	Intralaminar, rostral (CeM, CL, Pc)	Thal_IntR	14	40

	Intralaminar, caudal (CM, Pf)	Thal_IntC	15	41
	Mediodorsal, medial	Thal_MDm	16	42
	Mediodorsal, lateral	Thal_MDl	17	43
	Lateral geniculate	Thal_LGn	18	44
	Limitans–supragenículate + medial geniculate	Thal_MSGn	19	45
	Pulvinar anterior / inferior / lateral / medial	Thal_PulA / PulI / PulL / PulM	20–23	46–49
Subcortical	Caudate	Caud	24	50
	Putamen	Puta	25	51
	Pallidum	Pall	26	52
	Nucleus accumbens	Accu	27	53
	Hippocampus	Hippo	28	54
	Amygdala	Amyg	29	55
	Septal nuclei	Septal	30	56
	Subthalamic nucleus	Subthal	31	57
	Claustrum	Cla	32	58
Midbrain	Red nucleus	RN	59	72
	Substantia nigra pars compacta	SNc	60	73
	Substantia nigra pars reticulata	SNr	61	74
	Superior colliculus	SC	62	75
	Inferior colliculus	IC	63	76
	Mesencephalic reticular formation	mRT	64	77
	Ventral tegmental area	VTA	69 (midline)	
	Periaqueductal gray	PAG	70 (midline)	
Pons	Pons (28 pontine nuclei merged)	Pons	71 (midline)	

	Locus coeruleus	LC	65	78
	Nucleus reticularis pontis oralis	PnO	68	81
Medulla	Inferior olivary nucleus	ION	66	79
	Vestibular nuclei	Ve	67	80
Cerebellar cortex	Lobules I–IV	Cbm_I_IV	82	103
	Lobule V	Cbm_V	83	104
	Lobule VI	Cbm_VI	84	105
	Crus I	Cbm_CrusI	85	106
	Crus II	Cbm_CrusII	86	107
	Lobule VIIb	Cbm_VIIb	87	108
	Lobule VIIIa	Cbm_VIIIa	88	109
	Lobule VIIIb	Cbm_VIIIb	89	110
	Lobule IX	Cbm_IX	90	111
	Lobule X	Cbm_X	91	112
	Vermis VI / VII / VIII / IX / X	Cbm_Vermis_VI–X	95–99 (midline)	
Deep cerebellar nuclei	Dentate	DN	92	100
	Interposed	IN	93	101
	Fastigial	FN	94	102

Table 1. Regions of the 112-node parcellation used for tractography. Numbers correspond to the node indices of the connectivity matrices and to the streamline of file names mentioned in the tractography section below. The 28 pontine nuclei of the 139-region matrix used for the graph-theoretical analysis were merged into a single pons region (Table 3). The parcellation (HB atlas) was built in the laboratory by combining several atlases and segmentation tools (Table 4).

Node	Nuclei included	Node	Nuclei included
Thal_AV	Anteroventral	Thal_IntC	Centromedian + parafascicular
Thal_LDP	Laterodorsal + lateral posterior	Thal_MDm	Mediodorsal, medial (magnocellular)
Thal_VA	Ventral anterior + ventral anterior magnocellular	Thal_MDl	Mediodorsal, lateral (parvocellular)
Thal_VLA	Ventral lateral anterior	Thal_LGn	Lateral geniculate
Thal_VLP	Ventral lateral posterior	Thal_MSGn	Limitans–suprageniculate + medial geniculate
Thal_VPL	Ventromedial + ventral posterolateral	Thal_PulA / PulI / PulL / PulM	Pulvinar: anterior, inferior, lateral, medial
Thal_IntR	Central medial + central lateral + paracentral		

Table 2. Composition of the thalamic regions. Thalamic nuclei were segmented with FreeSurfer, and neighboring nuclei were combined into 16 regions per hemisphere. Numbers are FreeSurfer label values. Reuniens, paratenial, and reticular nuclei were not included.

Nucleus	Abbreviation	Nucleus	Abbreviation
Pontine nuclei	PN	Abducens nucleus	ABD
Nucleus reticularis tegmenti pontis	NRTP	Facial motor nucleus	FM
Pedunculopontine nucleus	PPN	Superior salivatory nucleus	Ssal
Parabrachial nucleus	PB	Cochlear nuclei	CN
Laterodorsal tegmental nucleus	LDT	Raphe nucleus pontis	RNPON
Principal sensory trigeminal nucleus	TPS	Central superior raphe nucleus	CSR
Trigeminal motor nucleus	TM	Superior olivary complex	SOC

Table 3. Pontine nuclei used in the 139-region matrix for graph-theoretical analysis. Each nucleus is represented in the left and right hemisphere, giving 28 regions. In the 112-region parcellation used for tractography (Table 1), these nuclei are merged into a single pons region.

Anatomical structure	**Tool / Atlas**
Cortex (PFC, M1, PMSMA)	Brodmann-based atlas (MNI space)
Cerebellar cortex	FastSurfer, CerebNet
Thalamic nuclei (AV, LDP, VA, VLA, VLP, VPL, IntR, IntC, MDm, MDl, LGn, MSGn, PulA, PulI, PulL, PulM)	FreeSurfer, recon-all and segmentThalamicNuclei.sh
Basal Ganglia (Caudate, Putamen, Pallidum, Accumbens), Hippocampus, Amygdala	FSL FIRST, run_first_all
Hypothalamus	FreeSurfer, mri_segment_hypothalamic_subunits
Septal nuclei	FreeSurfer, mri_sclimbic_seg
Subthalamic nucleus	https://www.nature.com/articles/s41597-020-00644-6
Claustrum	https://github.com/MezerLab/ClaustrumSegmentation
Brainstem (pons)	FreeSurfer, segmentBS.sh
Arousal structures (mRT, PnO, LC, VTA, PAG)	FreeSurfer, SegmentAAN.sh
Brainstem (RN, SNc, SNr)	https://www.nature.com/articles/sdata201863
Superior colliculus (SC), inferior colliculus (IC), inferior olivary nucleus (ION), vestibular nuclei (Ve)	Navigator_152
Interposed nucleus (IN), fastigial nucleus (FN)	Atlante cerebellare SUIT
Dentate nucleus (DN)	https://github.com/marta-gaviraghi/segmentDN

Table 4. Atlases and tools used to define the regions of the parcellation.

2.2 Cerebellar Structural Connectivity Pathways

2.2.1 Compilation of the Anatomical Reference

The structural connectivity matrix was built from a structured review of anatomical literature. Established connections were first identified from anatomy texts, such as *Essential Clinical Neuroanatomy* (Champney, 2023), which provided the anatomical framework for the regions of interest. Further searches were conducted in PubMed, ScienceDirect, and Google Scholar using combinations of region names, their abbreviations and terms such as projection, afferent, efferent, tract-tracing, and connectivity. AI-assisted literature discovery tools were used to help identify more sources, and every source was read and verified before a connection was encoded. Many of these searches were supplemented by reference anatomy texts, such as E*ssentials of Cerebellum and Cerebellar Disorders* (Gruol et al., 2016) and *The Human Central Nervous System* (Nieuwenhuys, Voogd & van Huijzen, 2008), and by review articles whose reference lists were used to identify primary tracing studies that keyword searching had missed. Studies were read to encode a connection.

Each connection was encoded in a binary directed matrix, in which 1 indicates a direct (monosynaptic) structural projection, including sparse projections, and 0 indicates that no direct projection was documented. Rows represent the regions that send projections (sources), and columns represent the regions that receive them (targets). A value of 0 was assigned when the evidence was just functional, when the pathway was polysynaptic, or when no anatomical evidence was found in the literature. Therefore, a 0 indicates the absence of evidence. The laterality of each projection (ipsilateral, contralateral, or bilateral) was encoded by coding the left and right regions separately. Representing connectivity as a matrix follows the network approach commonly used in connectome research (Bullmore & Sporns, 2009; Hagmann et al., 2007).

2.2.2 Intracerebellar Structural Connections

For the intracerebellar structural connections, the primary anatomical pathway considered was the projection from cerebellar cortex to DCN. Because Purkinje cells are the output neurons of the cerebellar cortex and provide direct inhibitory input to the cerebellar and vestibular nuclei, cerebellar cortex-to-DCN connections were coded in the matrix as directed (inhibitory) pathways linking cortical processing to the principal output structures of the cerebellum (Diedrichsen et al., 2011; Takahashi et al., 2013; Voogd & Glickstein, 1998). Corticonuclear projections follow the well-established mediolateral organization of the cerebellum: the vermal cortex projects predominantly to the FN, the paravermal or intermediate cortex to the IN, and

the lateral hemispheric cortex to the DN (Apps & Garwicz, 2005; Dum & Strick, 2003; Voogd & Glickstein, 1998).

Accordingly, the paravermal portions of anterior-lobe lobules I–V and posterior-lobe lobule VIII were coded as projecting predominantly to the ipsilateral IN, consistent with the classical corticonuclear organization of the intermediate cerebellar cortex (Apps & Garwicz, 2005; Voogd & Glickstein,1998) The lateral hemispheric portions of lobule VI, Crus I, Crus II, and lobule VIIb were coded as projecting predominantly to the ipsilateral DN, consistent with the established projection of the lateral cerebellar hemisphere to that nucleus (Apps & Garwicz, 2005; Dum & Strick, 2003; Voogd & Glickstein, 1998). Lobule VI was additionally assigned an edge to the ipsilateral IN to represent the inclusion of both paravermal and lateral hemispheric territories. Because the hemispheric ROIs include both paravermal and lateral territories, hemispheric lobules I–IV, V, VIIIa, VIIIb and IX were also connected to the ipsilateral DN, and lobules VIIb and IX were also connected to the ipsilateral IN (Voogd & Glickstein,1998). Lobule X (flocculus) was connected to the ipsilateral IN (Voogd & Glickstein, 1998). Because the vermis was represented as a single non-lateralized midline ROI, vermal lobules VI–X were connected to both the left and right FN. (Apps & Garwicz, 2005; Voogd & Glickstein, 1998). Vermal lobule VI was additionally connected to the left and right IN (Apps et al., 2018; Voogd & Glickstein, 1998).

Human structural imaging provides support for this broad topographic organization (Granziera et al., 2009; Steele et al., 2017). However, the detailed corticonuclear topography is derived from tract-tracing and physiological studies in non-human animals (Apps & Garwicz, 2005; Voogd & Glickstein, 1998). In the matrix, these Purkinje cell projections were coded as directed connections from the cerebellar cortex to the DCN.

Adjacency between cerebellar lobules was considered a possible basis for intracortical connectivity. Parallel fibers run mediolaterally along the long axis of each folium for a few millimeters and cross the boundaries between longitudinal zones, but not between lobules (Brand et al., 1976; Voogd & Glickstein, 1998). Basket and stellate cells provide more spatially restricted inhibitory interactions within the cerebellar cortex (Voogd & Glickstein, 1998). These intracortical interactions may support local integration within the cerebellar cortex, but they do not constitute a discrete lobule-to-lobule pathway. Therefore, they were not coded as matrix edges, because anatomical adjacency does not establish a directed structural connection between lobular ROIs. In addition, direct human tracing data at the folial and laminar levels

are limited, and diffusion MRI tractography cannot reliably resolve the fine-scale trajectories of cerebellar intracortical fibers (Lundell & Steele, 2024; Takahashi et al., 2013).

2.2.3 Structural Connectivity Between the Cerebellum and Brainstem Nuclei

The cerebellum is reciprocally connected with numerous brainstem nuclei through afferent pathways to the cerebellar cortex and DCN, as well as through efferent pathways arising primarily from the DCN and, in some cases, directly from the cerebellar cortex.

2.2.3.1 Pons

The pons contains several major brainstem systems that are directly connected with the cerebellum. These include the basilar pontine nuclei (BPN), vestibular nuclei (Ve), the principal sensory (TPS) and motor trigeminal nuclei (TM), the abducens nucleus (ABD), and the parabrachial nucleus (PB). Additional direct cerebellar connections involve the nucleus reticularis tegmenti pontis (NRTP), the oral pontine reticular nucleus (PnO), the pedunculopontine nucleus (PPN), the laterodorsal tegmental nucleus (LDT), the locus coeruleus (LC), the cochlear nuclei (CN), the facial motor nucleus (FM), and the pontine raphe nuclei, including the raphe nucleus pontis (RNPON) and the central superior raphe nucleus (CSR) (Nieuwenhuys et al., 2008; Usunoff et al., 2003). The pons also contains nuclei associated with cranial nerves V, VI, VII, and VIII, although the vestibular and cochlear nuclear complexes extend across the pontomedullary junction rather than being confined exclusively to the pons (Nieuwenhuys et al., 2008; Rahman & Tadi, 2023).

Basilar pontine nuclei

The BPN constitute the principal precerebellar relay of the pons and the major brainstem component of the cortico-ponto-cerebellar pathway. Corticopontine fibers from motor, premotor, prefrontal, parietal, temporal, and visual association cortices terminate in topographically organized territories of the ipsilateral BPN. Pontine neurons subsequently give rise to glutamatergic mossy fibers that predominantly cross the midline and enter the contralateral cerebellum through the middle cerebellar peduncle. The corticopontine projection therefore represents the first stage of the feedforward cerebrocerebellar pathway, while the pontocerebellar projection constitutes its second stage (Glickstein & Doron, 2008; Schmahmann, 2016; Schmahmann & Pandya, 1997).

Anatomical tracing in rodents, cats, and non-human primates demonstrates that the pontocerebellar system is extensive but topographically differentiated. Through axon collaterals, individual pontine territories can project to several separate, non-adjacent regions

of the cerebellar cortex, so that information from one pontine source is distributed across multiple cerebellar cortical territories (Brodal, 1979; Brodal & Bjaalie, 1992; Glickstein et al., 1985; Mihailoff et al., 1985). Pontocerebellar projections reach anterior-lobe lobules, lobule VI, Crus I, Crus II, lobule VIIb, lobules VIIIa and VIIIb, lobule IX, and corresponding vermal territories. Although pontocerebellar axons are predominantly crossed, these projections are bilateral and reach almost all cerebellar lobules except lobule X (flocculus) and vermal lobule X (nodulus) (Hoddevik, 1977; Mihailoff et al., 1985). Therefore, each BPN was linked to both the ipsilateral and the contralateral cerebellar cortical targets, excluding lobule X and vermal lobule X.

Pontocerebellar mossy fibers terminate primarily in the cerebellar granule-cell layer and issue excitatory collaterals to DCN. Consequently, the principal matrix edges from the BPN are directed toward the cerebellar cortex, with additional direct collateral edges to the DN and IN bilaterally and to the contralateral FN where the reviewed evidence identified these nuclear terminations (Cicirata et al., 2005; Oka et al., 1985; Somana & Walberg, 1980). The BPN also receive direct cerebellar nuclear projections, particularly from the DN, with more limited contributions from other DCN territories (Batton et al., 1977; Novello et al., 2024). DCN-to-BPN edges were coded bilaterally for the DN, IN, and FN.

Human evidence for pontocerebellar connectivity relies mainly on post-mortem degeneration studies, diffusion MRI tractography, and cross-species anatomical comparisons because conventional invasive tract tracing is not performed in living humans. Diffusion MRI identifies a rostrocaudal organizational gradient in the human pons and supports connectivity between pontine territories and individual cerebellar lobules, but it does not independently determine synaptic termination, neurotransmitter phenotype, or axonal direction. These imaging results were not used to code edges (Palesi et al., 2017; Rousseau et al., 2022; Yendiki et al., 2022).

Nucleus Reticularis Tegmenti Pontis

The nucleus reticularis tegmenti pontis (NRTP) is a precerebellar nucleus located in the ventromedial pontine tegmentum. It gives rise to direct mossy fiber projections that terminate predominantly in the contralateral cerebellar cortex. Anatomical studies indicate that these projections are widely distributed across the cerebellar cortex. (Brodal, 1980). Accordingly, NRTP to cerebellar cortex connections were included in the reference matrix for hemispheric lobules I–IV, V and VI; Crus I, Crus II and VIIb; hemispheric lobules VIIIa, VIIIb, IX and X;

and vermal lobules VI–IX. Vermis X was excluded because a projection to this region was not supported by the reviewed anatomical evidence (Azizi et al., 1981; Serapide et al., 2002).

NRTP mossy fibers also give rise to direct collaterals terminating in the deep cerebellar nuclei (DCN) (Gibson et al., 2023; Verveer et al., 1997). Tracing studies have identified terminations in the nucleus lateralis, nucleus interpositus, and caudal portion of the nucleus medialis, corresponding respectively to the DN, IN, and FN (Parenti et al., 2002). Therefore, direct NRTP to DCN connections were coded.

NRTP projections to the cerebellar cortex exhibit contralateral predominance, with approximately 60% of NRTP cells projecting contralaterally and 40% projecting ipsilaterally (Cicirata et al., 2005). NRTP to cerebellar connections were therefore entered bilaterally in the reference matrix. Finally, the NRTP also receives direct input from the cerebellar nuclei, reported predominantly from the contralateral DCN (Gibson et al., 2023). Consequently, the reference matrix included both NRTP to cerebellum and cerebellum to NRTP connections, representing a bidirectional anatomical circuit between the NRTP and the cerebellum.

Pontine reticular formation

Pontine reticular regions considered in the literature review of this thesis included the oral pontine reticular nucleus (PnO), caudal pontine reticular nucleus (PnC), and paramedian pontine reticular formation (PPRF). These structures are functionally and anatomically distinct from the NRTP, although terminology and boundaries may differ among species and anatomical atlases.

Oral pontine reticular nucleus

The PnO receives direct but sparse projections from DCN. Tracing studies describe sparse bilateral input from the DN and sparse, predominantly contralateral input from the FN and IN (Shammah-Lagnado et al., 1987). Therefore:

- left and right DN to PnO projections were coded bilaterally
- FN to PnO and interposed to PnO projections were coded contralaterally

Vestibular nuclei

The Ve differ from most precerebellar systems because they send direct mossy fiber projections to the cerebellar cortex and receive direct Purkinje cell output. Some vestibular nuclei therefore function analogously to extracerebellar output nuclei of the vestibulocerebellum (Barmack, 2003). Vestibulocerebellar mossy fibers originate predominantly from the superior, medial, and

inferior Ve and project bilaterally, with ipsilateral predominance, to the flocculus (lobule X), nodulus (vermal lobule X), and uvula (vermal lobule IX) (Barmack, 2003; Rahimi-Balaei et al., 2015). The densest cortical terminations occur in lobules IX and X, with additional projections to lobule VIII and anterior vermal regions (Ando et al., 2020; Barmack, 2003; Epema et al., 1990; Shojaku et al., 1987). Accordingly, the Ve were connected bilaterally to hemispheric lobules IX and X and to vermal lobules IX and X. The Ve were also coded as projecting bilaterally to the DN, IN, and FN (Kebschull et al., 2023).

In the opposite direction, Purkinje cells of the flocculus, nodulus, and uvula project to the superior and medial Ve, and the anterior vermis and vermal lobule VI project to the lateral Ve (Apps et al., 2018; Sadakane et al., 2000; Voogd & Glickstein, 1998). These projections were coded as edges from lobule X and vermal lobules VI, IX, and X to the Ve; the edges from lobule X were coded bilaterally, although the floccular projection is predominantly ipsilateral. The FN and IN were coded as projecting bilaterally to the Ve (Batton et al., 1977).

Cochlear nuclei (CN)

The cochlear nuclei (CN) are reciprocally connected with the vermis. Vermal lobules VI, VII and VIIIa receive bilateral afferents from the CN (Huang, Liu, & Huang, 1982), and the posteroventral cochlear nucleus receives direct fibers from vermal lobules VIII–X (Gacek, 1973). Accordingly, edges were coded from the CN to vermal lobules VI–VIII and from vermal lobules VIII–X to the CN.

Abducens and facial motor nuclei (ABD, FM)

The abducens nucleus (ABD), which controls horizontal eye movements, forms a reciprocal loop with the vestibulocerebellum. It receives projections from the FN, as part of the cerebellar output to brainstem oculomotor centers, and bilateral input from the flocculus (Shin et al., 2011), and in turn sends a minor bilateral projection to the flocculus (Blanks et al., 1983; Rodella et al., 1995). Accordingly, edges were coded between the ABD and lobule X in both directions, and from the FN to the ABD.

The facial motor nucleus (FM) sends bilateral projections, with ipsilateral predominance, to the flocculus, arising from neurons that control the zygomatico-orbital, posterior auricular and temporal muscles (Røste, 1989), and receives input from the contralateral FN (Harper & Heath, 1973; Heath & Harper, 1974). Accordingly, edges were coded from the FM to lobule X bilaterally and from the FN to the contralateral FM.

Trigeminal nuclei

The principal sensory trigeminal nucleus (TPS) sends mossy fibers carrying orofacial sensory information to the cerebellar hemispheres (Ikeda, 1979; Somana et al., 1980). Accordingly, edges were coded from the TPS to ipsilateral Crus I and to Crus II bilaterally. The motor trigeminal nucleus (TM) contains non-motor neurons that project bilaterally to the flocculus (Røste, 1989) and also projects to the DN (Kotchabhakdi & Walberg, 1977). Accordingly, edges were coded from the TM to lobule X and to the DN bilaterally.

Pontine raphe nuclei

The pontine raphe nuclei provide serotonergic input to the cerebellar cortex and nuclei (Bobillier et al., 1976; Pierce et al., 1977). The raphe nucleus pontis (RNPON) projects bilaterally to hemispheric lobules I–IV, Crus I, Crus II and X, to vermal lobules VII, IX and X, and to the DN, IN and FN. The central superior raphe nucleus (CSR) projects bilaterally to hemispheric and vermal lobule IX, to vermal lobule X, to the ipsilateral DN and IN, and to the FN bilaterally (Bobillier et al., 1976; Pierce et al., 1977). In the opposite direction, the RNPON receives input from the contralateral FN (Batton et al., 1977).

Parabrachial nucleus

The parabrachial nucleus (PB) surrounds the superior cerebellar peduncle in the dorsolateral pons and is involved in autonomic, gustatory and nociceptive processing. It is reciprocally connected with the cerebellum. The PB receives projections from the DN, the posterior IN and the FN (Hwang et al., 2023), including ipsilateral projections from the FN (Supple & Kapp, 1994) and from the IN to the lateral and medial PB (Gonzalo-Ruiz et al., 1990). Purkinje cells of vermal lobules VIII–X project directly to the ipsilateral PB, and the PB is reciprocally connected with these lobules (Hashimoto et al., 2018; Sadakane et al., 2000). In addition, the PB sends bilateral noradrenergic projections to the paravermal cortex and to the FN (Dietrichs, 1988). Accordingly, edges were coded from the DN, IN and FN to the PB and from the PB to the DN, IN and FN, together with reciprocal edges between the PB and vermal lobules VIII–X and edges from the PB to the paravermal cortex (Crus I and lobule VIIb).

Pedunculopontine nucleus

The pedunculopontine nucleus (PPN) lies in the pontomesencephalic tegmentum, adjacent to the superior cerebellar peduncle. Axons from the DN and IN form excitatory glutamatergic connections with the PPN. They arise as thin collaterals of cerebellothalamic fibers in the superior cerebellar peduncle and ramify along the entire rostrocaudal extent of the nucleus

(Hazrati & Parent, 1992; Usunoff et al., 2003). In the opposite direction, PPN neurons project to the cerebellar nuclei, particularly the FN, and to the vermal cortex (Usunoff et al., 2003), and cholinergic PPN fibers also reach the DN and IN (Kebschull et al., 2023). Accordingly, edges were coded from the DN and IN to the PPN, and from the PPN to the DN, IN and FN and to vermal lobules VI–X.

Laterodorsal tegmental nucleus

The laterodorsal tegmental nucleus (LDT) is a cholinergic nucleus of the dorsal pontine tegmentum. It sends scarce projections to the cerebellar nuclei, particularly the FN (Usunoff et al., 2003), and cholinergic fibers to the IN (Kebschull et al., 2023). Accordingly, edges were coded from the LDT to the DN, IN and FN.

Locus coeruleus

The locus coeruleus (LC), the main noradrenergic nucleus of the brain, located in the rostral pons, is reciprocally connected with the cerebellum. It projects to the cerebellar cortex and to the DCN bilaterally, with ipsilateral predominance (Dietrichs, 1988; Waterhouse et al., 2022), and receives input from the contralateral FN (Cedarbaum & Aghajanian, 1978; Luppi et al., 1995). Accordingly, the LC was coded as projecting to all cerebellar cortical regions and to the DN, IN and FN of both sides, and as receiving a projection from the contralateral FN.

2.2.3.2 Brainstem Nuclei of the Medulla and Midbrain

Inferior Olive

Another key anatomical connection is the inferior olive (IO) and cerebellum climbing fiber system. The IO is the sole source of climbing fibers and comprises three major divisions, the principal olive, medial accessory olive, and dorsal accessory olive, with each containing further subdivisions whose nomenclature and relative size vary across species (Baizer et al., 2011; Luo et al., 2023). The olivary axons decussate in the brainstem and project predominantly to the contralateral cerebellum. Their main branches ascend as climbing fibers and form powerful excitatory synapses on the proximal dendritic arbors of Purkinje cells in the molecular layer, while axon collaterals terminate in the cerebellar nuclei (T. J. Ruigrok & Voogd, 2000; Sugihara & Shinoda, 2004). Climbing-fiber activation evokes a characteristic complex spike in the postsynaptic Purkinje cell, accompanied by a widespread dendritic calcium signal, and contributes to cerebellar plasticity, motor learning, coordination, and the encoding of behaviorally relevant sensory and performance-related events (Han et al., 2020). This projection is organized with a high degree of topographic precision. Classic tracer,

autoradiographic, and horseradish peroxidase studies showed that these projections align closely with longitudinal Purkinje-cell compartments spanning both hemispheric and vermal cortex. This topographic organization is established during development and extends along the rostrocaudal axis of the cerebellum, linking longitudinal compartments across lobules I–X(Groenewegen et al., 1979; Luo et al., 2023; T. J. H. Ruigrok, 2016; T. J. Ruigrok & Voogd, 2000). Within this map, distinct subnuclei target distinct cerebellar territories: the principal olive innervates lateral hemispheric regions, including Crus I, Crus II, and lobule VI; the medial and dorsal accessory olives target anterior and vermal motor territories, and smaller subdivisions such as the β nucleus and dorsal cap project to lobule X (T. J. H. Ruigrok, 2016; Sugihara & Shinoda, 2004).

The relationship between the IO and cerebellum is not purely feedforward. In addition to the collaterals described above, a subset of neurons in the DCN projects back to the IO via the nucleo-olivary pathway, so that climbing fiber collaterals and nucleo-olivary axons together close a reciprocal olivo-cerebello-olivary loop. This return projection is not uniform across nuclei, reciprocal feedback is provided primarily by crossed projections from the DN and IN to the contralateral IO, whereas FN contributions are comparatively sparse and less consistently lateralized (T. J. Ruigrok & Voogd, 1990, 2000). Because the reported strength, laterality, and terminal distribution of medial nuclear projections vary across olivary territories and experimental species, the fastigial–olivary connection was classified conservatively as bilateral in the binary matrix (Anguat & Cicirata, 1982; Dietrichs & Walberg, 1981; T. J. Ruigrok & Voogd, 2000).

Although direct histological confirmation in humans is limited, a growing body of studies supports the same decussating architecture and longitudinal modularity in the human olivocerebellar system (Patay et al., 2014; Tilikete & Desestret, 2017), reinforcing the view that IO–cerebellum connectivity is anatomically conserved across mammals, including humans.

Red Nucleus

Unlike the IO, the red nucleus (RN) does not provide a significant direct afferent projection to the cerebellar cortex or DCN (Basile et al., 2021). Classic autoradiographic and fluorescent retrograde studies across non-human primates, cats, and rats consistently demonstrate that RN neurons do not terminate in the cerebellum; instead, the RN participates in the Guillain–Mollaret triangle, influencing cerebellar function indirectly via its robust projection to the IO

(Lapresle, 1970). DN projections reach the contralateral parvocellular RN via the superior cerebellar peduncle, and the RN in turn projects through the central tegmental tract to the IO; olivocerebellar climbing fibers then innervate Purkinje cells and reach the contralateral DCN, completing the loop. The RN-to-IO pathway subsequently gives rise to climbing fibers that innervate Purkinje cells as part of the Guillain-Mollaret triangle (Ogut et al., 2023), consistent with the well-established organization of the olivocerebellar system in which the IO is the sole source of climbing fibers synapsing onto Purkinje cells (Zeeuw et al., 1998). No direct monosynaptic RN-to-cerebellum route has been validated (Basile et al., 2021).

Conversely, RN is a major efferent target of both the DN and IN, forming a central hub in cerebellar premotor output (Basile et al., 2021; Cacciola et al., 2019). The magnocellular RN is linked to the IN, whereas the parvocellular RN is linked to the DN (Teune et al., 1995). Each RN receives cerebellar input from the contralateral DN and IN, with IN input dominating rubral motor pathways.

Midbrain Reticular Formation

The midbrain reticular formation (MRF) is a cytoarchitectonically heterogeneous region of the mesencephalic tegmentum comprising multiple interconnected neuronal populations. Anatomical tracing studies have identified predominantly contralateral projections from the DN and IN, and bilateral projections from the FN (Fujita et al., 2020; Judd et al., 2021; Shammah-Lagnado et al., 1987). The reviewed evidence did not provide sufficiently specific support for a direct MRF projection to the cerebellar cortex or nuclei that could be assigned to the ROIs used in the matrix.

Superior colliculus

The superior colliculus (SC) does not contribute a direct mossy or climbing fiber projection to the cerebellum. Animal tracing studies across multiple species indicate that the SC can influence cerebellar processing indirectly through projections to precerebellar structures, including the BPN, NRTP, pontine reticular formation, and IO, which subsequently relay information to the cerebellum (Gayer & Faull, 1988; Isa et al., 2021; Kratochwil et al., 2017). In the reverse direction, however, the SC is a direct target of cerebellar nuclear output, playing a central role in saccade control and visuomotor integration (Quaia et al., 1999). Retrograde tracing in the cat demonstrates that all three DCN project monosynaptically to the deep collicular layers, with a marked contralateral predominance: the DN provides the most substantial projection, terminating densely in the intermediate layers of the rostral contralateral

SC with an additional ipsilateral component; the anterior IN projects to the rostromedial intermediate grey of the contralateral SC; and the caudal FN projects bilaterally to the intermediate and deep layers (Roldan & Reinoso-Suarez, 1981). Accordingly, directed DCN-to-SC edges were encoded for all three nuclei using the nucleus-specific laterality reported in the tracing evidence. The matrix assignments were based primarily on animal anatomical tracing and the direct cerebellar outputs summarized by Novello et al. (2024). Human evidence remains less anatomically specific and was not used independently to determine direction or nucleus of origin.

Ventral tegmental area

The ventral tegmental area (VTA) is a major component of the midbrain dopaminergic circuitry that interacts with the cerebellum through reciprocal direct pathways as well as polysynaptic relays. Anatomical tracing and circuit experiments in rodents demonstrate a monosynaptic excitatory projection from the DCN to the VTA, arising from the DN and IN, which can recruit mesolimbic dopamine circuitry and influence reward and social behavior (Baek et al., 2022; Carta et al., 2019). Tracer studies in rats indicate that VTA neurons project to the cerebellum bilaterally with a slight contralateral predominance, via two anatomically and neurochemically distinct routes. Dopaminergic fibers target the cerebellar cortex, mainly Crus I and the paraflocculus, and to a lesser extent Crus II, terminating predominantly in the granular layer and, less densely, in the Purkinje cell layer, whereas separate non-dopaminergic VTA projections preferentially innervate the DN and IN (Ikai et al., 1992; Snider et al., 1976). Accordingly, the matrix encodes directed DN-to-VTA and IN-to-VTA edges, together with reciprocal VTA-to-cortex edges (Crus I, Crus II, paraflocculus) and VTA-to-DN and VTA-to-IN edges. In humans, direct anatomical evidence for monosynaptic VTA–cerebellar projections remain limited.

Periaqueductal grey

The periaqueductal gray (PAG) is a midbrain tegmental structure consisting of gray matter that surrounds the cerebral aqueduct and extends longitudinally through the midbrain (Bandler et al., 1991). Rather than serving primarily as a source of cerebellar afferents, the PAG is chiefly a target of cerebellar output. Retrograde and anterograde tracing studies demonstrate that the PAG receives cerebellar input arising mainly from the contralateral DN and the posterior IN (Beitz, 1982; Teune et al., 2000). The FN also projects directly to the ventrolateral PAG; while early tracing work described this contribution as comparatively sparse, modern circuit-level

studies using viral tracing and optogenetics have established it as a substantial monosynaptic pathway mediating cerebellar control of fear learning and defensive behavior (Frontera et al., 2020; Lawrenson et al., 2022). Cerebello-PAG connectivity is consistently identified across non-human mammalian tract-tracing studies in rodents and cats, and DCN to PAG edges were accordingly encoded for the DN, IN, and FN.

2.2.4 Cerebellar Thalamic and Subcortical Structural Connections

Thalamus

The cerebellum is strongly connected with the thalamus (Dum & Strick, 2003). Axons arising from the DN and IN leave the cerebellum through the superior cerebellar peduncle, and cross at its decussation in the midbrain before reaching the contralateral thalamus (Sakai et al., 1996). In primates, they terminate mainly in the posterior part of the ventral lateral nucleus (VLp), which corresponds to the oral part of the ventral posterolateral nucleus (VPLo), the caudal part of the ventral lateral nucleus (VLc) and area X in earlier nomenclatures, with additional terminations in the central lateral (CL) intralaminar nucleus (Asanuma et al., 1983b). The cerebellar territory also extends anteriorly into the ventral anterior nucleus (VA) and the anterior part of the ventral lateral nucleus (VLa; VApc and VLo in earlier nomenclatures), where cerebellar and pallidal terminals interdigitate and occasionally overlap (Sakai et al., 1996). Dentate neurons projecting to different cortical areas are topographically organized (Asanuma et al., 1983a; Dum & Strick, 2003), and transneuronal tracing showed that dentate output reaches not only motor but also prefrontal cortex through the caudal ventral lateral thalamus (Middleton & Strick, 1994, 2001).

Beyond the ventral lateral thalamus, cerebellar projections to the mediodorsal nucleus (MD) have been reported in monkeys (Yamamoto et al., 1992), and rodent studies describe weaker or inconsistent projections to other associative and midline nuclei (Novello et al., 2024). In the matrix, DN and IN projections were coded to the contralateral VA, VLa, VLp, ventral posterolateral nucleus (VPL, which in the atlas also includes the ventromedial nucleus), rostral and caudal intralaminar nuclei, lateral (parvocellular) mediodorsal nucleus (MDl) and lateral geniculate nucleus (Kalil, 1981; Nakamura, 2018; Sakai et al., 1996; Stanton, 1980; Yamamoto et al., 1992).

The FN projects bilaterally to the same ventral lateral region, with fewer terminations ipsilaterally (Asanuma et al., 1983a, 1983b). Anterograde tracing in mice showed that FN projections also reach the ventromedial, central lateral, parafascicular and mediodorsal nuclei (Fujita et al., 2020). In the matrix, the FN was coded as projecting to the contralateral VA, MDl

and rostral and caudal intralaminar nuclei, and bilaterally to the VLa, VLp, VPL and the limitans–suprageniculate/medial geniculate region (MSGn) (Asanuma et al., 1983b; Kalil, 1981; Katoh & Deura, 1993; Yamamoto et al., 1992).

Direct projections from the thalamus to the cerebellum have not been established. Instead, the thalamus is connected to the cerebellum indirectly: thalamic nuclei project to the cerebral cortex, which projects to the pontine nuclei, which in turn project to the cerebellar cortex, forming a cerebello-thalamo-cortico-ponto-cerebellar loop (Palesi et al., 2017; Schmahmann & Pandya, 1997). Therefore, no thalamus-to-cerebellum connections were coded.

Together, cerebellar output reaches the thalamus through two partly separate routes: projections from the DN and IN, mainly to the contralateral ventral lateral and ventral anterior nuclei, and projections from the FN, which reach the ventral lateral thalamus on both sides and the intralaminar and mediodorsal nuclei contralaterally.

Hypothalamus

Cerebello-hypothalamic projections arise from all three DCN and reach multiple hypothalamic regions (Novello et al., 2024; Zhu et al., 2006). In the squirrel monkey, HRP/WGA-HRP tracing identified cerebello-hypothalamic projections arising from the FN, IN and DN, with the projection described as predominantly contralateral (Haines & Dietrichs, 1984). Earlier work in the cat described FN projections traveling mainly through uncrossed fibers of the inferior cerebellar peduncle, with primarily ipsilateral terminations in the lateral, posterior, dorsomedial and paraventricular hypothalamic regions (Haroian et al., 1981). A recent review summarizes evidence for direct projections from all DCN to the contralateral ventromedial, dorsomedial and tuberomammillary nuclei (Benagiano & Rizzi, 2024). Given the predominant laterality reported in the tracing literature, DCN-to-hypothalamus connections were coded as contralateral. In the opposite direction, hypothalamic nuclei send fibers, partly histaminergic, to the ipsilateral cerebellar cortex, with collaterals to the DN, IN and FN (Benagiano & Rizzi, 2024). Hypothalamus-to-cerebellar cortex connections were therefore coded as ipsilateral, whereas hypothalamus-to-DCN connections were coded bilaterally.

Basal Ganglia Connections

Structural connectivity between the cerebellum and basal ganglia was also considered to establish whether direct anatomical projections have been reported between the two systems. In mice, viral-tracing experiments demonstrated that neurons in the DN, IN, and FN project directly to the substantia nigra pars compacta (SNc). The FN projection arising mainly from its

ventroposterior part. The DCN projected bilaterally throughout the SNc, targeting about twice as many neurons contralaterally as ipsilaterally; DCN-to-SNc connections were therefore coded bilaterally for each nucleus. These projections form monosynaptic glutamatergic synapses with both dopaminergic and non-dopaminergic SNc neurons (Washburn et al., 2024).

The zona incerta (ZI), a subthalamic region situated ventral to the thalamus, receives input from the cerebellar nuclei. In rats, anatomical tracing demonstrated a prominent projection from the IN to the ZI and a smaller reciprocal projection from the ZI to the IN. The IN-to-ZI projection was mainly contralateral, whereas the ZI-to-IN projection was mainly ipsilateral (Mitrofanis & deFonseka, 2001). More recent experiments in confirmed that cerebellar nuclear neurons project to the ZI through both glutamatergic and GABAergic long-range projections (Zhao et al., 2025). Because the human ZI can be visualized and subdivided on high-resolution MRI (Lau et al., 2020; Saluja et al., 2024), it could be added as a separate region in future versions of the atlas; in the present atlas, however, it was not represented and was therefore not included in the matrix.

2.3 Analysis on Connections

The analysis was performed in two steps. First, the literature-informed anatomical network was characterized by its binary structural connectivity matrix using graph theoretical measures. Second, the same connections were assessed with diffusion MRI tractography by comparing the tractography-derived connections with the literature-informed matrix.

2.3.1 Graph-Theoretical Analysis

The structural binary connectivity matrix included cerebellar cortical lobules, vermal regions, deep cerebellar nuclei, and extracerebellar structures involved in reported cerebellar afferent or efferent pathways. The cerebellar cortical nodes comprised bilateral lobules I–IV, V, VI, Crus I, Crus II, VIIb, VIIIa, VIIIb, IX, and X. Vermal regions VI–X were also included. The DCN included the bilateral DN, IN, FN. Relevant cortical, thalamic, subcortical, midbrain, and brainstem structures were included (Table1). Graph-theoretical analysis was performed at the single-node level. Because the connectivity matrix was binary and directed, measures appropriate for binary directed networks were used. The software used is described in Section 2.4.

Network-level descriptors

Before node-level measures were computed, the network was described using three global descriptors:

- total number of nodes (N)
- total number of directed edges (E)
- directed network density (D)

For a network containing N regions, each entry was defined as:

$$A_{ij} = \begin{matrix} 1, if\ a\ directed\ connection\ from\ node\ i\ to\ node\ j\ was\ represented \\ 0, if\ no\ directed\ connection\ from\ node\ i\ to\ node\ j\ was\ identified \end{matrix}$$

Network density describes how much of the possible connectivity is actually present. In a directed network without self-connections, each of the N nodes can project to each of the other $N - 1$.

For a directed graph without self-connections, density was calculated as the proportion of these possible edges that were represented in the matrix:

$$D = \frac{E}{N(N-1)}$$

Where E is the number of directed edges, and N is the number of nodes.

Density ranges from 0, when no connections are present, to 1, when every region projects to every other region. Because connections in the two directions are counted separately, a reciprocal connection between two regions contributes to two edges (Rubinov & Sporns, 2010).

For each node i, in-degree was calculated as:

$$k_i^{in} = \sum_j A_{ji}$$

In-degree represented the number of directed connections entering the node. Values ranged from 0 to N − 1, with higher in-degree indicating that a region received structural input from a greater number of distinct sources.

Out-degree was calculated as:

$$k_i^{out} = \sum_j A_{ij}$$

Out-degree represented the number of directed connections leaving the node. Values ranged from 0 to N − 1, with higher out-degree indicating that a region distributed structural output to a greater number of distinct targets.

Total directed degree was calculated as:

$$k_i^{total} = k_i^{in} + k_i^{out}$$

Total degree represented the overall number of directed edges associated with the node. Values ranged from 0 to 2(N − 1), with a higher total degree indicating a more extensively connected, highly integrated region within the network.

Local reciprocity was used to quantify the proportion of a node's neighbors with which it shares reciprocal connections, that is, pairs of regions that project to each other $(i \to j \; and \; j \to i)$. :

$$r_i = \frac{n_i^{reciprocal}}{n_i^{unique}}$$

where $n_i^{reciprocal}$ represents the number of neighbors connected to node i in both directions and n_i^{unique} represents the total number of unique neighbors connected to that node in at least one direction. Local reciprocity ranged from 0, when none of a node connections were reciprocated, to 1, when every connection involving that node was bidirectional. Higher values therefore indicate a greater tendency toward mutual, two-way structural coupling with neighboring regions.

Betweenness centrality ranged from 0 to 1 (normalized), with higher values indicating that a node more frequently lays on the shortest paths between other node pairs, reflecting a greater role as a structural bridge within the network. The directed clustering coefficient ranged from 0 to 1, with higher values indicating that a node's neighbors were more interconnected with each other. Trophic level began at 1 for basal, or source, nodes, with higher values indicating a position further downstream in the network's hierarchical flow. Trophic incoherence (F0) summarizes how hierarchical the whole network is: it is 0 in a perfectly hierarchical network, in which every connection points exactly one level up, and approaches 1 when there is no hierarchical organization (MacKay et al., 2020).

2.3.2 MRI Dataset and Participant

MRI data from one healthy participant, identified in the HCP-A dataset as HCA6053758, were obtained from the Lifespan Human Connectome Project in Aging (HCP-A) (Bookheimer et al., 2019; Harms et al., 2018; Yaqiong Chai et al., 2024). The participant was a female and 36.4 years in age at the time of the scan. The HCP Lifespan projects share their data through the NIMH Data Archive (NDA).

The present study used:

1. a structural T1-weighted image for anatomical segmentation, parcellation, and spatial registration.
2. diffusion-weighted MRI data for fiber orientation modelling and tractography.

The purpose of this initial analysis was to evaluate and select a tractography strategy before its potential application to the full study cohort. Therefore, the current investigation was treated as a within-participant methodological comparison and not as a population-level analysis of cerebellar connectivity.

MRI acquisition

Data were acquired on a 3T Siemens Prisma scanner with 80 mT/m gradients (Harms et al., 2018). The T1-weighted image was acquired with a multi-echo MPRAGE sequence at 0.8 mm isotropic resolution. Diffusion-weighted data were acquired at 1.5 mm isotropic resolution with two shells (b = 1500 and 3000 s/mm²; 92–93 directions per shell) and 28 b = 0 volumes, with each direction acquired twice with opposite phase encoding.

The data had been preprocessed with the HCP minimal preprocessing pipelines (Glasser et al., 2013), as adapted for the HCP Lifespan projects (Harms et al., 2018). The preprocessed data were used in this thesis.

2.3.3 Anatomical Parcellation and Regions of Interest

Anatomical regions of interest were defined by combining subject-specific segmentations (FreeSurfer, FastSurfer and FSL) with atlas-based parcellations registered in the subject space (Table 4). The cerebellar cortex was segmented into bilateral hemispheric lobules and vermal regions VI–X (Table 1), and the DCN were defined with the SUIT atlas (interposed and fastigial) and a CNN-based segmentation (dentate). All regions were combined into a single parcellation following the steps in Table 5.

Step	Description
1. Registration	The 0.8 mm T1-weighted image was registered to the MNI152 1 mm template with ANTs (antsRegistrationSyNQuick: rigid, affine and SyN; Avants et al., 2008; Evans et al., 2012); the inverse transform was used to bring the MNI-space atlases into subject space.
2. Alignment of software outputs	FreeSurfer and FastSurfer outputs were aligned to the T1-weighted image with a rigid transform.
3. Interpolation	All label images were resampled with nearest-neighbor interpolation, so that each voxel kept a single integer label.
4. Merging	Subcortical and brainstem regions and the SUIT interposed and fastigial nuclei were combined; where regions overlapped, the voxel was assigned the higher label value.
5. Filling	The pons and then the cerebellar lobules were added only in voxels not already assigned.
6. Resampling	The assembled atlas (0.8 mm) was resampled to the 1.5 mm diffusion space with a rigid transform.
7. Dentate nucleus	The dentate nuclei were segmented at 1.5 mm with a CNN, separated into left and right using the dilated SUIT dentate masks, and added last, taking precedence over any existing label.
8. Cortex and final labeling	The cortical regions (Table 4) were added, and all regions were relabeled to the 112-region scheme (Table 1).

Table 5. Steps used to assemble the parcellation in the subject's space.

2.3.4 Tractography

Seven tractography configurations were generated to evaluate how anatomical constraints, seeding strategy, tracking algorithm, FOD amplitude threshold, and image resolution affected

correspondence with the literature-informed network. Tractography was performed in MRtrix3 (Tournier et al., 2019) on the diffusion data of one HCP-A participant (HCA6053758), acquired at 1.5 mm isotropic resolution. Response functions for white matter, gray matter, and cerebrospinal fluid were estimated from the data (dwi2response msmt_5tt), and FOD were computed with multi-shell multi-tissue constrained spherical deconvolution (lmax = 8) (Jeurissen et al., 2014).

ACT (Smith et al., 2012) requires a 5TT image that defines where streamlines may propagate and terminate. The 5TT image was generated from the T1-weighted image with FSL-based segmentation (5ttgen FSL). In the standard segmentation, the nucleus accumbens, caudate, globus pallidus, putamen, thalamus, amygdala, and hippocampus were classified as subcortical gray matter. Because this segmentation does not represent DCN, brainstem nuclei, hypothalamus, septal nuclei, subthalamic nucleus and claustrum as gray matter, a modified 5TT image was also created by adding masks of these regions to the subcortical gray matter tissue (5ttedit), so that streamlines could terminate within them. For each image, the gray matter–white matter (GM-WM) interface used for seeding was derived with 5tt2gmwmi.

The FOD amplitude cutoff sets the minimum fiber orientation amplitude a streamline needs to continue, a higher cutoff stops the streamlines earlier and makes tracking more conservative. The default cutoff is 0.05, and a value of 0.06 was also tested. Seeds were placed either at the GM-WM interface (Smith et al., 2012), so that streamlines start where connections originate, or dynamically (Smith et al., 2015), where new seeds are placed preferentially in regions that are under-represented by the current streamlines.

The seven configurations used were the following (Table 6):

1. ***No ACT***: probabilistic tracking (iFOD2) without anatomical constraints, with seeds placed dynamically. Without ACT, the default FOD amplitude cutoff of 0.1 was applied.

2. ***Traditional ACT***: probabilistic tractography with ACT (Smith et al., 2012) was performed using a standard 5TT image, in which the subcortical gray matter mask included the structures define in the standard segmentation, including the amygdala and hippocampus. Seeds were placed at the gray matter–white matter (GM-WM) interface, and the default cutoff of 0.05 was used.

3. ***GM-WM seeding, default cutoff****:* identical to traditional ACT, but using the modified 5TT image in which the brainstem nuclei, DCN, hypothalamus, septal nuclei, subthalamic nucleus

and claustrum were also defined as deep gray matter, so that streamlines could terminate within them.

4. ***GM-WM seeding, cutoff 0.06***: identical to configuration 3, with a stricter FOD amplitude cutoff of 0.06, so that streamlines stop earlier in regions of low fiber orientation amplitude.

5. ***GM-WM seeding, 0.8 mm***: identical to configuration 3, after passing the diffusion data from 1.5 mm to 0.8 mm isotropic resolution; the 5TT image and seeding interface were recreated at this resolution. This configuration was included to test whether reconstructing streamlines on a finer voxel grid improves the separation of small, neighboring structures such as the cerebellar lobules and DCN (Dyrby et al., 2014).

6. ***Dynamic seeding****:* identical to configuration 3, but with seeds placed dynamically, preferentially in regions under-represented by the streamlines already generated (Smith et al., 2015).

7. ***Deterministic***: identical to configuration 3, but using the deterministic SD_STREAM algorithm (Tournier et al., 2012), which follows the single most likely fiber orientation at each step instead of sampling from the orientation distribution. Backtracking is not available for this algorithm, and its default step size (0.15 mm) and maximum angle (60°) were used.

#	**Configuration**	**Algorithm**	**ACT tissue image**	**Seeding**	**FOD cutoff**	**Backtracking**	**Resolution (step size)**
1	*No ACT*	iFOD2	none	dynamic	0.10 (default without ACT)	—	1.5 mm (0.75 mm)
2	*Traditional ACT*	iFOD2	standard 5TT (+ amygdala, hippocampus)	GM-WM interface	0.05 (default)	yes	1.5 mm (0.75 mm)

3	*GM-WM default*	iFOD2	modified 5TT (+ brainstem nuclei, DCN, hypothalamus, septal nuclei, subthalamic nucleus, claustrum)	GM-WM interface	0.05 (default)	yes	1.5 mm (0.75 mm)
4	*GM-WM 0.06*	iFOD2	modified 5TT	GM-WM interface	0.06	yes	1.5 mm (0.75 mm)
5	*GM-WM 0.8 mm*	iFOD2	modified 5TT at 0.8 mm	GM-WM interface	0.05	yes	0.8 mm (0.4 mm)
6	*Dynamic seeding*	iFOD2	modified 5TT	dynamic	0.05	yes	1.5 mm (0.75 mm)
7	*Deterministic*	SD_STREAM	modified 5TT	GM-WM interface	0.05	no	1.5 mm (0.15 mm; max angle 60°)

Table 6. Overview of the seven tractography configurations.

For each tractography configuration, 30 million streamlines were generated, and each streamline was assigned to pairs of regions of the 112-region parcellation using the MRtrix3 command tck2connectome, which assigns each streamline to the two regions in which its endpoints terminate and saves these assignments to a file. The streamlines connecting each pair of regions were then extracted with connectome2tck (option -exclusive), yielding one streamline file per connected pair. To remove connections supported by very few streamlines, each file was converted into a track-density map on the participant's T1-weighted image at 1.5 mm isotropic resolution (tckmap), and voxels traversed by fewer than five streamlines were set to zero (fslmaths). Connections with no remaining voxel above this threshold were discarded.

2.3.5 Comparison with Literature-Based Connectivity

Tractography cannot determine the direction of a connection. Therefore, the directed literature-derived matrix was converted into an undirected reference, in which two regions were considered connected if a projection was documented in at least one direction. The comparison was performed using the 112-region parcellation used for tractography (Table 1; Section 2.3.3). To match this parcellation, the 28 nuclei of the pons represented separately in the binary structural connectivity matrix (Table 3) were merged into a single pons region. For each tractography configuration, each connection (i.e., each pair of regions) was classified according to the agreement between the reference matrix and tractography as:

- **True positive (TP)**: connected in the reference matrix and reconstructed by tractography.
- **False positive (FP)**: reconstructed by tractography but not connected in the reference matrix.
- **False negative (FNe)**: present in the reference matrix but not reconstructed by tractography.
- **True negative (TN)**: absent from both the reference matrix and the tractography results.

Two summary measures were derived from these four categories. First, the F1 score which is a harmonic mean of precision and sensitivity, and itt indicates how well a configuration reconstructs the correct connections while avoiding incorrect ones, but it does not account for true negatives. Youden's J combines sensitivity and specificity (J = sensitivity + specificity − 1) and therefore considers both the connections that should be present and those that should be absent (Youden, 1950). J ranges from −1 to 1, where 0 indicates performance no better than chance and 1 a perfect agreement with the reference. The comparison was performed in two analyses. The first, which is the main analysis of this thesis, focused on the cerebellum and included all pairs of regions in which at least one region belonged to the cerebellum. The second analysis included the whole matrix to identify the best performing tractography configuration overall. In addition to the cerebellar connections, it included connections between brainstem regions and between the brainstem and other brain regions. Pairs in which both regions belonged to the cerebral cortex, thalamus, hypothalamus or other subcortical regions (nodes 1–58) were excluded, because connections among these regions were not part of the literature review.

The metrics were calculated using all possible pairs of regions within each analysis, not over the connections reconstructed by each configuration. With 112 regions, there are 6,216 possible pairs (112 × 111 / 2). The cerebellar analysis included only pairs involving at least one cereebellar region (2,976 pairs). The whole-matrix analysis included all pairs except those between two of the first 58 regions (cortical, thalamic and other subcortical regions), whose connections with each other were not part of the literature review (4,563 pairs).

For each of the seven configurations, performance in each analysis, was evaluated with the following measures:

$$\text{Sensitivity} = \frac{TP}{TP + FNe}$$

$$Specificity = \frac{TN}{TN + FP}$$

$$Precision = \frac{TP}{TP + FP}$$

$$F1 = \frac{2 \times Precision \times Sensitivity}{Precision + Sensitivity}$$

$$Youden's = Sensitivity + Specificity - 1$$

Sensitivity, specificity, precision, and F1 range from 0 to 1, where 1 indicates perfect performance. Youden's J ranges from −1 to 1, where 0 indicates performance no better than chance and 1 indicates a perfect classification (Youden, 1950). Sensitivity measures describe the proportion of reference connections recovered by tractography, specificity the proportion of absent connections correctly left unreconstructed, precision the proportion of reconstructed connections supported by the reference, and F1 the balance between precision and sensitivity.

The best-performing configuration was defined as the one with the highest Youden's J, because this measure weighs equal the recovery of literature-supported connections (sensitivity) and the correct rejection of unsupported connections (specificity). As only one participant was

included, the analysis aimed to identify a promising configuration for future validation in the broader cohort, rather than perform inferential statistical testing.

Sources of Disagreement and Streamline Counts

To characterize the discrepancies between the tractography results and the reference matrix, the pairs of false positives (FP) and false negatives (FNe) in the cerebellar analysis were classified based on the regions they connected. This analysis was performed for the three configurations with the highest Youden's J index value. The categories included: (1) pairs of cortical regions in the cerebellum; (2) pairs connecting the cerebellar cortex to a DCN; (3) pairs of DCNs; (4) cerebellum-thalamus pairs; (5) pairs connecting a cerebellar region to the hypothalamus and brainstem nuclei.

For each configuration, the percentage of false positives in each connection category was calculated as the number of false positives (in that category) divided by the total number of false positives. The same procedure was applied to false negatives.

In addition, the streamlines of selected reference connections of anatomical interest were examined. This included left crus to left DN, right hypothalamus to right DN, Vermis VII to left FN, left hypothalamus to left IN, left Ve to vermis IX, left DN to right VLp, right FN to right VLa, and left LC to right IN. For each connection and configuration, the streamline file extracted with connectome2tck (Section 2.3.4), and its number of streamlines was counted with tckinfo (MRtrix3; Tournier et al., 2019).

2.4 Software

All analyses were performed with the software listed in Table 7. Graph-theoretical measures were computed in Python in Google Colaboratory, using pandas (McKinney, 2010), NumPy (Harris et al., 2020) and NetworkX (Hagberg et al., 2008). Degree, local reciprocity and network density were computed directly from the adjacency matrix. Local reciprocity was defined as the proportion of a region's connected neighbors with which it shares connections in both directions. Betweenness centrality was computed with NetworkX and normalized by the number of possible node pairs (Freeman, 1977), and the clustering coefficient was computed in its directed form (Fagiolo, 2007). Trophic levels are not available in standard network toolboxes and were computed following MacKay, Johnson and Sansom (2020). Measure definitions followed Rubinov and Sporns (2010). Tractography was performed with MRtrix3 (Tournier et al., 2019), and the comparison between tractography and the literature-

derived matrix was performed in Microsoft Excel. Figures of the connectivity matrix were drawn with Matplotlib (Hunter, 2007).

Software	Version	Purpose
Python	3.13.15	Programming language for the graph-theoretical analyses, run in Google Colaboratory
pandas	2.2.3	Loading the connectivity matrix from Excel and validating its structure (square shape, matching labels, binary entries)
NumPy	2.1.3	Building the adjacency matrix and computing degree, local reciprocity, density and trophic level
NetworkX	3.6.1	Computing betweenness centrality and the directed clustering coefficient
Matplotlib	3.10.0	Drawing the connectograms in the Results section
MRtrix3	3.0.8	Tractography (tckgen, tck2connectome, connectome2tck, tckmap) and visualization (mrview)
Microsoft Excel	2609	Comparing tractography with the literature-derived matrix and computing the evaluation metrics (TP, FP, FN, TN, sensitivity, specificity, precision, F1, Youden's J)

Table 7. Software used for matrix construction, graph-theoretical analysis, tractography, and figure generation.

3. Results

3.1 Literature-Derived Binary Structural Connectivity Matrix

The literature-derived binary structural connectivity matrix comprised 139 nodes divided into: 31 cerebellar nodes (25 cortical lobules and 6 deep cerebellar nuclei), 6 cerebral cortical nodes, 50 brainstem nodes, 32 thalamic nodes, and 20 additional subcortical nodes. This thesis focused on projections from and to the cerebellum, in which the complete matrix had a total of 1876 connections, in which 699 involve the cerebellum. The 699 cerebellar connections split into 46 within the cerebellum, 232 efferent and 421 afferents. The following tables show the intracerebellar connections (Table 8), cerebellar projections from and to the brainstem (Table 9-11), and cerebellar connections with thalamic and subcortical regions (Table 12) (Figure 3). There were no monosynaptic direct connections with the cerebral cortex, the 6 nodes analyzed for the cortex are PFC_L, M1_L, PMSMA_L, PFC_R, M1_R, and PMSMA_R, as mentioned efferents and afferents are 0s.

Intracerebellar Connectivity

	DN R	IN R	FN R	DN L	IN L	FN L
L I-IV R	1	1	0	0	0	0
L V R	1	1	0	0	0	0
L VI R	1	1	0	0	0	0
C I R	1	0	0	0	0	0
C II R	1	0	0	0	0	0
L VIIb R	1	1	0	0	0	0
L VIIIa R	1	1	0	0	0	0
L VIIIb R	1	1	0	0	0	0
L IX R	1	1	0	0	0	0
L X R	0	1	0	0	0	0
V VI	0	1	1	0	1	1
V VII	0	0	1	0	0	1
V VIII	0	0	1	0	0	1
V IX	0	0	1	0	0	1
V X	0	0	1	0	0	1
DN R		0	0	0	0	0
IN R	0		0	0	0	0
FN R	0	0		0	0	0
L I-IV L	0	0	0	1	1	0
L V L	0	0	0	1	1	0
L VI L	0	0	0	1	1	0
C I L	0	0	0	1	0	0
C II L	0	0	0	1	0	0
L VIIb L	0	0	0	1	1	0
L VIIIa L	0	0	0	1	1	0
L VIIIb L	0	0	0	1	1	0
L IX L	0	0	0	1	1	0
L X L	0	0	0	0	1	0
DN L	0	0	0		0	0
IN L	0	0	0	0		0
FN L	0	0	0	0	0	

Table 8. Intracerebellar structural connectivity matrix. The matrix above is a binary summary of the intracerebellar connections based on literature research.

Cerebellum Connectivity Between Brainstem and Other Subcortical Areas

	RN L	SNC L	SNR L	SC L	IC L	mRT L	LC L	IO L	VN L	PnO L	VTA	PAG	Pons L	NRTP L	PPN L	PbC L	LDT L	TPS L	TM L	ABD L	FM L	SSN L	CN L	RNPON L	CSR L	SOC L
L I-IV L	0	0	0	0	0	0	0	0	0	0	0	0	0	0	0	0	0	0	0	0	0	0	0	0	0	0
L V L	0	0	0	0	0	0	0	0	0	0	0	0	0	0	0	0	0	0	0	0	0	0	0	0	0	0
L VI L	0	0	0	0	0	0	0	0	0	0	0	0	0	0	0	0	0	0	0	0	0	0	0	0	0	0
C I L	0	0	0	0	0	0	0	0	0	0	1	0	0	0	0	0	0	0	0	0	0	0	0	0	0	0
C II L	0	0	0	0	0	0	0	0	0	0	1	0	0	0	0	0	0	0	0	0	0	0	0	0	0	0
L VIIb L	0	0	0	0	0	0	0	0	0	0	0	0	0	0	0	0	0	0	0	0	0	0	0	0	0	0
L VIIIa L	0	0	0	0	0	0	0	0	0	0	0	0	0	0	0	0	0	0	0	0	0	0	0	0	0	0
L VIIIb L	0	0	0	0	0	0	0	0	0	0	0	0	0	0	0	0	0	0	0	0	0	0	0	0	0	0
L IX L	0	0	0	0	0	0	0	0	0	0	1	0	0	0	0	0	0	0	0	0	0	0	0	0	0	0
L X L	0	0	0	0	0	0	0	0	1	0	0	0	0	0	0	0	0	0	0	1	0	0	0	0	0	0
DN L	0	1	0	1	0	0	0	0	0	1	1	1	1	1	1	1	0	0	0	0	0	0	0	0	1	0
IN L	0	1	0	0	0	0	0	0	1	0	1	1	1	1	1	1	0	0	0	0	0	0	0	0	1	0
FN L	0	1	0	1	0	1	0	1	1	0	0	1	1	1	0	1	0	0	0	1	0	0	0	0	0	0
V VI	0	0	0	0	0	0	0	0	0	0	0	1	0	0	0	0	0	0	0	0	0	0	0	0	0	0
V VII	0	0	0	0	0	0	0	0	0	0	0	0	0	0	0	0	0	0	0	0	0	0	0	0	0	0
V VIII	0	0	0	0	0	0	0	0	0	0	0	1	0	0	0	1	0	0	0	0	0	0	1	0	0	0
V IX	0	0	0	0	0	0	0	0	1	0	0	1	0	0	0	1	0	0	0	0	0	0	1	0	0	0
V X	0	0	0	0	0	0	0	0	1	0	0	1	0	0	0	1	0	0	0	0	0	0	1	0	0	0
DN R	1	1	0	1	1	1	0	1	0	1	1	1	1	1	1	1	0	0	0	0	0	0	0	0	1	0
IN R	1	1	0	1	1	1	0	1	1	1	1	1	1	1	1	1	0	0	0	0	0	0	0	0	1	0
FN R	0	1	0	1	1	1	1	1	1	1	0	1	1	1	0	1	0	0	0	1	1	0	0	1	0	0
L I-IV R	0	0	0	0	0	0	0	0	0	0	0	0	0	0	0	0	0	0	0	0	0	0	0	0	0	0
L V R	0	0	0	0	0	0	0	0	0	0	0	0	0	0	0	0	0	0	0	0	0	0	0	0	0	0
L VI R	0	0	0	0	0	0	0	0	0	0	0	0	0	0	0	0	0	0	0	0	0	0	0	0	0	0
C I R	0	0	0	0	0	0	0	0	0	0	1	0	0	0	0	0	0	0	0	0	0	0	0	0	0	0
C II R	0	0	0	0	0	0	0	0	0	0	1	0	0	0	0	0	0	0	0	0	0	0	0	0	0	0
L VIIb R	0	0	0	0	0	0	0	0	0	0	0	0	0	0	0	0	0	0	0	0	0	0	0	0	0	0
L VIIIa R	0	0	0	0	0	0	0	0	0	0	0	0	0	0	0	0	0	0	0	0	0	0	0	0	0	0
L VIIIb R	0	0	0	0	0	0	0	0	0	0	0	0	0	0	0	0	0	0	0	0	0	0	0	0	0	0
L IX R	0	0	0	0	0	0	0	0	0	0	1	0	0	0	0	0	0	0	0	0	0	0	0	0	0	0
L X R	0	0	0	0	0	0	0	0	1	0	0	0	0	0	0	0	0	0	0	1	0	0	0	0	0	0

Table 9. Cerebellar projections to the left brainstem. Rows show cerebellar sources, and columns show left brainstem targets, including the midline VTA and PAG. Cells containing "1" denote established monosynaptic projections.

	RN R	SNC R	SNR R	SC R	IC R	mRT R	LC R	IO R	VN R	PnO R	Pons R	NRTP R	PPN R	PbC R	LDT R	TPS R	TM R	ABD R	FM R	SSN R	CN R	RNPON R	CSR R	SOC R
L I-IV L	0	0	0	0	0	0	0	0	0	0	0	0	0	0	0	0	0	0	0	0	0	0	0	0
L V L	0	0	0	0	0	0	0	0	0	0	0	0	0	0	0	0	0	0	0	0	0	0	0	0
L VI L	0	0	0	0	0	0	0	0	0	0	0	0	0	0	0	0	0	0	0	0	0	0	0	0
C I L	0	0	0	0	0	0	0	0	0	0	0	0	0	0	0	0	0	0	0	0	0	0	0	0
C II L	0	0	0	0	0	0	0	0	0	0	0	0	0	0	0	0	0	0	0	0	0	0	0	0
L VIIb L	0	0	0	0	0	0	0	0	0	0	0	0	0	0	0	0	0	0	0	0	0	0	0	0
L VIIIa L	0	0	0	0	0	0	0	0	0	0	0	0	0	0	0	0	0	0	0	0	0	0	0	0
L VIIIb L	0	0	0	0	0	0	0	0	0	0	0	0	0	0	0	0	0	0	0	0	0	0	0	0
L IX L	0	0	0	0	0	0	0	0	0	0	0	0	0	0	0	0	0	0	0	0	0	0	0	0
L X L	0	0	0	0	0	0	0	0	1	0	0	0	0	0	0	0	0	1	0	0	0	0	0	0
DN L	1	1	0	1	0	1	0	1	0	1	1	1	1	1	0	0	0	0	0	0	0	0	1	0
IN L	1	1	0	1	0	1	0	1	1	1	1	1	1	1	0	0	0	0	0	0	0	0	1	0
FN L	0	1	0	1	0	1	1	1	1	1	1	1	0	1	0	0	0	1	1	0	0	1	0	0
V VI	0	0	0	0	0	0	0	0	1	0	0	0	0	0	0	0	0	0	0	0	0	0	0	0
V VII	0	0	0	0	0	0	0	0	0	0	0	0	0	0	0	0	0	0	0	0	0	0	0	0
V VIII	0	0	0	0	0	0	0	0	0	0	0	0	0	1	0	0	0	0	0	0	1	0	0	0
V IX	0	0	0	0	0	0	0	0	1	0	0	0	0	1	0	0	0	0	0	0	1	0	0	0
V X	0	0	0	0	0	0	0	0	1	0	0	0	0	1	0	0	0	0	0	0	1	0	0	0
DN R	0	1	0	1	0	0	0	0	0	1	1	1	1	1	0	0	0	0	0	0	0	0	1	0
IN R	0	1	0	0	0	0	0	0	1	0	1	1	1	1	0	0	0	0	0	0	0	0	1	0
FN R	0	1	0	1	0	1	0	1	1	0	1	1	0	1	0	0	0	1	0	0	0	0	0	0
L I-IV R	0	0	0	0	0	0	0	0	0	0	0	0	0	0	0	0	0	0	0	0	0	0	0	0
L V R	0	0	0	0	0	0	0	0	0	0	0	0	0	0	0	0	0	0	0	0	0	0	0	0
L VI R	0	0	0	0	0	0	0	0	0	0	0	0	0	0	0	0	0	0	0	0	0	0	0	0
C I R	0	0	0	0	0	0	0	0	0	0	0	0	0	0	0	0	0	0	0	0	0	0	0	0
C II R	0	0	0	0	0	0	0	0	0	0	0	0	0	0	0	0	0	0	0	0	0	0	0	0
L VIIb R	0	0	0	0	0	0	0	0	0	0	0	0	0	0	0	0	0	0	0	0	0	0	0	0
L VIIIa R	0	0	0	0	0	0	0	0	0	0	0	0	0	0	0	0	0	0	0	0	0	0	0	0
L VIIIb R	0	0	0	0	0	0	0	0	0	0	0	0	0	0	0	0	0	0	0	0	0	0	0	0
L IX R	0	0	0	0	0	0	0	0	0	0	0	0	0	0	0	0	0	0	0	0	0	0	0	0
L X R	0	0	0	0	0	0	0	0	1	0	0	0	0	0	0	0	0	1	0	0	0	0	0	0

Table 10. Cerebellar projections to the right brainstem. Rows show cerebellar sources, and columns show right brainstem targets. 1 represents a connection is present.

	L I-IV L	L V L	L VI L	C I L	C II L	L VIIb L	L VIIa L	L VIIb L	L IX L	L X L	DN L	IN L	FN L	V VI	V VII	V VIII	V IX	V X	L I-IV R	L V R	L VI R	C I R	C II R	L VIIb R	L VIIa R	L VIIb R	L IX R	L X R	DN R	IN R	FN R
RN L	0	0	0	0	0	0	0	0	0	0	0	0	0	0	0	0	0	0	0	0	0	0	0	0	0	0	0	0	1	0
SNc L	0	0	0	0	0	0	0	0	0	0	0	0	0	0	0	0	0	0	0	0	0	0	0	0	0	0	0	0	0	0
SNr L	0	0	0	0	0	0	0	0	0	0	0	0	0	0	0	0	0	0	0	0	0	0	0	0	0	0	0	0	0	0
SC L	0	0	0	0	0	0	0	0	0	0	0	0	0	0	0	0	0	0	0	0	0	0	0	0	0	0	0	0	0	0
IC L	0	0	0	0	0	0	0	0	0	0	0	0	0	0	0	0	0	0	0	0	0	0	0	0	0	0	0	0	0	0
mRT L	0	0	0	0	0	0	0	0	0	0	0	0	0	0	0	0	0	0	0	0	0	0	0	0	0	0	0	0	0	1
LC L	1	1	1	1	1	1	1	1	1	1	1	1	1	1	1	1	1	1	1	1	1	1	1	1	1	1	1	1	1	1
ION L	0	0	0	0	0	0	0	0	0	0	0	0	0	1	1	1	1	1	1	1	1	1	1	1	1	1	1	1	1	1
Ve L	0	0	0	0	0	0	0	0	1	1	1	1	1	0	0	0	1	1	0	0	0	0	0	0	0	0	1	1	1	1
PnO L	0	0	0	0	0	0	0	0	0	0	0	0	0	0	0	0	0	0	0	0	0	0	0	0	0	0	0	0	0	0
BPN L	1	1	1	1	1	1	1	1	1	0	1	1	0	1	1	1	1	0	1	1	1	1	1	1	1	1	1	0	1	1
NRTP L	0	0	0	0	0	0	0	0	0	0	1	1	1	1	1	1	1	0	1	1	1	1	1	1	1	1	1	1	1	1
PPN L	0	0	0	0	0	0	0	0	0	0	1	1	1	1	1	1	1	1	0	0	0	0	0	0	0	0	0	1	1	1
Pb L	0	0	0	1	0	1	0	0	0	0	1	1	1	0	0	1	1	1	0	0	0	1	0	1	0	0	0	0	1	1	1
LDT L	0	0	0	0	0	0	0	0	0	0	1	1	1	0	0	0	0	0	0	0	0	0	0	0	0	0	0	1	1	1
TPS L	0	0	0	1	1	0	0	0	0	0	0	0	0	0	0	0	0	0	0	0	0	0	1	0	0	0	0	0	0	0
TM L	0	0	0	0	0	0	0	0	0	1	1	0	0	0	0	0	0	0	0	0	0	0	0	0	0	0	0	1	1	0	0
ABD L	0	0	0	0	0	0	0	0	0	1	0	0	1	0	0	0	0	0	0	0	0	0	0	0	0	0	0	1	0	0	1
FM L	0	0	0	0	0	0	0	0	0	1	0	0	0	0	0	0	0	0	0	0	0	0	0	0	0	0	0	1	0	0	0
SSN L	0	0	0	0	0	0	0	0	0	0	0	0	0	0	0	0	0	0	0	0	0	0	0	0	0	0	0	0	0	0	0
CN L	0	0	0	0	0	0	0	0	0	0	0	0	0	1	1	1	0	0	0	0	0	0	0	0	0	0	0	0	0	0	0
RNPON L	1	0	0	1	1	0	0	0	0	1	1	1	1	0	1	0	1	1	1	0	0	1	1	0	0	0	0	1	1	1	1
CSR L	0	0	0	0	0	0	0	0	1	0	1	1	1	0	0	0	1	1	0	0	0	0	0	0	0	0	1	0	0	0	1
SOC L	0	0	0	0	0	0	0	0	0	0	0	0	0	0	0	0	0	0	0	0	0	0	0	0	0	0	0	0	0	0	0
Hypo L	1	1	1	1	1	1	1	1	1	1	1	1	1	1	1	1	1	1	0	0	0	0	0	0	0	0	0	1	1	1
VTA	0	0	0	1	1	0	0	0	1	0	1	1	1	0	0	1	1	1	0	0	0	1	1	0	0	0	1	0	1	1	1
PAG	0	0	0	0	0	0	0	0	0	0	1	1	1	0	0	0	0	0	0	0	0	0	0	0	0	0	0	0	1	1	1
RN R	0	0	0	0	0	0	0	0	0	0	0	1	0	0	0	0	0	0	0	0	0	0	0	0	0	0	0	0	0	0	0
SNc R	0	0	0	0	0	0	0	0	0	0	0	0	0	0	0	0	0	0	0	0	0	0	0	0	0	0	0	0	0	0	0
SNr R	0	0	0	0	0	0	0	0	0	0	0	0	0	0	0	0	0	0	0	0	0	0	0	0	0	0	0	0	0	0	0
SC R	0	0	0	0	0	0	0	0	0	0	0	0	0	0	0	0	0	0	0	0	0	0	0	0	0	0	0	0	0	0	0
IC R	0	0	0	0	0	0	0	0	0	0	0	0	0	0	0	0	0	0	0	0	0	0	0	0	0	0	0	0	0	0	0
mRT R	0	0	0	0	0	0	0	0	0	0	0	0	1	0	0	0	0	0	0	0	0	0	0	0	0	0	0	0	0	0	0
LC R	1	1	1	1	1	1	1	1	1	1	1	1	1	1	1	1	1	1	1	1	1	1	1	1	1	1	1	1	1	1	1
ION R	1	1	1	1	1	1	1	1	1	1	1	1	1	1	1	1	1	1	0	0	0	0	0	0	0	0	0	0	0	0	0
Ve R	0	0	0	0	0	0	0	0	1	1	1	1	1	0	0	0	1	1	0	0	0	0	0	0	0	0	1	1	1	1	1
PnO R	0	0	0	0	0	0	0	0	0	0	0	0	0	0	0	0	0	0	0	0	0	0	0	0	0	0	0	0	0	0	0
BPN R	1	1	1	1	1	1	1	1	1	0	1	1	1	1	1	1	1	0	1	1	1	1	1	1	1	1	1	0	1	1	0
NRTP R	1	1	1	1	1	1	1	1	1	1	1	1	1	1	1	1	1	0	0	0	0	0	0	0	0	0	0	0	1	1	1
PPN R	0	0	0	0	0	0	0	0	0	0	1	1	1	1	1	1	1	1	0	0	0	0	0	0	0	0	0	0	1	1	1
Pb R	0	0	0	1	0	1	0	0	0	0	1	1	1	0	0	1	1	1	0	0	0	1	0	1	0	0	0	0	1	1	1
LDT R	0	0	0	0	0	0	0	0	0	0	1	1	1	0	0	0	0	0	0	0	0	0	0	0	0	0	0	0	1	1	1
TPS R	0	0	0	0	1	0	0	0	0	0	0	0	0	0	0	0	0	0	0	0	0	0	1	1	0	0	0	0	0	0	0
TM R	0	0	0	0	0	0	0	0	0	1	1	0	0	0	0	0	0	0	0	0	0	0	0	0	0	0	0	1	1	0	0
ABD R	0	0	0	0	0	0	0	0	0	1	0	0	1	0	0	0	0	0	0	0	0	0	0	0	0	0	0	1	0	0	1
FM R	0	0	0	0	0	0	0	0	0	1	0	0	0	0	0	0	0	0	0	0	0	0	0	0	0	0	0	1	0	0	0
SSN R	0	0	0	0	0	0	0	0	0	0	0	0	0	0	0	0	0	0	0	0	0	0	0	0	0	0	0	0	0	0	0
CN R	0	0	0	0	0	0	0	0	0	0	0	0	0	1	1	1	0	0	0	0	0	0	0	0	0	0	0	0	0	0	0
RNPON R	1	0	0	1	1	0	0	0	0	1	1	1	1	0	1	0	1	1	1	0	0	1	1	0	0	0	0	1	1	1	1
CSR R	0	0	0	0	0	0	0	0	1	0	0	0	1	0	0	0	1	1	0	0	0	0	0	0	0	0	1	0	1	1	1
SOC R	0	0	0	0	0	0	0	0	0	0	0	0	0	0	0	0	0	0	0	0	0	0	0	0	0	0	0	0	0	0	0
Hypo R	0	0	0	0	0	0	0	0	0	0	1	1	1	1	1	1	1	1	1	1	1	1	1	1	1	1	1	1	1	1	1

Table 11. Binary matrix of projections from brainstem nuclei and hypothalamus to cerebellum.

	Hypo L	AV L	LDP L	VA L	VLa L	VLp L	VPL L	IntR L	IntC L	MDm L	MDl L	LGn L	MSGn L	PulA L	PulI L	PulL L	PulM L	Hypo R	AV R	LDP R	VA R	VLa R	VLp R	VPL R	IntR R	IntC R	MDm R	MDl R	LGn R	MSGn R	PulA R	PulI R	PulL R	PulM R
L I-IV L	0	0	0	0	0	0	0	0	0	0	0	0	0	0	0	0	0	0	0	0	0	0	0	0	0	0	0	0	0	0	0	0	0	0
L V L	0	0	0	0	0	0	0	0	0	0	0	0	0	0	0	0	0	0	0	0	0	0	0	0	0	0	0	0	0	0	0	0	0	0
L VI L	0	0	0	0	0	0	0	0	0	0	0	0	0	0	0	0	0	0	0	0	0	0	0	0	0	0	0	0	0	0	0	0	0	0
C I L	0	0	0	0	0	0	0	0	0	0	0	0	0	0	0	0	0	0	0	0	0	0	0	0	0	0	0	0	0	0	0	0	0	0
C II L	0	0	0	0	0	0	0	0	0	0	0	0	0	0	0	0	0	0	0	0	0	0	0	0	0	0	0	0	0	0	0	0	0	0
L VIIb L	0	0	0	0	0	0	0	0	0	0	0	0	0	0	0	0	0	0	0	0	0	0	0	0	0	0	0	0	0	0	0	0	0	0
L VIIIa L	0	0	0	0	0	0	0	0	0	0	0	0	0	0	0	0	0	0	0	0	0	0	0	0	0	0	0	0	0	0	0	0	0	0
L VIIIb L	0	0	0	0	0	0	0	0	0	0	0	0	0	0	0	0	0	0	0	0	0	0	0	0	0	0	0	0	0	0	0	0	0	0
L IX L	0	0	0	0	0	0	0	0	0	0	0	0	0	0	0	0	0	0	0	0	0	0	0	0	0	0	0	0	0	0	0	0	0	0
L X L	0	0	0	0	0	0	0	0	0	0	0	0	0	0	0	0	0	0	0	0	0	0	0	0	0	0	0	0	0	0	0	0	0	0
DN L	0	0	0	0	0	0	0	0	0	0	0	0	0	0	0	0	0	1	0	0	1	1	1	1	1	1	0	1	1	0	0	0	0	0
IN L	0	0	0	0	0	0	0	0	0	0	0	0	0	0	0	0	0	1	0	0	1	1	1	1	1	1	0	1	1	0	0	0	0	0
FN L	0	0	0	0	1	1	1	0	0	0	0	0	1	0	0	0	0	1	0	0	1	1	1	1	1	1	0	1	0	1	0	0	0	0
V VI	0	0	0	0	0	0	0	0	0	0	0	0	0	0	0	0	0	0	0	0	0	0	0	0	0	0	0	0	0	0	0	0	0	0
V VII	0	0	0	0	0	0	0	0	0	0	0	0	0	0	0	0	0	0	0	0	0	0	0	0	0	0	0	0	0	0	0	0	0	0
V VIII	0	0	0	0	0	0	0	0	0	0	0	0	0	0	0	0	0	0	0	0	0	0	0	0	0	0	0	0	0	0	0	0	0	0
V IX	0	0	0	0	0	0	0	0	0	0	0	0	0	0	0	0	0	0	0	0	0	0	0	0	0	0	0	0	0	0	0	0	0	0
V X	0	0	0	0	0	0	0	0	0	0	0	0	0	0	0	0	0	0	0	0	0	0	0	0	0	0	0	0	0	0	0	0	0	0
DN R	1	0	0	1	1	1	1	1	1	0	1	1	0	0	0	0	0	0	0	0	0	0	0	0	0	0	0	0	0	0	0	0	0	0
IN R	1	0	0	1	1	1	1	1	1	0	1	1	0	0	0	0	0	0	0	0	0	0	0	0	0	0	0	0	0	0	0	0	0	0
FN R	1	0	0	1	1	1	1	1	1	0	1	0	1	0	0	0	0	0	0	0	0	1	1	1	0	0	0	0	0	1	0	0	0	0
L I-IV R	0	0	0	0	0	0	0	0	0	0	0	0	0	0	0	0	0	0	0	0	0	0	0	0	0	0	0	0	0	0	0	0	0	0
L V R	0	0	0	0	0	0	0	0	0	0	0	0	0	0	0	0	0	0	0	0	0	0	0	0	0	0	0	0	0	0	0	0	0	0
L VI R	0	0	0	0	0	0	0	0	0	0	0	0	0	0	0	0	0	0	0	0	0	0	0	0	0	0	0	0	0	0	0	0	0	0
C I R	0	0	0	0	0	0	0	0	0	0	0	0	0	0	0	0	0	0	0	0	0	0	0	0	0	0	0	0	0	0	0	0	0	0
C II R	0	0	0	0	0	0	0	0	0	0	0	0	0	0	0	0	0	0	0	0	0	0	0	0	0	0	0	0	0	0	0	0	0	0
L VIIb R	0	0	0	0	0	0	0	0	0	0	0	0	0	0	0	0	0	0	0	0	0	0	0	0	0	0	0	0	0	0	0	0	0	0
L VIIIa R	0	0	0	0	0	0	0	0	0	0	0	0	0	0	0	0	0	0	0	0	0	0	0	0	0	0	0	0	0	0	0	0	0	0
L VIIIb R	0	0	0	0	0	0	0	0	0	0	0	0	0	0	0	0	0	0	0	0	0	0	0	0	0	0	0	0	0	0	0	0	0	0
L IX R	0	0	0	0	0	0	0	0	0	0	0	0	0	0	0	0	0	0	0	0	0	0	0	0	0	0	0	0	0	0	0	0	0	0
L X R	0	0	0	0	0	0	0	0	0	0	0	0	0	0	0	0	0	0	0	0	0	0	0	0	0	0	0	0	0	0	0	0	0	0

Table 12. Binary structural connectivity matrix depicting direct monosynaptic projections from cerebellar lobules and deep cerebellar nuclei to targets within the thalamus and hypothalamus.

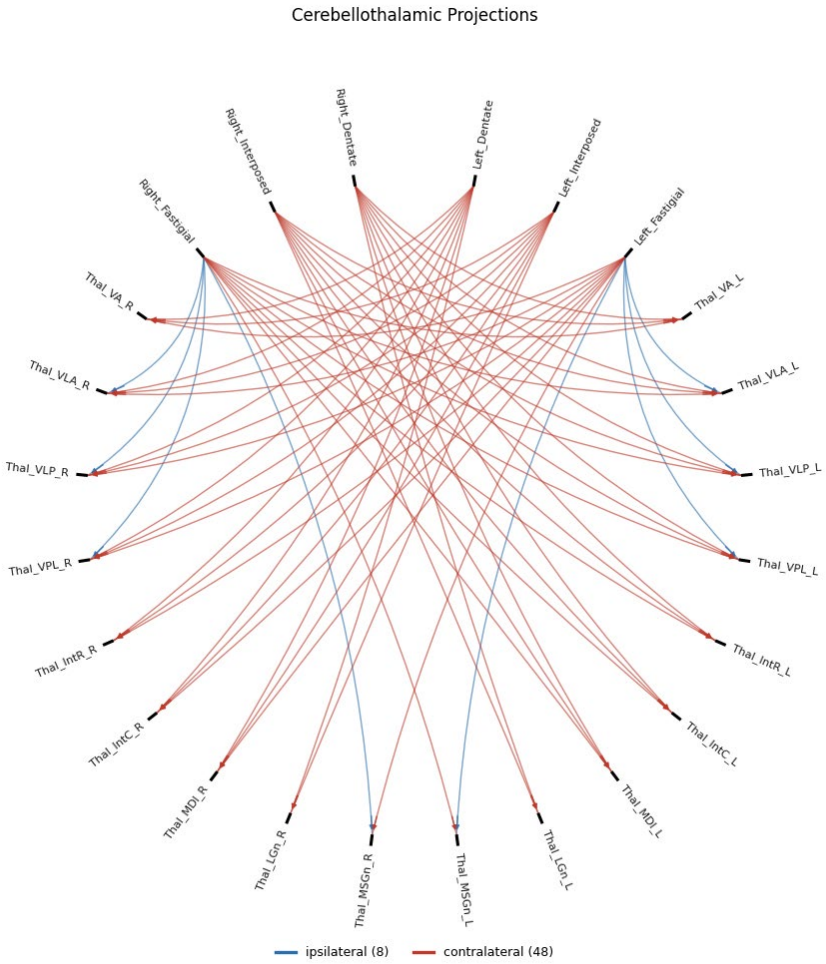


Figure 3. Connectome depicting direct monosynaptic projections from the cerebellar deep nuclei to the thalamus.

3.2 Graph Theory

The literature-derived structural connectivity matrix comprised 139 nodes and 1,876 directed connections, corresponding to a directed network density of 0.098 (1,876 of 19,182 possible directed connections). Of these connections, 699 involved at least one cerebellar region. Of these, 46 were intracerebellar, 425 were afferent to the cerebellum and 228 were efferent from it. The global reciprocity, defined as the proportion of connections present in both directions, was 0.383.

Node-level measures were computed for the 31 cerebellar regions (25 cortical regions and 6 DCN). Measures are reported for the 31 cerebellar regions but were calculated using each region's connections with all 139 regions of the network, including non-cerebellar regions. Degree measures are reported in Table 6, and the remaining topological measures (local reciprocity, betweenness centrality, clustering coefficient and trophic level) are in Table 14.

Degree

Degree values are reported for each region separately, for example, the left and right DN are counted as two regions, because laterality rules were applied equally to both hemispheres, homologous left and right regions had identical values. In the cerebellar cortex, out-degree was 2 in most hemispheric lobules, 3 in lobule IX and 5 in lobule X. In the vermis, out-degree ranged from 2 in vermis VII to 7 in vermis VI and VIII and 9 in vermis IX and X. In-degree ranged from 7 to 15 in the hemispheric lobules and from 14 to 21 in the vermis. In the DCN, in-degree ranged from 30 to 33 and out-degree from 30 to 36. Total degree was therefore highest in the FN (66), followed by the DN (63) and IN (62), and lowest in hemispheric lobules V, VI, VIIIa and VIIIb (9) (Table 13).

Region	In-degree	Out-degree	Total degree
Left hemisphere			
Lobules I–IV (L)	9	2	11
Lobule V (L)	7	2	9
Lobule VI (L)	7	2	9
Crus I (L)	13	2	15
Crus II (L)	12	2	14
Lobule VIIb (L)	9	2	11
Lobule VIIIa (L)	7	2	9
Lobule VIIIb (L)	7	2	9
Lobule IX (L)	12	3	15
Lobule X (L)	15	5	20
Right hemisphere			
Lobules I–IV (R)	9	2	11
Lobule V (R)	7	2	9
Lobule VI (R)	7	2	9
Crus I (R)	13	2	15
Crus II (R)	12	2	14
Lobule VIIb (R)	9	2	11
Lobule VIIIa (R)	7	2	9
Lobule VIIIb (R)	7	2	9
Lobule IX (R)	12	3	15
Lobule X (R)	15	5	20

Vermis			
Vermis VI	14	7	21
Vermis VII	16	2	18
Vermis VIII	17	7	24
Vermis IX	21	9	30
Vermis X	17	9	26
Deep cerebellar nuclei			
DN (L)	33	30	63
DN (R)	33	30	63
IN (L)	32	30	62
IN (R)	32	30	62
FN (L)	30	36	66
FN (R)	30	36	66

Table 13. Degree measures of the cerebellar regions within the literature-derived binary structural connectivity matrix.

Topological Measures

Betweenness centrality ranged from 0.026 to 0.042 in the DCN, with the highest values in the DN (0.042). In the cerebellar cortex, betweenness was 0.003 or lower and was zero in 12 lobules. The clustering coefficient was higher in the cerebellar cortex (0.311–0.500) than in the DCN (0.231–0.250). Local reciprocity ranged from 0.260 to 0.348 in the DCN, with the highest value in the IN, and from 0 to 0.250 in the cerebellar cortex, where it was zero in 14 regions (Table 14). Trophic level was lower in the DCN (1.253–1.346) than in the cerebellar cortex (1.353–1.859). Across the whole network, the mean trophic level was lowest in the cerebral cortex (0.47), intermediate in subcortical and brainstem regions (1.23–1.25), the DCN (1.31) and the cerebellar cortex (1.69), and highest in the thalamus (1.96). The trophic incoherence of the network was F0 = 0.70.

Region	Local reciprocity	Betweenness centrality	Clustering coefficient	Trophic level
Left hemisphere				
Lobules I–IV (L)	0.000	0.0000	0.400	1.675
Lobule V (L)	0.000	0.0000	0.444	1.686
Lobule VI (L)	0.000	0.0000	0.444	1.686
Crus I (L)	0.071	0.0002	0.385	1.762
Crus II (L)	0.077	0.0002	0.311	1.740
Lobule VIIb (L)	0.000	0.0000	0.455	1.737
Lobule VIIIa (L)	0.000	0.0000	0.444	1.686
Lobule VIIIb (L)	0.000	0.0000	0.444	1.686
Lobule IX (L)	0.071	0.0002	0.466	1.724
Lobule X (L)	0.250	0.0014	0.320	1.790
Right hemisphere				
Lobules I–IV (R)	0.000	0.0000	0.400	1.686
Lobule V (R)	0.000	0.0000	0.444	1.700
Lobule VI (R)	0.000	0.0000	0.444	1.700
Crus I (R)	0.071	0.0002	0.380	1.766
Crus II (R)	0.077	0.0002	0.311	1.749
Lobule VIIb (R)	0.000	0.0000	0.455	1.748
Lobule VIIIa (R)	0.000	0.0000	0.444	1.700
Lobule VIIIb (R)	0.000	0.0000	0.444	1.700
Lobule IX (R)	0.071	0.0002	0.471	1.732
Lobule X (R)	0.250	0.0014	0.323	1.796
Vermis				
Vermis VI	0.000	0.0027	0.443	1.500
Vermis VII	0.000	0.0005	0.333	1.859
Vermis VIII	0.200	0.0031	0.344	1.558
Vermis IX	0.154	0.0017	0.430	1.481
Vermis X	0.182	0.0009	0.500	1.353
Deep cerebellar nuclei				
DN (L)	0.260	0.0422	0.238	1.346
DN (R)	0.260	0.0424	0.231	1.345
IN (L)	0.348	0.0347	0.250	1.314
IN (R)	0.348	0.0353	0.240	1.312
FN (L)	0.294	0.0263	0.240	1.253
FN (R)	0.294	0.0258	0.245	1.257

Table 14. Topological measures of cerebellar regions within the literature-derived structural connectivity matrix.

3.3 Tractography Reconstruction

Seven tractography configurations were compared against the literature-based structural connectivity matrix (Section 2.3.4). The final parcellation used for tractography contained the 112 regions listed in Table 1 in the subject diffusion space. Each pair of regions was therefore counted as connected if the reference documented a projection in either direction. The resulting reference comprised 368 cerebellar connections across 2,976 eligible region pairs: 46 intracerebellar, 22 between the cerebellum and the brainstem, and 98 between the cerebellum and thalamic or other supratentorial regions.

Parcellation

The parcellation used for tractography contained 112 regions (Table 1) and was transformed into the participant's diffusion space (Figure 4). It combined cerebral cortical and subcortical regions, thalamic nuclei, brainstem nuclei and cerebellar lobules and deep nuclei (Table 4). In the cerebral cortex, only the regions included in the matrix (PFC, M1 and PMSMA) were used. The 28 pontine regions of the matrix (14 on each side) were merged into a single pons region (Table 3) which reduced the 139 regions of the matrix to 112.

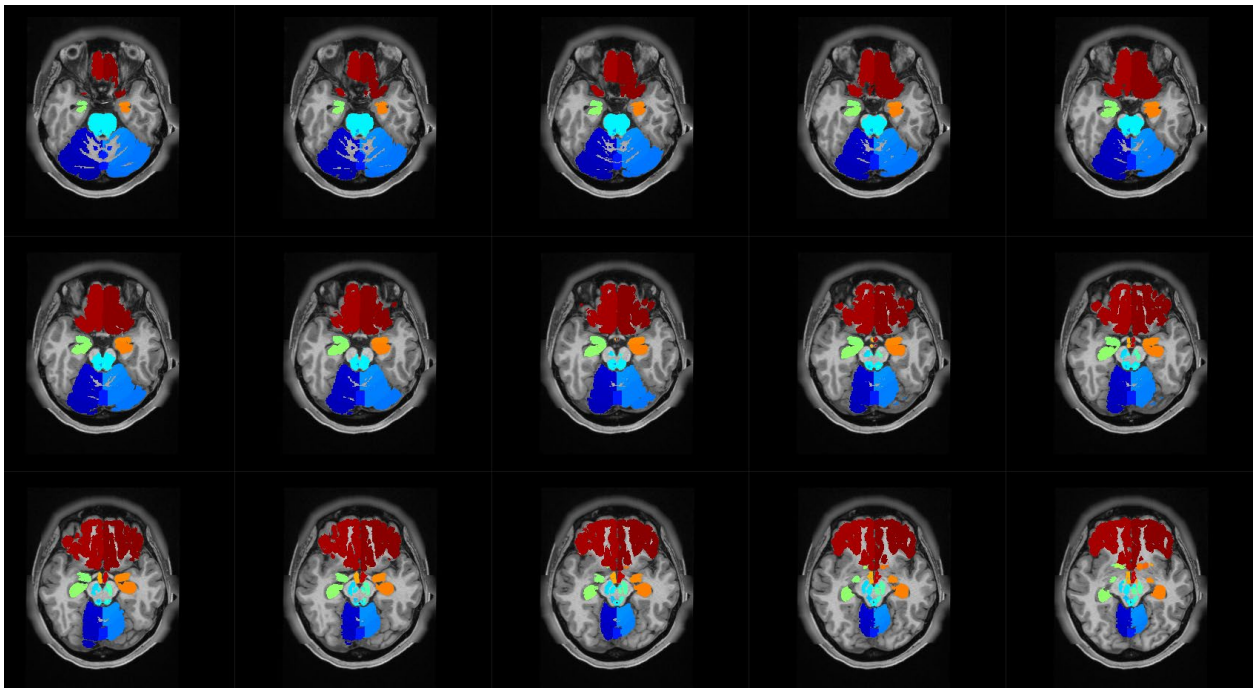


Figure 4. Parcellation of the participant's brain into 112 regions (Table 1), shown on axial T1-weighted

slices from inferior (top left) to superior (bottom right). The left hemisphere is shown on the right side of each image. Only the cortical regions included in the matrix (PFC, M1 and PMSMA) are labeled in the cerebral cortex. The pontine nuclei are shown as a single pons region. Shown at 0.8mm resolution.

Reference connections used for the comparison

Because tractography cannot determine the direction of a connection, the directed matrix was converted into undirected connections: each pair of regions was counted as connected if the reference documented a projection in either direction. Two analyses were performed (Table 15). The cerebellar analysis included the 2,976 region pairs with at least one cerebellar region. In this analysis, 429 directed cerebellar connections became 368 undirected connections: 46 intracerebellar, 224 between the cerebellum and the brainstem, and 98 between the cerebellum and supratentorial region. The whole-matrix analysis included all 4,563 region pairs. In this analysis, the 1,119 directed connections became 883 undirected connections.

Analysis	Region pairs	One-way pairs	Reciprocal pairs	Undirected connections	Directed connections
Cerebellar analysis	2,976	307 (× 1 = 307)	61 (× 2 = 122)	368	429
Whole-matrix analysis	4,563	647 (× 1 = 647)	236 (× 2 = 472)	883	1,119

Table 15. Conversion of the 112-region directed reference matrix into undirected connections for comparison with tractography. A one-way pair contains one directed connection and a reciprocal pair two. By merging the two directions of each reciprocal pair gives the number of undirected connections.

Cerebellar analysis

In the cerebellar analysis, every configuration reconstructed more false-positive than true-positive connections (Table 16). Sensitivity ranged from 0.380 (Deterministic) to 0.541 (GM-WM default), and precision did not exceed 0.270 (Deterministic). GM-WM default recovered the most reference connections (199 TP) but also produced 657 FP, and 169 reference connections were not recovered (FNe). Deterministic produced the fewest FP (379) but recovered only 140 reference connections and missed 228. Traditional ACT had the lowest precision (0.147), with 1,104 FP. GM-WM 0.06 achieved the highest Youden's J (0.292) and F1 score (0.329), followed closely by GM-WM default (J = 0.289) and Dynamic seeding (J = 0.272), whereas No ACT (J = 0.161) and Traditional ACT (J = 0.093) performed worst.

Configuration	Tracts	TP	FP	FNe	TN	Sens.	Prec.	Spec.	F1	Youden's J
GM-WM 0.06	816	195	621	173	1987	0.530	0.239	0.762	0.329	0.292
GM-WM default	856	199	657	169	1951	0.541	0.232	0.748	0.325	0.289
Dynamic seeding	697	174	523	194	2085	0.473	0.250	0.799	0.327	0.272
GM-WM 0.8 mm	735	171	564	197	2044	0.465	0.233	0.784	0.310	0.248
Deterministic	519	140	379	228	2229	0.380	0.270	0.855	0.316	0.235
No ACT	898	163	735	205	1873	0.443	0.182	0.718	0.258	0.161
Traditional ACT	1294	190	1104	178	1504	0.516	0.147	0.577	0.229	0.093

Table 16. Agreement between tractography and the matrix for connections with at least one cerebellar region (2,976 node pairs), for the seven tractography configurations, ordered by Youden's J. Of the 429 (112-node matrix) directed cerebellar connections, 368 undirected connections remained after merging the pontine nuclei and the two directions of the 61 reciprocal pairs.

Performance differed by type of connection. In the five configurations using the modified tissue image, intracerebellar connections were recovered almost completely (43 to 46 of 46; sensitivity 0.935–1.000), but with low precision (0.110–0.144), because tractography also reconstructed connections between cortical lobules, and between lobules and deep nuclei, that are absent from the reference. Connections between the cerebellum and the brainstem showed the most balanced performance (sensitivity 0.402–0.638; precision 0.429–0.545). Connections between the cerebellum and supratentorial regions were the most difficult to reconstruct: these five configurations recovered at most 11 of the 98 reference connections (sensitivity 0.020–0.112), and Dynamic seeding recovered only 2.

Laterality of Reconstructed Connections of the Cerebellum

To evaluate whether tractography reconstructed connections are on the correct side, the reference connections of the cerebellar analysis between two lateralized regions were divided into ipsilateral connections (both regions in the same hemisphere; n = 120) and contralateral connections (regions in opposite hemispheres; n = 144). Connections involving a midline region (vermis, pons, VTA and PAG) were excluded. For each configuration, the proportion of

recovered connections was calculated for each group as the number of recovered connections divided by the total number of connections in that group. All configurations recovered a larger proportion of ipsilateral than contralateral connections, and ipsilateral connections were recovered 2.4 to 3.4 times more often than contralateral ones (Table 17).

Configuration	**Ipsilateral recovered**	**Contralateral recovered**	**Ratio (ipsilateral/contralateral)**
GM-WM 0.06	83/120 (0.69)	41/144 (0.28)	2.4
GM-WM default	85/120 (0.71)	42/144 (0.29)	2.4
Dynamic seeding	77/120 (0.64)	32/144 (0.22)	2.9
GM-WM 0.8 mm	73/120 (0.61)	34/144 (0.24)	2.6
Deterministic	63/120 (0.53)	22/144 (0.15)	3.4
No ACT	64/120 (0.53)	27/144 (0.19)	2.8
Traditional ACT	83/120 (0.69)	31/144 (0.22)	3.2

Table 17. Connections of the literature-based matrix recovered by tractography for the cerebellum.

The matrix contained 56 connections between the DCN and the thalamus, 48 of which were crossed. None of the crossed connections were reconstructed by the five configurations using the modified tissue image, including *GM-WM 0.06* and *Dynamic seeding*, which reconstructed only ipsilateral connections between the deep nuclei and the thalamus, almost all of which were false positives (Table 18). Crossed connections were reconstructed only by *No ACT* (3) and *Traditional ACT* (2).

Configuration	**Reconstructed**	**Crossed, TP**	**Crossed, FP**	**Ipsilateral, TP**	**Ipsilateral, FP**
GM-WM 0.06	27	0	0	1	26
GM-WM default	27	0	0	1	26
Dynamic seeding	2	0	0	0	2
GM-WM 0.8 mm	32	0	0	4	28
Deterministic	23	0	0	0	23
No ACT	34	3	2	1	28
Traditional ACT	21	2	0	0	19

Table 18. Connections between the deep cerebellar nuclei and the thalamus reconstructed by each configuration, by laterality. The reference contained 56 such connections (48 crossed and 8 ipsilateral). TP means a connection is present in the reference, while FP means a connection absent from the reference.

Whole-Matrix Performance

In the whole-matrix analysis (4,563 node pairs; 883 reference connections), the five configurations using the modified tissue image performed best, with Youden's J between 0.273 and 0.321 (Table 14). Dynamic seeding achieved the highest J (0.321; sensitivity 0.559, specificity 0.761), followed by *GM-WM default* (0.307) and *GM-WM 0.06* (0.297). *GM-WM default* recovered the most reference connections (543 TP; sensitivity 0.615) but also produced more false positives than *Dyanmic seeding* (1,134 vs 878), while missing fewer reference connections (340 vs 389 FNe). *Deterministic* tractography was the most conservative, with the highest precision (0.375) and specificity (0.818) but the lowest sensitivity among these five (0.455).No ACT (J = 0.161) and Traditional ACT (J = 0.092) performed worst, and Traditional ACT produced the most false positives (1,330). Across all configurations, precision remained low (0.231–0.375), meaning that most reconstructed connections were not in the reference (Table 19).

Configuration	Reconstructed Connections	TP	FP	FNe	TN	FP (%)
Dynamic seeding	1372	494	878	389	2802	64.0
GM-WM default	1677	543	1134	340	2546	67.6
GM-WM 0.06	1605	522	1083	361	2597	67.5
GM-WM 0.8 mm	1503	499	1004	384	2676	66.8
Deterministic	1073	402	671	481	3009	62.5
No ACT	1252	357	895	526	2785	71.5
Traditional ACT	1730	400	1330	483	2350	76.9

Table 19. Agreement between tractography and the matrix in the whole-matrix analysis.

Configuration	Reconstructed Connections	Sensitivity	Precision	Specificity	F1	Youden's J
Dynamic seeding	1372	0.559	0.360	0.761	0.438	0.321
GM-WM default	1677	0.615	0.324	0.692	0.424	0.307
GM-WM 0.06	1605	0.591	0.325	0.706	0.420	0.297
GM-WM 0.8 mm	1503	0.565	0.332	0.727	0.418	0.292
Deterministic	1073	0.455	0.375	0.818	0.411	0.273
No ACT	1252	0.404	0.285	0.757	0.334	0.161
Traditional ACT	1730	0.453	0.231	0.639	0.306	0.092

Table 20. Performance of the seven configurations in the whole-matrix analysis: sensitivity, precision, specificity, F1 and Youden's J, ordered by J.

Sources of Disagreement between Tractography and the References

Each false-positive and false-negative connection of the cerebellar analysis was classified according to the regions it connected, for the three configurations with the highest Youden's J:

- *GM-WM 0.06* (J = 0.292): 621 false positives and 173 false negatives.
- *GM-WM default* (J = 0.289): 657 false positives and 169 false negatives.
- *Dynamic seeding* (J = 0.272): 523 false positives and 194 false negatives.

The errors were distributed similarly across the three configurations. Most false positives (41 to 49%) connected two neighboring cerebellar cortical lobules, which are not connected in the matix. A further 13 to 16% connected a lobule with a deep nucleus to which it does not project, such as vermal lobule X and the IN. Most false negatives involved either the Hypo, LC, VTA, and PAG (40 to 43%), or the connections between the DCN and the thalamus (29 to 33%), which included all 48 crossed connections.

Table 21 shows the number of streamlines reconstructed by each configuration for examples of reference connections, selected to include connections found by many and by few configurations. The corticonuclear projection from the left Crus II to the left DN was reconstructed by all seven configurations (Figure 5), but the number of streamlines differed widely. *Traditional ACT* reconstructed 1,115 streamlines, *No ACT* 16,518, and the five configurations using the modified tissue image between 10,430 (*GM-WM 0.8 mm*) and 32,031 (*Dynamic seeding*). The projection from the right hypothalamus to the right DN was reconstructed by six configurations, with 12 to 150 streamlines. With *GM-WM 0.06*, its 54 streamlines ran posteriorly from the hypothalamus, descended through the brainstem and

entered the cerebellum to reach the DN. The projection from vermal lobule VII to the left FN was reconstructed by four configurations, with 10 (*GM-WM 0.06*) to 480 streamlines (*No ACT*), and it was the only intracerebellar connection missed by *GM-WM default*. Connections between the DCN and the thalamus were rarely reconstructed: the crossed projection from the left DN to the right VLp was found only by *Traditional ACT* (9 streamlines), and the ipsilateral projection from the right FN to the right VLa only by *GM-WM 0.8 mm* (7 streamlines). Crossed projections of the LC were reconstructed in some cases. The connection between the left LC and the right IN was found only by *Deterministic* (95 streamlines), and the connection between the right LC and the left DN was reconstructed by *GM-WM 0.06* with 55 streamlines that crossed the midline in the dorsal pons before reaching the DN.

Connection	***Trad. ACT***	***No ACT***	***GM-WM default***	***GM-WM 0.06***	***GM-WM 0.8 mm***	***Dyn. seeding***	***Determ.***	**Found by (of 7)**
Left Crus II → left DN (86–92)	1,115	16,518	10,936	10,515	10,430	32,031	13,468	7
Right Hypo → right DN (33–100)	12	150	57	54	13	–	14	6
Vermis VII → left FN (96–94)	–	480	–	10	176	23	–	4
Left Hypo → left IN (7–93)	25	–	12	–	–	–	–	2
Left Ve – vermis IX (67–98)	–	–	–	–	–	10	7	2
Left DN → right VLp (92–38)	9	–	–	–	–	–	–	1
Right FN → right VLa (102–37)	–	–	–	–	7	–	–	1
Left LC → right IN (65–101)	–	–	–	–	–	–	95	1

Table 21. Number of streamlines reconstructed by each configuration for examples of reference connections in participant HCA6053758. Arrows give the direction of the projection in the matrix. A dash means the connection was not reconstructed. Region numbers refer to Table 1.

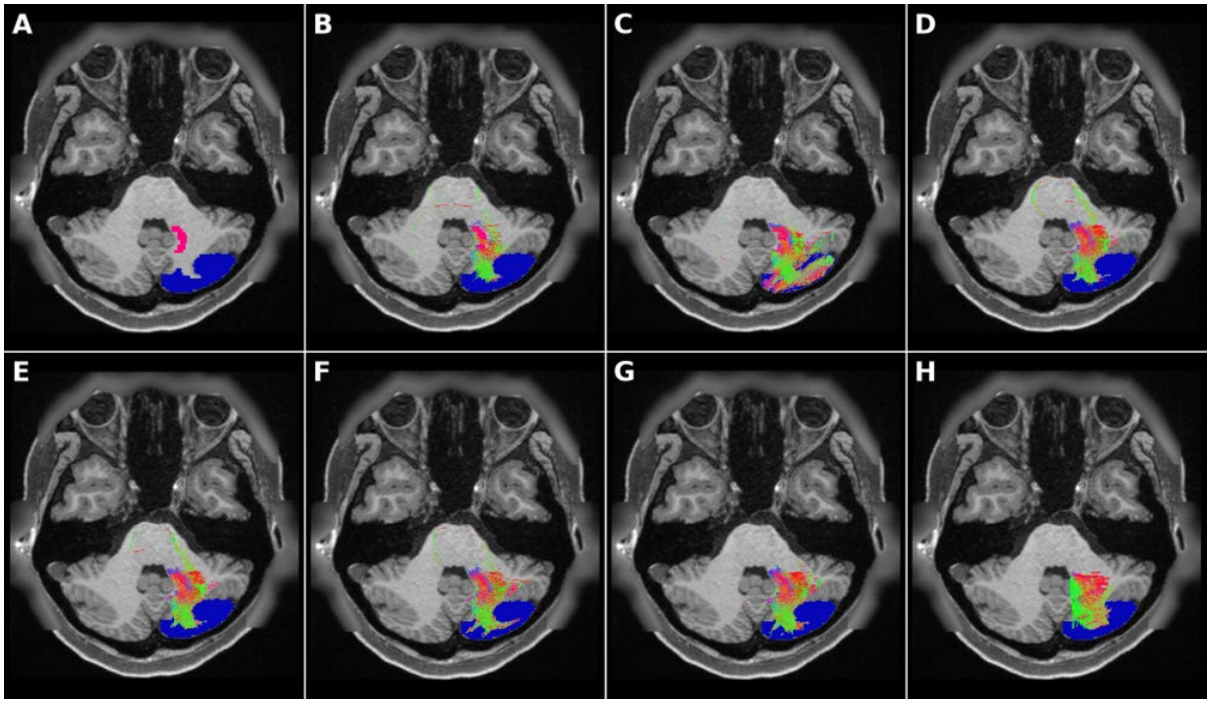


Figure 5. Streamlines connecting the left Crus II and the left dentate nucleus (DN) in participant HCA6053758, reconstructed by each of the seven tractography configurations and shown on the same T1-weighted slice: (B) *Traditional ACT* (1,115 streamlines), (C) *No ACT* (16,518), (D) *GM-WM default* (10,936), (E) *GM-WM 0.06* (10,515), (F) *GM-WM 0.8 mm* (10,430), (G) *Dynamic seeding* (32,031) and (H) *Deterministic* (13,468). (A) Location of left Crus II (blue) and the left DN (pink).

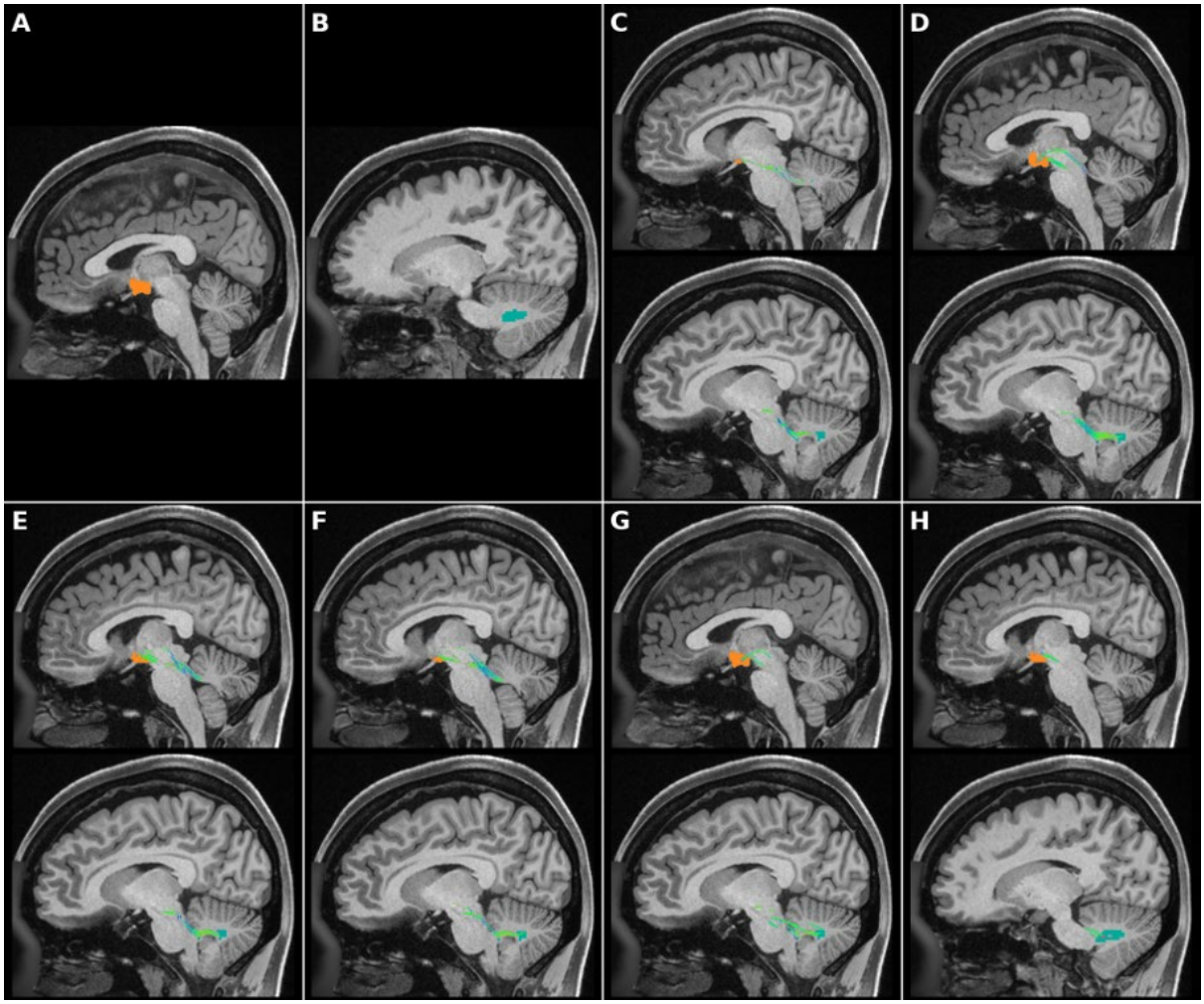


Figure 6. Streamlines connecting the right hypothalamus and the right dentate nucleus (DN) in participant HCA6053758, shown on sagittal T1-weighted slices. Location of the right hypothalamus (orange). (B) Location of the right DN (teal). (C) *Traditional ACT* (12 streamlines), (D) *No ACT* (150), (E) *GM-WM default* (57), (F) *GM-WM 0.06* (54), (G) *GM-WM 0.8 mm* (13) and (H) *Deterministic* (14). *Dynamic seeding* did not reconstruct this connection. In panels C–H, the top image shows the hypothalamus, and the bottom image shows the DN, with streamlines drawn thicker in the bottom images for visibility. Two slices are shown for each configuration because the hypothalamus lies near the midline and the DN lies more laterally, so both cannot be seen on the same sagittal slice.

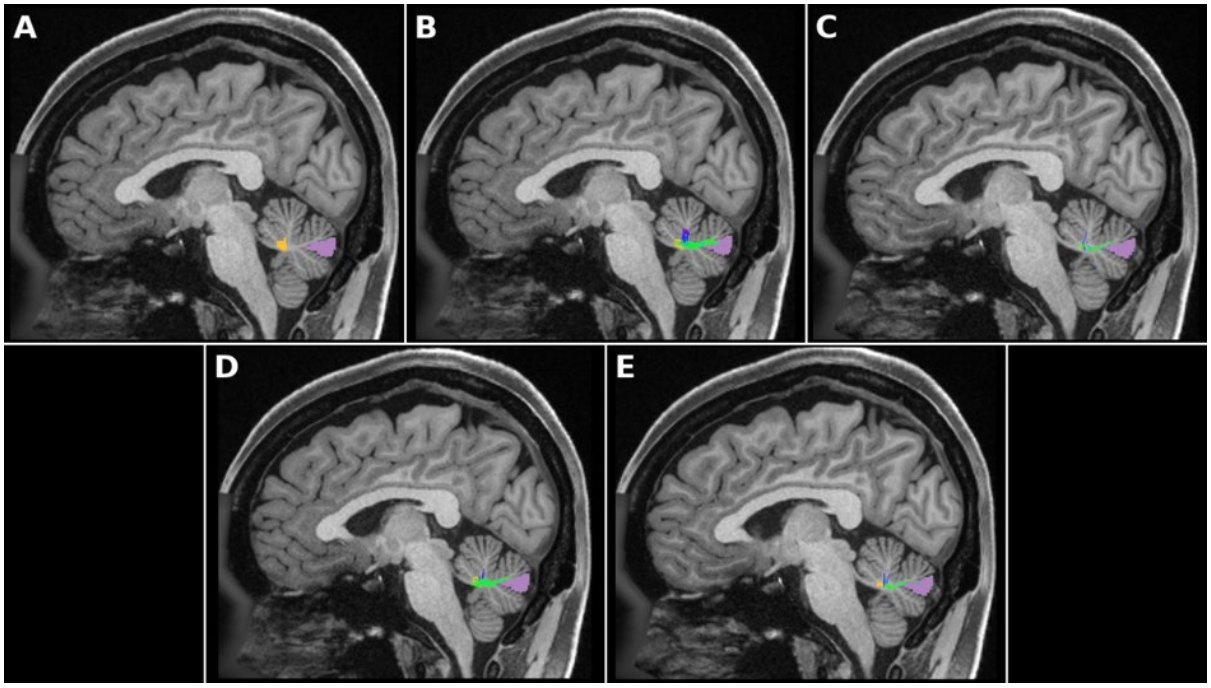


Figure 7. Streamlines connecting vermal lobule VII and the left fastigial nucleus (FN) in participant HCA6053758, shown on sagittal T1-weighted slices. (A) Location of vermal lobule VII (purple) and the left FN (orange). (B) *No ACT* (480 streamlines), (C) *GM-WM 0.06* (10), (D) *GM-WM 0.8 mm* (176) and (E) *Dynamic seeding* (23). *Traditional ACT*, *GM-WM default* and *Deterministic* did not reconstruct this connection.

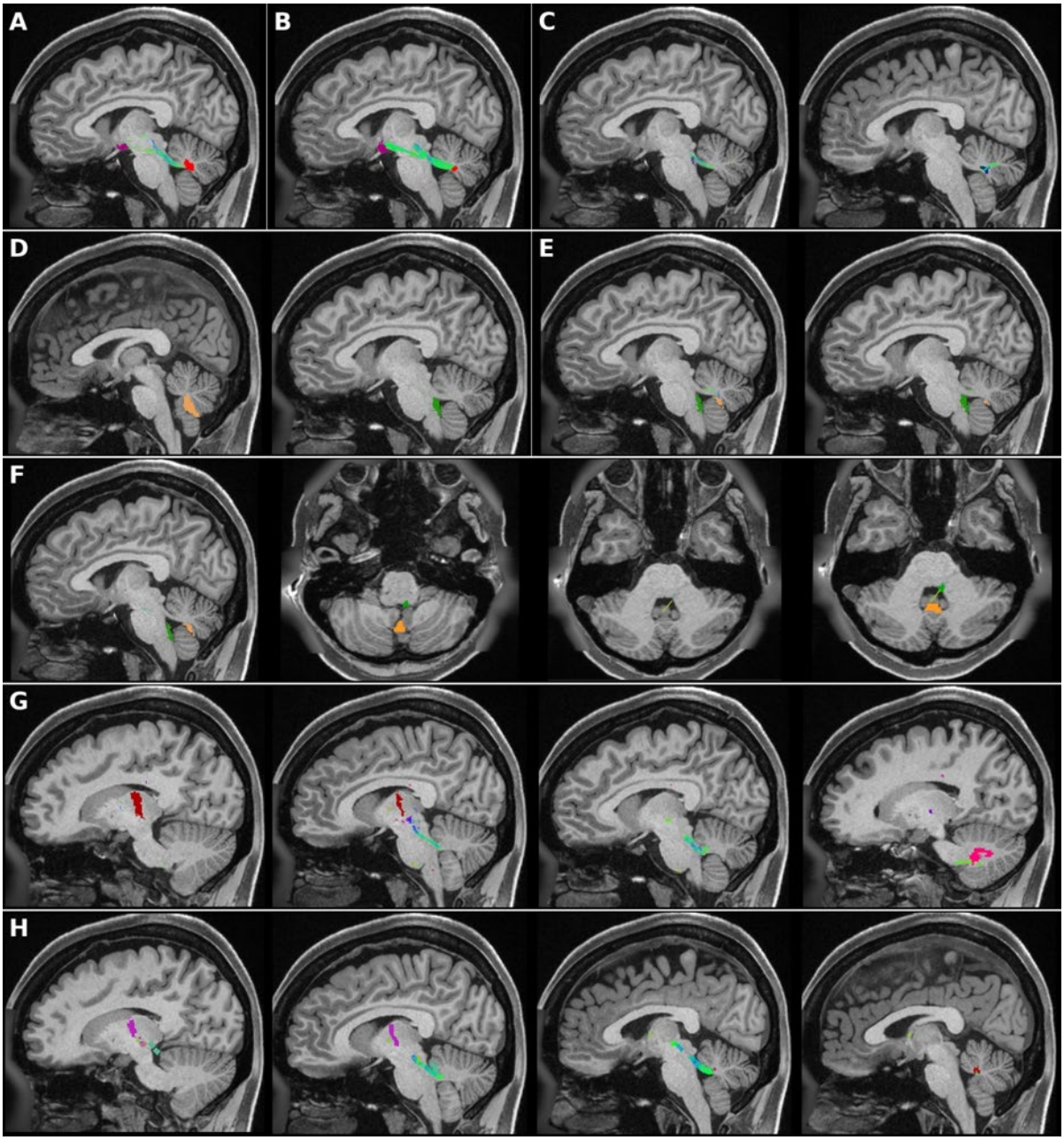


Figure 8. Reference connections reconstructed by only one or two tractography configurations in participant HCA6053758, shown on sagittal T1-weighted slices except for panel F showing the axial T1-weighted slices. (A, B) Left hypothalamus (purple) to left IN (red), reconstructed by *Traditional ACT (*25 streamlines) and *GM-WM default* (12). (C) Left LC (purple) to right IN (blue), reconstructed only by *deterministic* tracking (95). (D) Left Ve (dark green) to vermis IX (orange), reconstructed by *dynamic seeding* (E) (10) and *deterministic* tracking (F) (7). (G) Left DN (pink) to right VLp (brown), reconstructed only by Traditional ACT (9); slices progress from the thalamus through the brainstem crossing to the DN. (H) Right FN (brown) to right VLa (purple), reconstructed only by *GM-WM 0.8 mm* (7). For crossed and multi-slice connections, successive slices are shown from left to right. Streamlines are drawn thicker in B and H for visibility.

4. Discussion

The main aim of this thesis was to build a binary, directed structural connectivity matrix of the human cerebellum and its connections with the brainstem, thalamus and other subcortical regions, based on anatomical literature, and encoding the directionality and laterality of each connection. This cerebellar matrix was subsequently merged with a matrix that included the connections of the brainstem nuclei with three cerebral cortical regions (prefrontal cortex, primary motor cortex, and premotor and supplementary motor area), the thalamus, the hypothalamus, and other subcortical regions. The whole-brain directed structural connectivity matrix had 139 regions. The organization of the matrix was then characterized with graph-theoretical measures, and the matrix was used as a reference to evaluate how accurately seven different diffusion MRI tractography configurations reconstruct cerebellar connections.

There were three main findings. First, the graph-theoretical measures of the matrix reproduced the known architecture of the cerebellum, with the cerebellar cortex mainly receiving connections and the DCN acting as the main output stations. Second, the best agreement with the literature-derived matrix was achieved by three tractography configurations using a modified anatomical constrain tractography (ACT) segmentation, in which the DCN, brainstem nucleus, hypothalamus, septal nucleus, subthalamic nucleus, and claustrum were classified as deep gray matter to allow streamlines to terminate in these regions. This was the methodological choice with the largest effect on Youden's J index. Among these tractographies, *GM-WM default* identified the largest number of cerebellar connections that were also present in the binary connectivity matrix (199 of 368; sensitivity 0.541) and also had the highest sensitivity in the whole-brain matrix analysis (543 of 883; 0.615). However, it also reconstructed more false positives, so when both recovered and absent connections were considered with Youden's J index, *GM-WM 0.06* performed best in the cerebellar analysis and *Dynamic seeding* in the whole-brain matrix analysis (Tables 18 and 22). Nevertheless, all configurations produced a large number of false positives between 73 and 85% of the connections reconstructed by each configuration in the cerebellar analysis were not in the binary matrix (Table 18). This reflects the nature of tractography, which infers connections only from the local orientation of fibers in each voxel. As a result, streamlines can pass between adjacent or crossing bundles and connect regions that are not anatomically connected, a limitation that persists even under ideal conditions (Maier-Hein et al., 2017). Third, tractography recovered a larger proportion of ipsilateral than contralateral reference connections (53–71% vs 15–29%; Table 17). *GM-WM 0.06* and *Dynamic seeding* did not

reconstruct any of the crossed connections between the DCN and the thalamus, but reconstructed the ipsilateral DCN-thalamus connections, which are false positives (Table 18).

Encoding laterality was important because the major pathways connecting the cerebellum and the cerebral cortex cross the midline, resulting in predominantly contralateral connections between each cerebral hemisphere and the cerebellar hemisphere. This crossed organization is clinically relevant. For example, the dentato-rubro-thalamic tract, which carries cerebellar output to the contralateral thalamus, is used as a target for deep brain stimulation in tremor, and tremor reduction is related to how close the electrode is to the tract (Coenen et al., 2020). Because the target is planned from tractography, a tract reconstructed on the wrong side, or replaced by ipsilateral false-positive streamlines, could lead to a misplaced target, so the side of a reconstructed pathway must be checked against anatomy. Advanced diffusion MRI tractography has already reconstructed the crossed cerebello-thalamo-cortical and cortico-ponto-cerebellar pathways in humans in vivo (Palesi et al., 2015, 2017), showing that tractography can represent laterality. However, tractography also produces many false positives, highlighting the need for an independent anatomical reference to assess the reliability of reconstructed pathways. The matrix built in this thesis provides such reference and adds a second feature that most references used to evaluate tractography do not contain, the direction of each connection. Direction matters because cerebellar circuits have an organized flow of information, from mossy and climbing fibers, which provide the major inputs to the cerebellar cortex, to Purkinje cells, which project to the DCN, and from the DCN to targets in the brainstem and thalamus (Apps & Garwicz, 2005; Voogd & Glickstein, 1998). Although tractography cannot determine direction, the direction encoded in the matrix makes it possible to interpret each reconstructed connection as a cerebellar input or output. Consistent with this organization, the matrix showed inputs targeting the cerebellar cortex, and outputs leaving the cerebellum through the six DCN (Apps & Garwicz, 2005).

The graph-theoretical measures provided complementary evidence that the matrix reflected major features of cerebellar organization, however they cannot by themselves establish that every included connection is correct or that every absent connection is anatomically absent. The in-degree and out-degree indices showed that the cerebellar cortex received more connections than it sent, whereas the DCN both received many connections (in-degree range: 30–33) and sent many (out-degree range: 30–36). Total degree, i.e., the number of connections a region has in both directions, summarizes how connected a region is: the DCN had the highest total degree of all cerebellar regions (range: 62–66), three to seven times that of the hemispheric

lobules (range: 9–20) (Table 13). This confirms that the DCN are the main connection points of the cerebellum, the regions through which most of its connections pass, which is consistent with the corticonuclear organization of the cerebellum: Purkinje cells provide the output of the cerebellar cortex and project mainly to the DCN and Ve, and neurons in these nuclei integrate this input and project to numerous targets in the thalamus and brainstem (Apps & Garwicz, 2005; Voogd & Glickstein, 1998). Because many connections pass through the DCN, whether they were labeled as deep gray matter or white matter in the tissue image used by ACT affected a large number of connections at once. This is one likely reason why changing from the standard tissue-segmentation image used by *Traditional ACT* to the modified one, in which the DCN, brainstem nuclei, hypothalamus, septal nuclei, subthalamic nucleus and claustrum were labeled as gray matter, had a larger effect on tractography than any other methodological choice tested. Within the cerebellar cortex, lobule X and vermal lobules VI, VIII, IX and X sent more connections than the other cortical regions (out-degree from 5 to 9, compared with 2 or 3; Table 13). Most hemispheric lobules project only to the DCN on their own side. In contrast, each vermal lobule, represented as a single midline region, projects to the FN on both sides, and these regions also project directly to brainstem nuclei, mainly the Ve, as is characteristic of the vestibulocerebellum and the vermis (Cullen, 2023).

This distinction was also reflected in the other graph-theoretical measures (Table 14). The high betweenness centrality of the DCN indicates that they occupy an intermediate position between the cerebellar cortex and the extracerebellar regions. Local reciprocity was higher in the DCN than in the cerebellar cortex, because the DCN are reciprocally connected with several brainstem nuclei, such as the inferior olive through the nucleo-olivary loop, the pontine nuclei and the Pb, while most cortical lobules only receive connections from the regions that project to them. The clustering coefficient was higher in the cerebellar cortex because the neighbors of a lobule are mostly brainstem nuclei that are connected with each other and with the DCN that receives the lobule's output. Trophic level reflects the position of a region in the network based on the direction of its connections. In our matrix, the cerebellar cortex had a higher trophic level than the DCN: the cerebellar cortex receives connections from several brainstem nuclei but sends connections mainly to the DCN. The DCN receives input from the several brainstem nuclei, but also project back to many of them and to the thalamus, resulting in lower trophic level. Together with their high degree and betweenness centrality, these finding support the interpretation of the DCN as an integrative output structure, as they integrate inputs from the cerebellar cortex and the brainstem and distribute the outputs to many targets. Anatomical and

physiological studies have shown that cerebellar neurons receive input from multiple, spatially distributed cortical zones of cerebellar cortex, supporting their role for integrating information across different parts of the cerebellar cortex (Apps et al., 2018; Apps & Garwicz, 2005).

At the network level, the trophic levels showed that the matrix was only moderately hierarchical (F0 = 0.70, on a scale from 0, a strictly one-directional hierarchy, to 1, no hierarchy) (MacKay et al., 2020). This partly reflects the corticonuclear projection itself, because the DCN are reciprocally connected with brainstem nuclei at low trophic levels, they were placed below the cerebellar cortex. Consequently, projections from the cerebellar cortex to the DCN run in the opposite direction to the overall trophic hierarchy, linking regions with higher trophic levels to regions with lower trophic levels. Recurrent and reciprocal pathways, such as the nucleo-olivary loop and the reciprocal connections between the FN and Ve also prevent this organization from forming a simple feedforward chain. This is consistent with current accounts of the cerebellum as a set of interconnected, partially segregated loops rather than a single linear pathway (Apps et al., 2018; Kelly & Strick, 2003). However, because thalamocortical projections were not included in our matrix, the large cerebro-cerebellar loops are only partially represented (Kelly & Strick, 2003).

The tractography configurations differed mainly in how many false positives they produced rather than in how many reference connections they recovered. In the cerebellar analysis, the number of true positives varied between 140 and 199, whereas the number of false positives varied between 379 and 1104 (Table 18). Thus, the differences in performance were driven mainly by specificity. The largest difference was observed between *Traditional ACT* and *GM-WM default*, which differed only in the tissue segmentation image. In the standard image used by *Traditional ACT*, the DCN, brainstem nuclei and other subcortical regions were not included in the deep gray matter mask and therefore classified as white matter. Because ACT allows streamlines to terminate only within the gray matter masks, streamlines could not stop in these nuclei and continued until they reached another gray-matter region, potentially creating spurious connections. In comparison, changing the FOD cutoff or the resolution had much smaller effects on the agreement between the binary matrix and tractography configurations in the cerebellar analysis (differences in Youden's J of 0.003 and 0.04, compared with 0.20 for the tissue image). In the whole-matrix analysis, *Dynamic seeding* had the highest Youden's J index (Table 20). For the connections that did not involve the cerebellum, it recovered a similar number of reference connections as *GM-WM 0.06* and *GM-WM default* (320 vs 327 and 344) but produced fewer false positives (355 vs 462 and 477). According to the study done by

Schilling et al. 2019, when tractography was compared with tracer injections in non-human primates, no method achieved both high sensitivity and high specificity, confirming that the large number of false positives is a general limitation of tractography rather than of this specific pipeline.

The best configurations recovered almost all intracerebellar connections, and the streamline counts in Table 21 illustrate how the tissue segmentation image affected their reconstruction. The projection from the left Crus II to the left DN was reconstructed by every configuration, but *Traditional ACT* produced 9 to 29 times fewer streamlines (1115) than the configurations using the modified tissue image (10430 to 32031). Compared with *GM-WM default* (10936 streamlines), which differed only in the tissue image, *Traditional ACT* produced about 10 times fewer streamlines, a difference that reflects whether the DN was classified as gray matter or as white matter in the tissue image. The projection from vermal lobule VII to the left FN was reconstructed with 480 streamlines by *No ACT*, but with only 10 by *GM-WM 0.06*, and it was not reconstructed by *GM-WM defaul*t. In these two configurations, the connection was therefore close to the five-streamline threshold, where small differences in seeding or cutoff decide whether a connection is counted. Streamline counts also vary widely between configurations. They depend on the tracking parameters and therefore should not be interpreted as a measure of connection strength (Jones et al., 2013; Yeh et al., 2021). Although intracerebellar connections were recovered almost completely, they also produced the largest group of false positives: 41-51% of all false positives connected two cerebellar cortical regions (Section 3.3.1). These false positives likely reflect the close spacing of the folia, where a single voxel can contain fibers from neighboring lobules (Maier-Hein et al., 2017).

In all configurations, tractography recovered 53-71% of the ipsilateral reference connections but only 15-29% of the contralateral ones, although the matrix contained more contralateral connections (Table 17). The crossed connections between the DCN and the thalamus were not reconstructed by the tractography configurations using the modified tissue image, while almost all of the ipsilateral connections reconstructed were false positives (Table 18). It is to note, indeed, that cerebellar pathways decussate in small regions of the brainstem, where dentatothalamic fibers cross in the midbrain, and the pons, where pontocerebellar fibers cross into the contralateral middle cerebellar peduncle. In these regions, fibers from both sides cross at sharp angles, and a streamline may follow the dominant fiber orientation and stay on the same side rather than follow the crossing, which could explain why crossed pathways were either reconstructed as ipsilateral or not reconstructed.

The matrix derived from the literature review has some limitations. First, it was restricted to the connections identified in the literature review and therefore reflects the studies available evidence and the animal models in which the studies were performed. Most of the evidence comes from rodents, cats, and non-human primates; consequently, connections that differ across species may be misrepresented. However, the basic cellular organization and microcircuitry of the cerebellum are largely conserved across species, although the size of its subdivisions varies (Sultan & Glickstein, 2007). Second, the matrix does not encode the strength of the projections. Therefore, connections mentioned as sparse or weak in the literature are still coded as 1 in the matrix, which is particularly relevant when interpreting tractography results, as weak projections may be more difficult to reconstruct.

In future work, the reference matrix could be improved by building a separate matrix for each species. This would help distinguish connections that are conserved across species from those supported from only one single species. Recording the type and number of studies supporting each connection would also show how strong the evidence is for each entry and would make it easier to identify and correct entries supported by weak or indirect evidence.

Tractography should be evaluated in more HCP-A participants to test whether the relative performance of the configurations is the same across individuals. In addition, methods that filter the streamlines according to how well they explain the diffusion signal, such as spherical-deconvolution informed filtering of tractograms (SIFT2; Smith et al., 2015) or convex optimization modeling for microstructure informed tractography (COMMIT; Daducci et al., 2015), could help to reduce the contribution of spurious streamlines.

In summary, this thesis built a literature-derived matrix of cerebellar connectivity that encodes the directionality and laterality of each connection. By encoding direction, the matrix reproduced the known organization of the cerebellum, with the cerebellar cortex mainly receiving connections and the DCN acting as its output stations. Used as a reference, it showed that tractography recovered only about half of the cerebellar connections, while most of the connections it reconstructed were false positives. Among the tested configurations, using a tissue segmentation image in which the DCN, brainstem nuclei, hypothalamus, septal nuclei, subthalamic nucleus and claustrum were labeled as deep gray matter had the largest effect on performance, mainly by reducing false positives. By encoding laterality, the matrix also showed that crossed connections were more difficult for tractography to reconstruct than ipsilateral ones, both for major tracts such as the cerebellothalamic pathway and for thin, diffuse projections such as those of the LC.

5. Bibliography

Andersson, G., & Oscarsson, O. (1978). Climbing fiber microzones in cerebellar vermis and their projection to different groups of cells in the lateral vestibular nucleus. Experimental Brain Research, 32(4), 565–579. https://doi.org/10.1007/BF00239553

Ando, T., Ueda, M., Luo, Y., & Sugihara, I. (2020). Heterogeneous vestibulocerebellar mossy fiber projections revealed by single axon reconstruction in the mouse. Journal of Comparative Neurology, 528(10), 1775–1802. https://doi.org/10.1002/cne.24853

Anguat, P., & Cicirata, F. (1982). Cerebello-olivary projections in the rat. An autoradiographic study. Brain, Behavior and Evolution, 21(1), 24–33. https://doi.org/10.1159/000121612

Apps, R., & Garwicz, M. (2005). Anatomical and physiological foundations of cerebellar information processing. Nature Reviews Neuroscience, 6(4), 297–311. https://doi.org/10.1038/nrn1646

Apps, R., Hawkes, R., Aoki, S., Bengtsson, F., Brown, A. M., Chen, G., Ebner, T. J., Isope, P., Jörntell, H., Lackey, E. P., Lawrenson, C., Lumb, B., Schonewille, M., Sillitoe, R. V., Spaeth, L., Sugihara, I., Valera, A., Voogd, J., Wylie, D. R., & Ruigrok, T. J. H. (2018). Cerebellar Modules and Their Role as Operational Cerebellar Processing Units. The Cerebellum, 17(5), 654–682. https://doi.org/10.1007/s12311-018-0952-3

Asanuma, C., Thach, W. T., & Jones, E. G. (1983a). Anatomical evidence for segregated focal groupings of efferent cells and their terminal ramifications in the cerebellothalamic pathway of the monkey. Brain Research Reviews, 5(3), 267–297. https://doi.org/10.1016/0165-0173(83)90016-4

Asanuma, C., Thach, W. T., & Jones, E. G. (1983b). Distribution of cerebellar terminations and their relation to other afferent terminations in the ventral lateral thalamic region of the monkey. Brain Research Reviews, 5(3), 237–265. https://doi.org/10.1016/0165-0173(83)90015-2

Azizi, S. A., Mihailoff, G. A., Burne, R. A., & Woodward, D. J. (1981). The pontocerebellar system in the rat: An HRP study. I. Posterior vermis. Journal of Comparative Neurology, 197(4), 543–558. https://doi.org/10.1002/cne.901970402

Baek, S. J., Park, J. S., Kim, J., Yamamoto, Y., & Tanaka-Yamamoto, K. (2022). VTA-projecting cerebellar neurons mediate stress-dependent depression-like behaviors. eLife, 11, e72981. https://doi.org/10.7554/eLife.72981

Baizer, J. S., Sherwood, C. C., Hof, P. R., Witelson, S. F., & Sultan, F. (2011). Neurochemical and structural organization of the principal nucleus of the inferior olive in the human. Anatomical Record, 294(7), 1198–1216. https://doi.org/10.1002/ar.21400

Bandler, R., Carrive, P., & Depaulis, A. (1991). Emerging Principles of Organization of the Midbrain Periaqueductal Gray Matter. In A. Depaulis & R. Bandler (Eds.), The Midbrain Periaqueductal Gray Matter: Functional, Anatomical, and Neurochemical Organization (pp. 1–8). Springer US. https://doi.org/10.1007/978-1-4615-3302-3_1

Barmack, N. H. (2003). Central vestibular system: Vestibular nuclei and posterior cerebellum. Brain Research Bulletin, Functional Anatomy of Ear Connections, 60(5), 511–541. https://doi.org/10.1016/S0361-9230(03)00055-8

Basile, G. A., Quartu, M., Bertino, S., Serra, M. P., Boi, M., Bramanti, A., Anastasi, G. P., Milardi, D., & Cacciola, A. (2021). Red nucleus structure and function: From anatomy to clinical neurosciences. Brain Structure and Function, 226(1), 69–91. https://doi.org/10.1007/s00429-020-02171-x

Basser, P. J., Mattiello, J., & LeBihan, D. (1994). MR diffusion tensor spectroscopy and imaging. Biophysical Journal, 66(1), 259–267. https://doi.org/10.1016/S0006-3495(94)80775-1

Basser, P. J., Pajevic, S., Pierpaoli, C., Duda, J., & Aldroubi, A. (2000). In vivo fiber tractography using DT-MRI data. Magnetic Resonance in Medicine, 44(4), 625–632. https://doi.org/10.1002/1522-2594(200010)44:4%3C625::AID-MRM17%3E3.0.CO;2-O

Batton, R. R., Jayaraman, A., Ruggiero, D., & Carpenter, M. B. (1977a). Fastigial efferent projections in the monkey: An autoradiographic study. Journal of Comparative Neurology, 174(2), 281–305. https://doi.org/10.1002/cne.901740206

Batton, R. R., Jayaraman, A., Ruggiero, D., & Carpenter, M. B. (1977b). Fastigial efferent projections in the monkey: An autoradiographic study. Journal of Comparative Neurology, 174(2), 281–305. https://doi.org/10.1002/cne.901740206

Behrens, T. E. J., Woolrich, M. W., Jenkinson, M., Johansen-Berg, H., Nunes, R. G., Clare, S., Matthews, P. M., Brady, J. M., & Smith, S. M. (2003). Characterization and propagation of uncertainty in diffusion-weighted MR imaging. Magnetic Resonance in Medicine, 50(5), 1077–1088. https://doi.org/10.1002/mrm.10609

Beitz, A. J. (1982). The organization of afferent projections to the midbrain periaqueductal gray of the rat. Neuroscience, 7(1), 133–159. https://doi.org/10.1016/0306-4522(82)90157-9

Benagiano, V., & Rizzi, A. (2024). Autonomic functions of the cerebellum: Anatomical bases and clinical implications. Italian Journal of Anatomy and Embryology, 128(2), 113–123. https://doi.org/10.36253/ijae-15756

Blanks, R. H. I., Precht, W., & Torigoe, Y. (1983). Afferent projections to the cerebellar flocculus in the pigmented rat demonstrated by retrograde transport of horseradish peroxidase. Experimental Brain Research, 52(2). https://doi.org/10.1007/BF00236639

Bobillier, P., Seguin, S., Petitjean, F., Salvert, D., Touret, M., & Jouvet, M. (1976). The raphe nuclei of the cat brain stem: A topographical atlas of their efferent projections as revealed by autoradiography. Brain Research, 113(3), 449–486. https://doi.org/10.1016/0006-8993(76)90050-0

Boonstra, J. T. (2025). The cerebellar connectome. Behavioural Brain Research, 482, 115457. https://doi.org/10.1016/j.bbr.2025.115457

Brand, S., Dahl, A. L., & Mugnaini, E. (1976). The length of parallel fibers in the cat cerebellar cortex. An experimental light and electron microscopic study. Experimental Brain Research, 26(1). https://doi.org/10.1007/BF00235248

Brodal, P. (1979). The pontocerebellar projection in the rhesus monkey: An experimental study with retrograde axonal transport of horseradish peroxidase. Neuroscience, 4(2), 193–208. https://doi.org/10.1016/0306-4522(79)90082-4

Brodal, P. (1980). The projection from the nucleus reticularis tegmenti pontis to the cerebellum in the rhesus monkey. Experimental Brain Research, 38(1). https://doi.org/10.1007/BF00237927

Brodal, P., & Bjaalie, J. G. (1992). Organization of the pontine nuclei. Neuroscience Research, 13(2), 83–118. https://doi.org/10.1016/0168-0102(92)90092-q

Bullmore, E., & Sporns, O. (2009). Complex brain networks: Graph theoretical analysis of structural and functional systems. Nature Reviews Neuroscience, 10(3), 186–198. https://doi.org/10.1038/nrn2575

Cacciola, A., Milardi, D., Basile, G. A., Bertino, S., Calamuneri, A., Chillemi, G., Paladina, G., Impellizzeri, F., Trimarchi, F., Anastasi, G., Bramanti, A., & Rizzo, G. (2019). The cortico-rubral and cerebello-rubral pathways are topographically organized within the human red nucleus. Scientific Reports, 9(1), 12117. https://doi.org/10.1038/s41598-019-48164-7

Carta, I., Chen, C. H., Schott, A. L., Dorizan, S., & Khodakhah, K. (2019). Cerebellar modulation of the reward circuitry and social behavior. Science, 363(6424), eaav0581. https://doi.org/10.1126/science.aav0581

Cedarbaum, J. M., & Aghajanian, G. K. (1978). Afferent projections to the rat locus coeruleus as determined by a retrograde tracing technique. Journal of Comparative Neurology, 178(1), 1–15. https://doi.org/10.1002/cne.901780102

Champney, T. (2023). Essential clinical neuroanatomy (Second edition). Wiley-Blackwell.

Cicirata, F., Zappalà, A., Serapide, M. F., Parenti, R., Pantò, M. R., & Paz, C. (2005). Different pontine projections to the two sides of the cerebellum. Brain Research Reviews, Embryonic Chimeras and Transplantation for the Study of CNS Development and Regeneration, 49(2), 280–294. https://doi.org/10.1016/j.brainresrev.2005.02.002

Coenen, V. A., Sajonz, B., Prokop, T., Reisert, M., Piroth, T., Urbach, H., Jenkner, C., & Reinacher, P. C. (2020). The dentato-rubro-thalamic tract as the potential common deep brain stimulation target for tremor of various origin: An observational case series. Acta Neurochirurgica, 162(5), 1053–1066. https://doi.org/10.1007/s00701-020-04248-2

Cullen, K. E. (2023). Internal models of self-motion: Neural computations by the vestibular cerebellum. Trends in Neurosciences, 46(11), 986–1002. https://doi.org/10.1016/j.tins.2023.08.009

Daducci, A., Dal Palù, A., Lemkaddem, A., & Thiran, J.-P. (2015). COMMIT: Convex Optimization Modeling for Microstructure Informed Tractography. IEEE Transactions on Medical Imaging, 34(1), 246–257. https://doi.org/10.1109/TMI.2014.2352414

Dell'Acqua, F., & Tournier, J.-D. (2019). Modelling white matter with spherical deconvolution: How and why? NMR in Biomedicine, 32(4), e3945. https://doi.org/10.1002/nbm.3945

Diedrichsen, J., Balsters, J. H., Flavell, J., Cussans, E., & Ramnani, N. (2009). A probabilistic MR atlas of the human cerebellum. NeuroImage, 46(1), 39–46. https://doi.org/10.1016/j.neuroimage.2009.01.045

Diedrichsen, J., Maderwald, S., Küper, M., Thürling, M., Rabe, K., Gizewski, E. R., Ladd, M. E., & Timmann, D. (2011). Imaging the deep cerebellar nuclei: A probabilistic atlas and normalization procedure. NeuroImage, 54(3), 1786–1794. https://doi.org/10.1016/j.neuroimage.2010.10.035

Dietrichs, E. (1988). Cerebellar cortical and nuclear afferents from the feline locus coeruleus complex. Neuroscience, 27(1), 77–91. https://doi.org/10.1016/0306-4522(88)90220-5

Dietrichs, E., & Walberg, F. (1981). The cerebellar nucleo-olivary projection in the cat. Anatomy and Embryology, 162(1), 51–67. https://doi.org/10.1007/BF00318094

Donahue, C. J., Sotiropoulos, S. N., Jbabdi, S., Hernandez-Fernandez, M., Behrens, T. E., Dyrby, T. B., Coalson, T., Kennedy, H., Knoblauch, K., Essen, D. C. V., & Glasser, M. F. (2016). Using Diffusion Tractography to Predict Cortical Connection Strength and Distance: A Quantitative Comparison with Tracers in the

Monkey. Journal of Neuroscience, 36(25), 6758–6770. https://doi.org/10.1523/JNEUROSCI.0493-16.2016
Dum, R. P., & Strick, P. L. (2003). An unfolded map of the cerebellar dentate nucleus and its projections to the cerebral cortex. Journal of Neurophysiology, 89(1), 634–639. https://doi.org/10.1152/jn.00626.2002
Ekerot, C. F., Garwicz, M., & Schouenborg, J. (1991). Topography and nociceptive receptive fields of climbing fibres projecting to the cerebellar anterior lobe in the cat. The Journal of Physiology, 441(1), 257–274. https://doi.org/10.1113/jphysiol.1991.sp018750
Epema, A. H., Gerrits, N., & Voogd, J. (1990). Secondary vestibulocerebellar projections to the flocculus and uvulo-nodular lobule of the rabbit: A study using HRP and double fluorescent tracer techniques. Experimental Brain Research, 80(1), 72–82. https://doi.org/10.1007/BF00228849
Fagiolo, G. (2007). Clustering in complex directed networks. Physical Review E, 76(2), 026107. https://doi.org/10.1103/PhysRevE.76.026107
Freeman, L. C. (1977). A Set of Measures of Centrality Based on Betweenness. Sociometry, 40(1), 35–41. https://doi.org/10.2307/3033543
Frontera, J. L., Baba Aissa, H., Sala, R. W., Mailhes-Hamon, C., Georgescu, I. A., Léna, C., & Popa, D. (2020). Bidirectional control of fear memories by cerebellar neurons projecting to the ventrolateral periaqueductal grey. Nature Communications, 11(1), 5207. https://doi.org/10.1038/s41467-020-18953-0
Fujita, H., Kodama, T., & Du Lac, S. (2020). Modular output circuits of the fastigial nucleus for diverse motor and nonmotor functions of the cerebellar vermis. eLife, 9, e58613. https://doi.org/10.7554/eLife.58613
Gacek, R. R. (1973). A cerebellocochlear nucleus pathway in the cat. Experimental Neurology, 41(1), 101–112. https://doi.org/10.1016/0014-4886(73)90183-0
Gayer, N. S., & Faull, R. L. M. (1988). Connections of the paraflocculus of the cerebellum with the superior colliculus in the rat brain. Brain Research, 449(1), 253–270. https://doi.org/10.1016/0006-8993(88)91042-6
Gibson, A. R., Horn, K. M., & Pong, M. (2023). Nucleus reticularis tegmenti pontis: A bridge between the basal ganglia and cerebellum for movement control. Experimental Brain Research, 241(5), 1271–1287. https://doi.org/10.1007/s00221-023-06574-0
Glickstein, M., & Doron, K. (2008). Cerebellum: Connections and Functions. The Cerebellum, 7(4), 589–594. https://doi.org/10.1007/s12311-008-0074-4
Glickstein, M., May, J. G., & Mercier, B. E. (1985). Corticopontine projection in the macaque: The distribution of labelled cortical cells after large injections of horseradish peroxidase in the pontine nuclei. The Journal of Comparative Neurology, 235(3), 343–359. https://doi.org/10.1002/cne.902350306
Gonzalo-Ruiz, A., Leichnetz, G. R., & Hardy, S. G. P. (1990). Projections of the medial cerebellar nucleus to oculomotor-related midbrain areas in the rat: An anterograde and retrograde HRP study. Journal of Comparative Neurology, 296(3), 427–436. https://doi.org/10.1002/cne.902960308
Granziera, C., Schmahmann, J. D., Hadjikhani, N., Meyer, H., Meuli, R., Wedeen, V., & Krueger, G. (2009). Diffusion Spectrum Imaging Shows the Structural Basis of Functional Cerebellar Circuits in the Human Cerebellum In Vivo. PLOS ONE, 4(4), e5101. https://doi.org/10.1371/journal.pone.0005101
Groenewegen, H. J., Voogd, J., & Freedman, S. L. (1979). The parasagittal zonation within the olivocerebellar projection. II. Climbing fiber distribution in the intermediate and hemispheric parts of cat cerebellum. Journal of Comparative Neurology, 183(3), 551–601. https://doi.org/10.1002/cne.901830307
Grover, V. P. B., Tognarelli, J. M., Crossey, M. M. E., Cox, I. J., Taylor-Robinson, S. D., & McPhail, M. J. W. (2015). Magnetic Resonance Imaging: Principles and Techniques: Lessons for Clinicians. Journal of Clinical and Experimental Hepatology, 5(3), 246–255. https://doi.org/10.1016/j.jceh.2015.08.001
Gruol, D. L., Koibuchi, N., Manto, M., Molinari, M., Schmahmann, J. D., & Shen, Y. (Eds.). (2016). Essentials of Cerebellum and Cerebellar Disorders. Springer International Publishing. https://doi.org/10.1007/978-3-319-24551-5
Hagmann, P., Kurant, M., Gigandet, X., Thiran, P., Wedeen, V. J., Meuli, R., & Thiran, J.-P. (2007). Mapping Human Whole-Brain Structural Networks with Diffusion MRI. PLoS ONE, 2(7), e597. https://doi.org/10.1371/journal.pone.0000597
Haines, D. E., & Dietrichs, E. (1984). An HRP study of hypothalamo-cerebellar and cerebello-hypothalamic connections in squirrel monkey (saimiri sciureus). Journal of Comparative Neurology, 229(4), 559–575. https://doi.org/10.1002/cne.902290409
Han, K.-S., Chen, C. H., Khan, M. M., Guo, C., & Regehr, W. G. (2020). Climbing fiber synapses rapidly and transiently inhibit neighboring Purkinje cells via ephaptic coupling. Nature Neuroscience, 23(11), 1399–1409. https://doi.org/10.1038/s41593-020-0701-z
Haroian, A. J., Massopust, L. C., & Young, P. A. (1981). Cerebellothalamic projections in the rat: An autoradiographic and degeneration study. The Journal of Comparative Neurology, 197(2), 217–236. https://doi.org/10.1002/cne.901970205

Harper, J. W., & Heath, R. G. (1973). Anatomic connections of the fastigial nucleus to the rostral forebrain in the cat. Experimental Neurology, 39(2), 285–292. https://doi.org/10.1016/0014-4886(73)90231-8
Hashimoto, M., Yamanaka, A., Kato, S., Tanifuji, M., Kobayashi, K., & Yaginuma, H. (2018). Anatomical Evidence for a Direct Projection from Purkinje Cells in the Mouse Cerebellar Vermis to Medial Parabrachial Nucleus. Frontiers in Neural Circuits, 12, 6. https://doi.org/10.3389/fncir.2018.00006
Hazrati, L.-N., & Parent, A. (1992). Projection from the deep cerebellar nuclei to the pedunculopontine nucleus in the squirrel monkey. Brain Research, 585(1–2), 267–271. https://doi.org/10.1016/0006-8993(92)91216-2
Heath, R. G., & Harper, J. W. (1974). Ascending projections of the cerebellar fastigial nucleus to the hippocampus, amygdala, and other temporal lobe sites: Evoked potential and histological studies in monkeys and cats. Experimental Neurology, 45(2), 268–287. https://doi.org/10.1016/0014-4886(74)90118-6
Hoddevik, G. H. (1977). The pontine projection to the flocculonodular lobe and the paraflocculus studied by means of retrograde axonal transport of horseradish peroxidase in the rabbit. Experimental Brain Research, 30(4). https://doi.org/10.1007/BF00237641
Huang, C.-M., Liu, G., & Huang, R. (1982). Projections from the cochlear nucleus to the cerebellum. Brain Research, 244(1), 1–8. https://doi.org/10.1016/0006-8993(82)90897-6
Hull, C., & Regehr, W. G. (2022). The Cerebellar Cortex. Annual Review of Neuroscience, 45, 151–175. https://doi.org/10.1146/annurev-neuro-091421-125115
Hwang, K.-D., Baek, J., Ryu, H.-H., Lee, J., Shim, H. G., Kim, S. Y., Kim, S. J., & Lee, Y.-S. (2023). Cerebellar nuclei neurons projecting to the lateral parabrachial nucleus modulate classical fear conditioning. Cell Reports, 42(4), 112291. https://doi.org/10.1016/j.celrep.2023.112291
Ikai, Y., Takada, M., Shinonaga, Y., & Mizuno, N. (1992). Dopaminergic and non-dopaminergic neurons in the ventral tegmental area of the rat project, respectively, to the cerebellar cortex and deep cerebellar nuclei. Neuroscience, 51(3), 719–728. https://doi.org/10.1016/0306-4522(92)90310-X
Ikeda, M. (1979). Projections from the spinal and the principal sensory nuclei of the trigeminal nerve to the cerebellar cortex in the cat, as studied by retrograde transport of horseradish peroxidase. Journal of Comparative Neurology, 184(3), 567–585. https://doi.org/10.1002/cne.901840309
Isa, T., Marquez-Legorreta, E., Grillner, S., & Scott, E. K. (2021). The tectum/superior colliculus as the vertebrate solution for spatial sensory integration and action. Current Biology, 31(11), R741–R762. https://doi.org/10.1016/j.cub.2021.04.001
Jbabdi, S., & Johansen-Berg, H. (2011). Tractography: Where Do We Go from Here? Brain Connectivity, 1(3), 169–183. https://doi.org/10.1089/brain.2011.0033
Jeurissen, B., Leemans, A., Tournier, J., Jones, D. K., & Sijbers, J. (2013). Investigating the prevalence of complex fiber configurations in white matter tissue with diffusion magnetic resonance imaging. Human Brain Mapping, 34(11), 2747–2766. https://doi.org/10.1002/hbm.22099
Jeurissen, B., Tournier, J.-D., Dhollander, T., Connelly, A., & Sijbers, J. (2014). Multi-tissue constrained spherical deconvolution for improved analysis of multi-shell diffusion MRI data. NeuroImage, 103, 411–426. https://doi.org/10.1016/j.neuroimage.2014.07.061
Jones, D. K., Knösche, T. R., & Turner, R. (2013). White matter integrity, fiber count, and other fallacies: The do's and don'ts of diffusion MRI. NeuroImage, 73, 239–254. https://doi.org/10.1016/j.neuroimage.2012.06.081
Judd, E. N., Lewis, S. M., & Person, A. L. (2021). Diverse inhibitory projections from the cerebellar interposed nucleus. eLife, 10, e66231. https://doi.org/10.7554/eLife.66231
Kalil, K. (1981). Projections of the cerebellar and dorsal column nuclei upon the thalamus of the rhesus monkey. Journal of Comparative Neurology, 195(1), 25–50. https://doi.org/10.1002/cne.901950105
Katoh, Y. Y., & Deura, S. (1993). Direct projections from the cerebellar fastigial nucleus to the thalamic supragenículate nucleus in the cat studied with the anterograde and retrograde axonal transport of wheat germ agglutinin-horseradish peroxidase. Brain Research, 617(1), 155–158. https://doi.org/10.1016/0006-8993(93)90628-Z
Kebschull, J. M., Casoni, F., Consalez, G. G., Goldowitz, D., Hawkes, R., Ruigrok, T. J. H., Schilling, K., Wingate, R., Wu, J., Yeung, J., & Uusisaari, M. Y. (2023). Cerebellum Lecture: The Cerebellar Nuclei—Core of the Cerebellum. The Cerebellum, 23(2), 620–677. https://doi.org/10.1007/s12311-022-01506-0
Kelly, R. M., & Strick, P. L. (2003). Cerebellar loops with motor cortex and prefrontal cortex of a nonhuman primate. The Journal of Neuroscience: The Official Journal of the Society for Neuroscience, 23(23), 8432–8444. https://doi.org/10.1523/JNEUROSCI.23-23-08432.2003
Kotchabhakdi, N., & Walberg, F. (1977). Cerebellar afferents from neurons in motor nuclei of cranial nerves demonstrated by retrograde axonal transport of horseradish peroxidase. Brain Research, 137(1), 158–163. https://doi.org/10.1016/0006-8993(77)91020-4

Kratochwil, C. F., Maheshwari, U., & Rijli, F. M. (2017). The Long Journey of Pontine Nuclei Neurons: From Rhombic Lip to Cortico-Ponto-Cerebellar Circuitry. Frontiers in Neural Circuits, 11. https://doi.org/10.3389/fncir.2017.00033

Lapresle, J. (1970). The Dentato-olivary Pathway: Somatotopic Relationship Between the Dentate Nucleus and the Contralateral Inferior Olive. Archives of Neurology, 22(2), 135. https://doi.org/10.1001/archneur.1970.00480200041004

Lara-Aparicio, S. Y., Laureani-Fierro, A. J., Morgado-Valle, C., Beltrán-Parrazal, L., Rojas-Durán, F., García, L. I., Toledo-Cárdenas, R., Hernández, M. E., Manzo, J., & Pérez, C. A. (2022). Latest research on the anatomy and physiology of the cerebellum. Neurology Perspectives, 2(1), 34–46. https://doi.org/10.1016/j.neurop.2021.12.002

Larsell, O. (1952). The morphogenesis and adult pattern of the lobules and fissures of the cerebellum of the white rat. Journal of Comparative Neurology, 97(2), 281–356. https://doi.org/10.1002/cne.900970204

Larsell, O., & Jansen, J. (1972). The comparative anatomy and histology of the cerebellum. 3: The human cerebellum, cerebellar connections, and cerebellar cortex / by Olof Larsell and Jan Jansen. With chapters by Helge K. Korneliussen and Enrico Mugnaini. Univ. of Minnesota Press.

Lau, J. C., Xiao, Y., Haast, R. A. M., Gilmore, G., Uludag, K., MacDougall, K. W., Menon, R. S., Parrent, A. G., Peters, T. M., & Khan, A. R. (2020). Direct visualization and characterization of the human zona incerta and surrounding structures. Neuroscience. https://doi.org/10.1101/2020.03.25.008318

Lawrenson, C., Paci, E., Pickford, J., Drake, R. A., Lumb, B. M., & Apps, R. (2022). Cerebellar modulation of memory encoding in the periaqueductal grey and fear behaviour. eLife, 11, e76278. https://doi.org/10.7554/eLife.76278

Lehman, V. T., Black, D. F., DeLone, D. R., Blezek, D. J., Kaufmann, T. J., Brinjikji, W., & Welker, K. M. (2020). Current concepts of cross-sectional and functional anatomy of the cerebellum: A pictorial review and atlas. The British Journal of Radiology, 93(1106), 20190467. https://doi.org/10.1259/bjr.20190467

Lundell, H., & Steele, C. J. (2024). Cerebellar imaging with diffusion magnetic resonance imaging: Approaches, challenges, and potential. Current Opinion in Behavioral Sciences, 56, 101353. https://doi.org/10.1016/j.cobeha.2024.101353

Luo, Y., Chao, Y., Owusu-Mensah, R. N. A., Zhang, J., Hirata, T., & Sugihara, I. (2023). Neurogenic timing of the inferior olive subdivisions is related to the olivocerebellar projection topography. Scientific Reports, 13(1), 7114. https://doi.org/10.1038/s41598-023-33497-1

Luo, Y., Fujita, H., Nedelescu, H., Biswas, M. S., Sato, C., Ying, S., Takahashi, M., Akita, K., Higashi, T., Aoki, I., & Sugihara, I. (2017). Lobular homology in cerebellar hemispheres of humans, non-human primates and rodents: A structural, axonal tracing and molecular expression analysis. Brain Structure and Function, 222(6), 2449–2472. https://doi.org/10.1007/s00429-017-1436-9

Luppi, P.-H., Aston-Jones, G., Akaoka, H., Chouvet, G., & Jouvet, M. (1995). Afferent projections to the rat locus coeruleus demonstrated by retrograde and anterograde tracing with cholera-toxin B subunit and Phaseolus vulgaris leucoagglutinin. Neuroscience, 65(1), 119–160. https://doi.org/10.1016/0306-4522(94)00481-J

Lyu, W., Wu, Y., Huynh, K. M., Ahmad, S., & Yap, P.-T. (2024). A multimodal submillimeter MRI atlas of the human cerebellum. Scientific Reports, 14(1), 5622. https://doi.org/10.1038/s41598-024-55412-y

MacKay, R. S., Johnson, S., & Sansom, B. (2020). How directed is a directed network? Royal Society Open Science, 7(9), 201138. https://doi.org/10.1098/rsos.201138

Maier-Hein, K. H., Neher, P. F., Houde, J.-C., Côté, M.-A., Garyfallidis, E., Zhong, J., Chamberland, M., Yeh, F.-C., Lin, Y.-C., Ji, Q., Reddick, W. E., Glass, J. O., Chen, D. Q., Feng, Y., Gao, C., Wu, Y., Ma, J., He, R., Li, Q., … Descoteaux, M. (2017). The challenge of mapping the human connectome based on diffusion tractography. Nature Communications, 8(1), 1349. https://doi.org/10.1038/s41467-017-01285-x

Makris, N., Hodge, S. M., Haselgrove, C., Kennedy, D. N., Dale, A., Fischl, B., Rosen, B. R., Harris, G., Caviness, V. S., & Schmahmann, J. D. (2003). Human cerebellum: Surface-assisted cortical parcellation and volumetry with magnetic resonance imaging. Journal of Cognitive Neuroscience, 15(4), 584–599. https://doi.org/10.1162/089892903321662967

Middleton, F. A., & Strick, P. L. (1994). Anatomical Evidence for Cerebellar and Basal Ganglia Involvement in Higher Cognitive Function. Science, 266(5184), 458–461. https://doi.org/10.1126/science.7939688

Middleton, F. A., & Strick, P. L. (2001). Cerebellar Projections to the Prefrontal Cortex of the Primate. The Journal of Neuroscience, 21(2), 700–712. https://doi.org/10.1523/JNEUROSCI.21-02-00700.2001

Mihailoff, G. A., Lee, H., Watt, C. B., & Yates, R. (1985). Projections to the basilar pontine nuclei from face sensory and motor regions of the cerebral cortex in the rat. Journal of Comparative Neurology, 237(2), 251–263. https://doi.org/10.1002/cne.902370209

Mitrofanis, J., & deFonseka, R. (2001). Organisation of connections between the zona incerta and the interposed nucleus. Anatomy and Embryology, 204(2), 153–159. https://doi.org/10.1007/s004290100187

Mori, S., Crain, B. J., Chacko, V. P., & Van Zijl, P. C. M. (1999). Three-dimensional tracking of axonal projections in the brain by magnetic resonance imaging. Annals of Neurology, 45(2), 265–269. https://doi.org/10.1002/1531-8249(199902)45:2%3C265::AID-ANA21%3E3.0.CO;2-3

Nakamura, H. (2018). Cerebellar projections to the ventral lateral geniculate nucleus and the thalamic reticular nucleus in the cat. Journal of Neuroscience Research, 96(1), 63–74. https://doi.org/10.1002/jnr.24105

Nieuwenhuys, R., Voogd, J., & van Huijzen, C. (Eds.). (2008). Topography of Spinal Cord, Brain Stem and Cerebellum. In The Human Central Nervous System (pp. 177–245). Springer. https://doi.org/10.1007/978-3-540-34686-9_6

Novello, M., Bosman, L. W. J., & De Zeeuw, C. I. (2024). A Systematic Review of Direct Outputs from the Cerebellum to the Brainstem and Diencephalon in Mammals. Cerebellum (London, England), 23(1), 210–239. https://doi.org/10.1007/s12311-022-01499-w

Ogut, E., Armagan, K., & Tufekci, D. (2023). The Guillain-Mollaret triangle: A key player in motor coordination and control with implications for neurological disorders. Neurosurgical Review, 46(1), 181. https://doi.org/10.1007/s10143-023-02086-1

Oka, H., Yoshida, K., Yamamoto, T., & Samejima, A. (1985). Organization of afferent connections to the lateral and interpositus cerebellar nuclei from the brainstem relay nuclei: A horseradish peroxidase study in the cat. Neuroscience Research, 2(5), 321–333. https://doi.org/10.1016/0168-0102(85)90044-6

Palesi, F., De Rinaldis, A., Castellazzi, G., Calamante, F., Muhlert, N., Chard, D., Tournier, J. D., Magenes, G., D'Angelo, E., & Gandini Wheeler-Kingshott, C. A. M. (2017). Contralateral cortico-ponto-cerebellar pathways reconstruction in humans in vivo: Implications for reciprocal cerebro-cerebellar structural connectivity in motor and non-motor areas. Scientific Reports, 7(1), 12841. https://doi.org/10.1038/s41598-017-13079-8

Palesi, F., Tournier, J.-D., Calamante, F., Muhlert, N., Castellazzi, G., Chard, D., D'Angelo, E., & Wheeler-Kingshott, C. A. M. (2015). Contralateral cerebello-thalamo-cortical pathways with prominent involvement of associative areas in humans in vivo. Brain Structure and Function, 220(6), 3369–3384. https://doi.org/10.1007/s00429-014-0861-2

Parenti, R., Zappalà, A., Serapide, M. F., Pantò, M. R., & Cicirata, F. (2002). Projections of the basilar pontine nuclei and nucleus reticularis tegmenti pontis to the cerebellar nuclei of the rat. Journal of Comparative Neurology, 452(2), 115–127. https://doi.org/10.1002/cne.10316

Patay, Z., Enterkin, J., Harreld, J. H., Yuan, Y., Lobel, U., Rumboldt, Z., Khan, R., & Boop, F. (2014). MR Imaging Evaluation of Inferior Olivary Nuclei: Comparison of Postoperative Subjects with and without Posterior Fossa Syndrome. American Journal of Neuroradiology, 35(4), 797–802. https://doi.org/10.3174/ajnr.A3762

Patenaude, B., Smith, S. M., Kennedy, D. N., & Jenkinson, M. (2011). A Bayesian model of shape and appearance for subcortical brain segmentation. NeuroImage, 56(3), 907–922. https://doi.org/10.1016/j.neuroimage.2011.02.046

Pierce, E. T., Hoddevik, G. H., & Walberg, F. (1977). The cerebellar projection from the raphe nuclei in the cat as studied with the method of retrograde transport of horseradish peroxidase. Anatomy and Embryology, 152(1), 73–87. https://doi.org/10.1007/BF00341436

Pisano, T. J., Dhanerawala, Z. M., Kislin, M., Bakshinskaya, D., Engel, E. A., Hansen, E. J., Hoag, A. T., Lee, J., Oude, N. L. de, Venkataraju, K. U., Verpeut, J. L., Hoebeek, F. E., Richardson, B. D., Boele, H.-J., & Wang, S. S.-H. (2021). Homologous organization of cerebellar pathways to sensory, motor, and associative forebrain. Cell Reports, 36(12). https://doi.org/10.1016/j.celrep.2021.109721

Quaia, C., Lefèvre, P., & Optican, L. M. (1999). Model of the Control of Saccades by Superior Colliculus and Cerebellum. Journal of Neurophysiology, 82(2), 999–1018. https://doi.org/10.1152/jn.1999.82.2.999

Rahimi-Balaei, M., Afsharinezhad, P., Bailey, K., Buchok, M., Yeganeh, B., & Marzban, H. (2015). Embryonic stages in cerebellar afferent development. Cerebellum & Ataxias, 2(1), 7. https://doi.org/10.1186/s40673-015-0026-y

Rodella, L., Rezzani, R., Corsetti, G., Simonetti, C., Stacchiotti, A., & Ventura, R. G. (1995). A light and electron microscope study of rat abducens nucleus neurons projecting to the cerebellar flocculus. Journal of Anatomy, 186 (Pt 2)(Pt 2), 357–363.

Rogers, A., & Beier, K. T. (2021). Can transsynaptic viral strategies be used to reveal functional aspects of neural circuitry? Journal of Neuroscience Methods, 348, 109005. https://doi.org/10.1016/j.jneumeth.2020.109005

Roldan, M., & Reinoso-Suarez, F. (1981). Cerebellar projections to the superior colliculus in the cat. The Journal of Neuroscience, 1(8), 827–834. https://doi.org/10.1523/JNEUROSCI.01-08-00827.1981

Rousseau, P.-N., Chakravarty, M. M., & Steele, C. J. (2022). Mapping pontocerebellar connectivity with diffusion MRI. NeuroImage, 264, 119684. https://doi.org/10.1016/j.neuroimage.2022.119684

Rubinov, M., & Sporns, O. (2010). Complex network measures of brain connectivity: Uses and interpretations. NeuroImage, Computational Models of the Brain, 52(3), 1059–1069. https://doi.org/10.1016/j.neuroimage.2009.10.003

Ruigrok, T. J. H. (2011). Ins and Outs of Cerebellar Modules. The Cerebellum, 10(3), 464–474. https://doi.org/10.1007/s12311-010-0164-y

Ruigrok, T. J. H. (2016). Spinocerebellar and Cerebellospinal Pathways. In D. L. Gruol, N. Koibuchi, M. Manto, M. Molinari, J. D. Schmahmann, & Y. Shen (Eds.), Essentials of Cerebellum and Cerebellar Disorders: A Primer For Graduate Students (pp. 79–88). Springer International Publishing. https://doi.org/10.1007/978-3-319-24551-5_9

Ruigrok, T. J., & Voogd, J. (1990). Cerebellar nucleo-olivary projections in the rat: An anterograde tracing study with Phaseolus vulgaris-leucoagglutinin (PHA-L). The Journal of Comparative Neurology, 298(3), 315–333. https://doi.org/10.1002/cne.902980305

Ruigrok, T. J., & Voogd, J. (2000). Organization of projections from the inferior olive to the cerebellar nuclei in the rat. The Journal of Comparative Neurology, 426(2), 209–228. https://doi.org/10.1002/1096-9861(20001016)426:2%3C209::aid-cne4%3E3.0.co;2-0

R□ste, G. K. (1989). Non-motoneurons in the facial and motor trigeminal nuclei projecting to the cerebellar flocculus in the cat: A fluorescent double-labelling and WGA-HRP study. Experimental Brain Research, 75(2). https://doi.org/10.1007/BF00247935

Sadakane, K., Kondo, M., & Nisimaru, N. (2000). Direct projection from the cardiovascular control region of the cerebellar cortex, the lateral nodulus-uvula, to the brainstem in rabbits. Neuroscience Research, 36(1), 15–26. https://doi.org/10.1016/s0168-0102(99)00103-0

Sakai, S. T., Inase, M., & Tanji, J. (1996). Comparison of cerebellothalamic and pallidothalamic projections in the monkey (Macaca fuscata): A double anterograde labeling study. The Journal of Comparative Neurology, 368(2), 215–228. https://doi.org/10.1002/(SICI)1096-9861(19960429)368:2%3C215::AID-CNE4%3E3.0.CO;2-6

Saluja, S., Qiu, L., Wang, A. R., Campos, G., Seilheimer, R., McNab, J. A., Haber, S. N., Barbosa, D. A. N., & Halpern, C. H. (2024). Diffusion Magnetic Resonance Imaging Tractography Guides Investigation of the Zona Incerta: A Novel Target for Deep Brain Stimulation. Biological Psychiatry, 96(6), 445–454. https://doi.org/10.1016/j.biopsych.2024.02.1004

Schilling, K. G., Nath, V., Hansen, C., Parvathaneni, P., Blaber, J., Gao, Y., Neher, P., Aydogan, D. B., Shi, Y., Ocampo-Pineda, M., Schiavi, S., Daducci, A., Girard, G., Barakovic, M., Rafael-Patino, J., Romascano, D., Rensonnet, G., Pizzolato, M., Bates, A., … Landman, B. A. (2019). Limits to anatomical accuracy of diffusion tractography using modern approaches. NeuroImage, 185, 1–11. https://doi.org/10.1016/j.neuroimage.2018.10.029

Schmahmann, J. D. (2016). The Cerebrocerebellar System. In D. L. Gruol, N. Koibuchi, M. Manto, M. Molinari, J. D. Schmahmann, & Y. Shen (Eds.), Essentials of Cerebellum and Cerebellar Disorders: A Primer For Graduate Students (pp. 101–115). Springer International Publishing. https://doi.org/10.1007/978-3-319-24551-5

Schmahmann, J. D., Doyon, J., McDonald, D., Holmes, C., Lavoie, K., Hurwitz, A. S., Kabani, N., Toga, A., Evans, A., & Petrides, M. (1999). Three-Dimensional MRI Atlas of the Human Cerebellum in Proportional Stereotaxic Space. NeuroImage, 10(3), 233–260. https://doi.org/10.1006/nimg.1999.0459

Schmahmann, J. D., & Pandya, D. N. (1997). The Cerebrocerebellar System. In International Review of Neurobiology (Vol. 41, pp. 31–60). Elsevier. https://doi.org/10.1016/S0074-7742(08)60346-3

Serapide, M. F., Parenti, R., Pantò, M. R., Zappalà, A., & Cicirata, F. (2002). Multiple zonal projections of the nucleus reticularis tegmenti pontis to the cerebellar cortex of the rat. The European Journal of Neuroscience, 15(11), 1854–1858. https://doi.org/10.1046/j.1460-9568.2002.02029.x

Sereno, M. I., Diedrichsen, J., Tachrount, M., Testa-Silva, G., d'Arceuil, H., & De Zeeuw, C. (2020). The human cerebellum has almost 80% of the surface area of the neocortex. Proceedings of the National Academy of Sciences of the United States of America, 117(32), 19538–19543. https://doi.org/10.1073/pnas.2002896117

Shammah-Lagnado, S. J., Negra˜o, N., Silva, B. A., & Ricardo, J. A. (1987). Afferent connections of the nuclei reticularis pontis oralis and caudalis: A horseradish peroxidase study in the rat. Neuroscience, 20(3), 961–989. https://doi.org/10.1016/0306-4522(87)90256-9

Shin, M., Moghadam, S. H., Sekirnjak, C., Bagnall, M. W., Kolkman, K. E., Jacobs, R., Faulstich, M., & Du Lac, S. (2011). Multiple Types of Cerebellar Target Neurons and Their Circuitry in the Vestibulo-ocular Reflex. Journal of Neuroscience, 31(30), 10776–10786. https://doi.org/10.1523/JNEUROSCI.0768-11.2011

Shojaku, H., Sato, Y., Ikarashi, K., & Kawasaki, T. (1987). Topographical distribution of Purkinje cells in the uvula and the nodulus projecting to the vestibular nuclei in cats. Brain Research, 416(1), 100–112. https://doi.org/10.1016/0006-8993(87)91501-0

Smith, R. E., Tournier, J.-D., Calamante, F., & Connelly, A. (2012a). Anatomically-constrained tractography: Improved diffusion MRI streamlines tractography through effective use of anatomical information. NeuroImage, 62(3), 1924–1938. https://doi.org/10.1016/j.neuroimage.2012.06.005

Smith, R. E., Tournier, J.-D., Calamante, F., & Connelly, A. (2012b). Anatomically-constrained tractography: Improved diffusion MRI streamlines tractography through effective use of anatomical information. NeuroImage, 62(3), 1924–1938. https://doi.org/10.1016/j.neuroimage.2012.06.005

Smith, R. E., Tournier, J.-D., Calamante, F., & Connelly, A. (2012c). Anatomically-constrained tractography: Improved diffusion MRI streamlines tractography through effective use of anatomical information. NeuroImage, 62(3), 1924–1938. https://doi.org/10.1016/j.neuroimage.2012.06.005

Smith, R. E., Tournier, J.-D., Calamante, F., & Connelly, A. (2015). SIFT2: Enabling dense quantitative assessment of brain white matter connectivity using streamlines tractography. NeuroImage, 119, 338–351. https://doi.org/10.1016/j.neuroimage.2015.06.092

Smith, S. M. (2002). Fast robust automated brain extraction. Human Brain Mapping, 17(3), 143–155. https://doi.org/10.1002/hbm.10062

Snider, R. S., Maiti, A., & Snider, S. R. (1976). Cerebellar pathways to ventral midbrain and nigra. Experimental Neurology, 53(3), 714–728. https://doi.org/10.1016/0014-4886(76)90150-3

Somana, R., Kotchabhakdi, N., & Walberg, F. (1980). Cerebellar afferents from the trigeminal sensory nuclei in the cat. Experimental Brain Research, 38(1). https://doi.org/10.1007/BF00237931

Somana, R., & Walberg, F. (1979). The cerebellar projection from locus coeruleus as studied with retrograde transport of horseradish peroxidase in the cat. Anatomy and Embryology, 155(1), 87–94. https://doi.org/10.1007/BF00315733

Stanton, G. B. (1980). Topographical organization of ascending cerebellar projections from the dentate and interposed nuclei in Macaca mulatta: An anterograde degeneration study. Journal of Comparative Neurology, 190(4), 699–731. https://doi.org/10.1002/cne.901900406

Steele, C. J., Anwander, A., Bazin, P.-L., Trampel, R., Schaefer, A., Turner, R., Ramnani, N., & Villringer, A. (2017). Human Cerebellar Sub-millimeter Diffusion Imaging Reveals the Motor and Non-motor Topography of the Dentate Nucleus. Cerebral Cortex, 27(9), 4537–4548. https://doi.org/10.1093/cercor/bhw258

Strick, P. L., Dum, R. P., & Fiez, J. A. (2009). Cerebellum and Nonmotor Function. Annual Review of Neuroscience, 32(1), 413–434. https://doi.org/10.1146/annurev.neuro.31.060407.125606

Sugihara, I., & Shinoda, Y. (2004). Molecular, Topographic, and Functional Organization of the Cerebellar Cortex: A Study with Combined Aldolase C and Olivocerebellar Labeling. Journal of Neuroscience, 24(40), 8771–8785. https://doi.org/10.1523/JNEUROSCI.1961-04.2004

Sultan, F., & Glickstein, M. (2007). The cerebellum: Comparative and animal studies. The Cerebellum, 6(3), 168. https://doi.org/10.1080/14734220701332486

Supple, W. F., & Kapp, B. S. (1994). Anatomical and physiological relationships between the anterior cerebellar vermis and the pontine parabrachial nucleus in the rabbit. Brain Research Bulletin, 33(5), 561–574. https://doi.org/10.1016/0361-9230(94)90082-5

Takahashi, E., Song, J. W., Folkerth, R. D., Grant, P. E., & Schmahmann, J. D. (2013). Detection of postmortem human cerebellar cortex and white matter pathways using high angular resolution diffusion tractography: A feasibility study. NeuroImage, 68, 105–111. https://doi.org/10.1016/j.neuroimage.2012.11.042

Teune, T. M., Der Burg, J., & Ruigrok, T. J. H. (1995). Cerebellar projections to the red nucleus and inferior olive originate from separate populations of neurons in the rat: A non-fluorescent double labeling study. Brain Research, 673(2), 313–319. https://doi.org/10.1016/0006-8993(94)01431-G

Teune, T. M., Van Der Burg, J., Van Der Moer, J., Voogd, J., & Ruigrok, T. J. H. (2000). Topography of cerebellar nuclear projections to the brain stem in the rat. In Progress in Brain Research (Vol. 124, pp. 141–172). Elsevier. https://doi.org/10.1016/S0079-6123(00)24014-4

Thomas, C., Ye, F. Q., Irfanoglu, M. O., Modi, P., Saleem, K. S., Leopold, D. A., & Pierpaoli, C. (2014). Anatomical accuracy of brain connections derived from diffusion MRI tractography is inherently limited. Proceedings of the National Academy of Sciences, 111(46), 16574–16579. https://doi.org/10.1073/pnas.1405672111

Tilikete, C., & Desestret, V. (2017). Hypertrophic Olivary Degeneration and Palatal or Oculopalatal Tremor. Frontiers in Neurology, 8. https://doi.org/10.3389/fneur.2017.00302

Tournier, J.-D., Calamante, F., & Connelly, A. (2007). Robust determination of the fibre orientation distribution in diffusion MRI: Non-negativity constrained super-resolved spherical deconvolution. NeuroImage, 35(4), 1459–1472. https://doi.org/10.1016/j.neuroimage.2007.02.016

Tournier, J.-D., Smith, R., Raffelt, D., Tabbara, R., Dhollander, T., Pietsch, M., Christiaens, D., Jeurissen, B., Yeh, C.-H., & Connelly, A. (2019a). MRtrix3: A fast, flexible and open software framework for medical image processing and visualisation. NeuroImage, 202, 116137. https://doi.org/10.1016/j.neuroimage.2019.116137

Tournier, J.-D., Smith, R., Raffelt, D., Tabbara, R., Dhollander, T., Pietsch, M., Christiaens, D., Jeurissen, B., Yeh, C.-H., & Connelly, A. (2019b). MRtrix3: A fast, flexible and open software framework for medical image processing and visualisation. NeuroImage, 202, 116137. https://doi.org/10.1016/j.neuroimage.2019.116137

Usunoff, K. G., Itzev, D. E., Lolov, S. R., & Wree, A. (2003). Pedunculopontine tegmental nucleus. Part I: Cytoarchitecture, transmitters, development and connections. Biomedical Reviews, 14(0), 95–120. https://doi.org/10.14748/bmr.v14.111

Verveer, C., Hawkins, R. K., Ruigrok, T. J. H., & De Zeeuw, C. I. (1997). Ultrastructural study of the GABAergic and cerebellar input to the nucleus reticularis tegmenti pontis. Brain Research, 766(1–2), 289–296. https://doi.org/10.1016/S0006-8993(97)00774-9

Voogd, J., & Glickstein, M. (1998). The anatomy of the cerebellum. Trends in Neurosciences, 21(9), 370–375. https://doi.org/10.1016/S0166-2236(98)01318-6

Voogd, J., & Marani, E. (2016). Gross Anatomy of the Cerebellum. In D. L. Gruol, N. Koibuchi, M. Manto, M. Molinari, J. D. Schmahmann, & Y. Shen (Eds.), Essentials of Cerebellum and Cerebellar Disorders (pp. 33–38). Springer International Publishing. https://doi.org/10.1007/978-3-319-24551-5_4

Washburn, S., Oñate, M., Yoshida, J., Vera, J., Bhuvanasundaram, R., Khatami, L., Nadim, F., & Khodakhah, K. (2024). The cerebellum directly modulates the substantia nigra dopaminergic activity. Nature Neuroscience, 27(3), 497–513. https://doi.org/10.1038/s41593-023-01560-9

Waterhouse, B. D., Predale, H. K., Plummer, N. W., Jensen, P., & Chandler, D. J. (2022). Probing the structure and function of locus coeruleus projections to CNS motor centers. Frontiers in Neural Circuits, 16, 895481. https://doi.org/10.3389/fncir.2022.895481

Watts, D. J., & Strogatz, S. H. (1998). Collective dynamics of 'small-world' networks. Nature, 393(6684), 440–442. https://doi.org/10.1038/30918

Wu, X., Sarpong, G. A., Zhang, J., & Sugihara, I. (2023). Divergent topographic projection of cerebral cortical areas to overlapping cerebellar lobules through distinct regions of the pontine nuclei. Heliyon, 9(4), e14352. https://doi.org/10.1016/j.heliyon.2023.e14352

Xu, X., Holmes, T. C., Luo, M.-H., Beier, K. T., Horwitz, G. D., Zhao, F., Zeng, W., Hui, M., Semler, B. L., & Sandri-Goldin, R. M. (2020). Viral Vectors for Neural Circuit Mapping and Recent Advances in Trans-synaptic Anterograde Tracers. Neuron, 107(6), 1029–1047. https://doi.org/10.1016/j.neuron.2020.07.010

Yamamoto, T., Yoshida, K., Yoshikawa, H., Kishimoto, Y., & Oka, H. (1992). The medial dorsal nucleus is one of the thalamic relays of the cerebellocerebral responses to the frontal association cortex in the monkey: Horseradish peroxidase and fluorescent dye double staining study. Brain Research, 579(2), 315–320. https://doi.org/10.1016/0006-8993(92)90067-J

Yeh, C.-H., Jones, D. K., Liang, X., Descoteaux, M., & Connelly, A. (2021). Mapping Structural Connectivity Using Diffusion MRI: Challenges and Opportunities. Journal of Magnetic Resonance Imaging, 53(6), 1666–1682. https://doi.org/10.1002/jmri.27188

Yendiki, A., Aggarwal, M., Axer, M., Howard, A. F. D., van Walsum, A.-M. van C., & Haber, S. N. (2022). Post mortem mapping of connectional anatomy for the validation of diffusion MRI. NeuroImage, 256, 119146. https://doi.org/10.1016/j.neuroimage.2022.119146

Zalesky, A., Fornito, A., Cocchi, L., Gollo, L. L., van den Heuvel, M. P., & Breakspear, M. (2016). Connectome sensitivity or specificity: Which is more important? NeuroImage, 142, 407–420. https://doi.org/10.1016/j.neuroimage.2016.06.035

Zeeuw, C. I. D., Hoogenraad, C. C., Koekkoek, S. K. E., Ruigrok, T. J. H., Galjart, N., & Simpson, J. I. (1998). Microcircuitry and function of the inferior olive. Trends in Neurosciences, 21(9), 391–400. https://doi.org/10.1016/S0166-2236(98)01310-1

Zhang, Y., Brady, M., & Smith, S. (2001). Segmentation of brain MR images through a hidden Markov random field model and the expectation-maximization algorithm. IEEE Transactions on Medical Imaging, 20(1), 45–57. https://doi.org/10.1109/42.906424

Zhao, Y., Wu, J.-T., Feng, J.-B., Cai, X.-Y., Wang, X.-T., Wang, L., Xie, W., Gu, Y., Liu, J., Chen, W., Zhou, L., & Shen, Y. (2025). Dual and plasticity-dependent regulation of cerebello-zona incerta circuits on anxiety-like behaviors. Nature Communications, 16(1), 3339. https://doi.org/10.1038/s41467-025-58727-0

Zhu, J.-N., Yung, W.-H., Kwok-Chong Chow, B., Chan, Y.-S., & Wang, J.-J. (2006). The cerebellar-hypothalamic circuits: Potential pathways underlying cerebellar involvement in somatic-visceral integration. Brain Research Reviews, 52(1), 93–106. https://doi.org/10.1016/j.brainresrev.2006.01.003